Dissertation

submitted to the

Combined Faculty of Natural Sciences and Mathematics

of Heidelberg University, Germany

for the degree of

Doctor of Natural Sciences

Put forward by

Ondrej Jaura, M. Sc.

Born in Bratislava, Slovak Republic

Oral examination on May 27th, 2020

Study of radiation feedback during formation of Population III stars in primordial minihalos

Referees:

Prof. Dr. Ralf Stephan Klessen

Prof. Dr. Björn Malte Schäfer

"All science is either physics or stamp collecting."
Ernest Rutherford

Abstract

Study of radiation feedback during formation of Population III stars in primordial minihalos

In this thesis, we utilize novel radiation transfer technique called SIMPLEX to study complex ionization and dissociation processes in Population III star formation around 400 million years after the Big Bang. The first part describes the SIMPLEX method and its implementation as a radiation transfer code SPRAI in the hydrodynamic code AREPO. We test it on several standard test cases and demonstrate its usability for physically accurate calculations in the astrophysical context. The second part presents our model of first-star formation and discuss our results. We follow the collapse of the primordial gas cloud in the central regions of a minihalo. The collapse of the gas is evolved until the first stars form in the densest regions. Subsequently, we cut out the central four parsecs region of the simulation around the star-forming area, continue the simulation for the next 20 kyrs, and simulate radiation feedback from individual stars. The results show that the effect of the ionizing radiation strongly depends on the starting position of the escaping photons and resolution. Simulations in the previous literature neglect accretion disks within the inner 10 AU around the stars. Our simulations show that the lack of resolution leads to an overestimation of the escaping ionizing photons from the accreting Population III stars. We report the trapping of the ionizing radiation on the scale length of the height of the accretion disk.

"Physics isn’t the most important thing. Love is."
Richard P. Feynman

Zusammenfassung

Untersuchung der Strahlungsrückkopplung der Population III Sternentstehung in primordialen Minihalos

In dieser Arbeit verwenden wir eine neuartige Technik für den Strahlungstransport namens SIMPLEX, um komplexe Ionisations- und Dissoziationsprozesse in einer Population III Sternentstehung etwa 400 Millionen Jahre nach dem Urknall zu untersuchen. Der erste Teil beschreibt die Methode SIMPLEX und ihre Implementierung als Strahlungsübertragungscode SPRAI im hydrodynamischen Code AREPO. Wir testen sie an mehreren Standardtestfällen und demonstrieren ihre Verwendbarkeit für physikalisch genaue Berechnungen im astrophysikalischen Kontext. Im zweiten Teil stellen wir unser Modell der Erststernbildung vor und diskutieren unsere Ergebnisse. Wir folgen einem Kollaps einer Urgaswolke in den zentralen Regionen eines Minihalos. Wir entwickeln den Gaskollaps weiter, bis sich in den dichtesten Regionen die ersten Sterne bilden. Anschließend führen wir die Simulation für die nächsten 20 ka auf einem Bereich von vier Parsec um den Sternentstehungsbereich herum fort und simulieren die Strahlungsrückkopplung einzelner Sterne. Wir stellen fest, dass die Wirkung der ionisierenden Strahlung stark von der Ausgangsposition der austretenden Photonen und der Auflösung abhängt. Simulationen in der vorherigen Literatur vernachlässigen die Akkretionsscheibe innerhalb der inneren 10 AU um die Sterne. Unsere Simulationen zeigen, dass die mangelnde Auflösung zu einer Überschätzung der austretenden ionisierenden Photonen aus den akkretierenden Population III Sternen führt. Wir beobachten das Einfangen der ionisierenden Strahlung auf der Langenskala der Höhe der Akkretionsscheibe.

I dedicate this work to my parents,
who always supported my study of physics,
but never forgot to teach me the most important thing.

Contents

Part I

Radiation in early Universe

1 Introduction

1.1 Motivation

Observations of the light emitted or scattered from other objects are one of the primary means of how we experience and study the world around us. Without such fundamental particles like photons, our Universe would be a dark and hostile environment. The first stars emerged hundreds of million years after the Big Bang (BB) and separated the light from the darkness. These events gradually changed the structure of the matter and eventually resulted in the Universe's complexity and various life forms as we know them today. One can investigate very early stage of star formation only indirectly. The gas composition of the interstellar medium (ISM) is nowadays enriched by heavier elements and there are only a few known examples of the extremely metal-poor objects (Beers and Christlieb, 2005; Caffau et al., 2011; Simcoe et al., 2012; Hsyu et al., 2017). The advance of technology and numerical methods allows us to study these highly non-linear processes using computational models.

We divide the motivation of this work into the methodological and scientific part: Firstly, we want to learn more about the role of radiation feedback in the early universe and the formation of the first stars. For this purpose, we set up a set of simulations that follow the initial phase of this process in great detail and with high resolution. Secondly, as a means of our research, we chose to extend and explore the possibilities of an alternative numerical technique that has the potential to solve the complicated radiation transfer problem in a more efficient way. In the text below, we address both of these parts.

The appearance of the first stars ended the so-called "Dark Ages" of our Universe (Loeb, 2010). They played a key role in cosmic metal enrichment and reionization, thereby shaping the galaxies and their internal properties as we see them today. In order to study the impact of the first generations of stars, also known as Population III stars (Pop-III), on subsequent cosmic evolution, we need to know when and where they form, and how many to expect. We also need to understand better the physical processes that control their initial mass function (IMF) and multiplicity. These are the primary parameters that determine the spectral energy distribution of the stellar radiation field, the amount and composition of heavy elements produced, and the energy and momentum carried away by winds and eventually by supernova explosions.

Pop-III stars form by gravitational collapse of truly metal-free primordial gas that is accummulated in the potential wells of dark matter halos. First star formation is thought to set in at redshifts $z \gtrsim 30$ and reach a peak rate at $z \sim 20 - 15$. Although the overall cosmic star formation rate continues to increase (Madau et al., 2014), the rate at which metal-free stars form declines at later times as gas that is not enriched by supernova ejecta becomes increasingly rare (Bromm and Larson, 2004; Yoshida et al., 2012; Bromm, 2013;

Glover, 2013; Klessen, 2018). Early studies of Pop-III star formation predicted that only one extremely massive star should form in each dark matter halo with about 100 solar masses or more (Omukai, 2001; Abel et al., 2002; Bromm et al., 2002; O'Shea and Norman, 2007). With the ever-increasing capabilities of modern supercomputers, however, this situation has changed, and more recent investigations and numerical simulations lead to the conclusion that fragmentation is a widespread phenomenon in first star formation (Clark et al., 2011a; Greif et al., 2012). We now believe that most Pop-III stars form as members of multiple stellar systems with a wide range of separations and mass ratios (Turk et al., 2009; Clark et al., 2011b; Greif et al., 2011b; Smith et al., 2011; Stacy and Bromm, 2013). This raises the question of whether these fragments survive or merge together. As yet, there is no convincing answer to this question because all existing analytic or numerical models either deal with restricted geometry, only include a subset of the relevant physical processes, or only cover the initial phase of the overall evolution. Studies that do include radiative feedback (Hirano et al., 2014, 2015; Hosokawa et al., 2016), magnetic fields (Machida et al., 2006, 2008; Schleicher et al., 2009; Sur et al., 2010, 2012; Turk et al., 2012; Schober et al., 2012a,b; Bovino et al., 2013b), dark matter annihilation (Smith et al., 2012; Stacy et al., 2014), as well as the primordial streaming velocities (Tseliakhovich and Hirata, 2010; Greif et al., 2011b; Maio et al., 2011; Stacy et al., 2011; Schauer et al., 2019) add to this complexity.

In this thesis, we build on the previous studies and follow with high ($\sim$1 AU) resolution collapse of a gas cloud in a primordial minihalo and subsequent fragmentation of the accretion disks. We study the effects of the radiation feedback from each of the newly formed Pop-III stars and analyze their environment. We also derive the IMF for each of our radiation model.

Before we pursue our scientific goal, we need to address and improve the numerical techniques used in our simulations. Multiple methods solve hydrodynamics of the matter, either using Lagrangian or Eulerian description of the fluids (Fryxell et al., 2000; Teyssier, 2002; Springel, 2005, 2010; Hopkins, 2015). Chemistry solvers follow abundances of the elements in the simulated gas, via primordial (Glover, 2015a,b) or the present-day (Glover and Clark, 2012) networks. The main difference between the two networks is in the presence of metals that are responsible for various processes in the ISM and nucleosynthesis within the stars. In the following chapter, we will focus mainly on the primordial case, which assumes metal-poor environments. Other implementations extend the hydrodynamics with magnetic fields (Pakmor et al., 2011; Pakmor and Springel, 2013). Radiation transfer codes solve interactions of light with matter (Dullemond et al., 2012; Reissl et al., 2016, 2018; Rosdahl et al., 2013; Baczynski et al., 2015; Kannan et al., 2019).

We choose to do our simulations using the AREPO code (AREPO) (Springel, 2010). It performs excellently in simulations with multi-scale systems, conserve the angular momentum, and does not produce square-shaped artifacts found in codes that use Cartesian girds. We present a new implementation of the SPRAI module (SPRAI) (Jaura et al., 2018). It is based on the SIMPLEX radiation transfer (SIMPLEX) (Ritzerveld and Icke, 2006; Kruip et al., 2010; Paardekooper et al., 2010) method that is for the first time used in combination with the parallel hydrodynamical solver. The advantage of this method is that it can directly use the Voronoi mesh constructed by the hydrodynamical solver of the AREPO. Additionally, its computational costs do not scale with the number of sources, as in the case of the standard

ray-tracing. This property is especially useful when studying accretion disk fragmentation and multiple stellar systems.

Radiation interaction with the ISM is often non-local and influences many physical properties of the gas (e.g., ionization state, temperature, and dynamics). Therefore, we dedicate a substantial part of this thesis to the explanation of this method and discussion of its physical accuracy in various test problems.

1.2 Outline

This thesis is divided into eight chapters that together form four main parts: In Chapter 1, we provide the reader with a concise overview of the whole work. The next two Chapters, 2 and 3, give a broader theoretical introduction to the physical processes in the early universe and computational methods. Chapters 4, 5, and 6 are three self-contained works that correspond to our three recent or prepared publications. The last two Chapters, 7 and 8, conclude the thesis and state acknowledgments. At the very end, we also include lists of abbreviations and bibliography. The list below provides brief descriptions for each chapter.

Chapter 2 The first stars appear in the very early stages of the Universe, and their formation and composition differ from the stars in the present Universe. In this chapter, we summarize the necessary theoretical background and physical context of this period.

Chapter 3 In this chapter, we discuss numerical methods used to calculate hydrodynamics and radiation transfer. We give a brief overview of the frequently used methods and codes and compare those that we used in our simulations.

Chapter 4 The text in this chapter is an excerpt from the already published method paper of the SPRAI code. We introduce here the basics of the method, provide several test cases, and show its strengths and shortcomings.

Chapter 5 This part builds on the previous chapter. It is an excerpt from the second paper from the series on the SPRAI method. We discuss difficulties of simulations within high-density regions, discuss new features like multi-frequency, dust heating, and radiation pressure.

Chapter 6 We apply the method described in the previous two chapters in this chapter on the problem case from the early universe. This text is also an excerpt from the prepared paper. We set up a set of simulations where we trace the collapse of the gas cloud in the primordial mini-halo. We observe the first 20 kyr of star formation in the cloud and the onset of the radiation feedback. We give a detail description of our setup and discuss our results.

Chapter 7 In the end, we provide a summary of this thesis, state our conclusions, and give an outlook for our next scientific steps.

Chapter 8 The work in this thesis would not be possible without support from various people, grants, and institutions. Here we acknowledge their contributions and support.

2 Theory

In this chapter, we will give a broader introduction to the astronomical context used in our study. The first section describes the cosmological setting of our simulations. In the second section, we summarize the collapse of the primordial halos. In the third section, we will focus on the cooling and heating processes that take place in such minihalos.

2.1 Cosmological context

The physical cosmology studies the evolution of the Universe from its beginning to the present time. The current standard BB theory assumes the Lambda Cold Dark Matter (ΛCDM) model of the Universe. However, mock observation of the strong gravitational lensing (Li et al., 2016) also suggests that models with Warm Dark Matter (WDM) particles are possible. In this section, we will introduce the related theory and basic terms. Simulations and results described in the following chapters assume this cosmological context. Nevertheless, the effect of the expansion of the Universe on time intervals studied in our simulations is negligible, and we do not calculate it explicitly. In the Section 2.1.1 we briefly summarize the basic cosmological parameters that are implicitly assumed in our simulations.

Figure 2.1 shows a schematic timeline of the Universe for this model. In the Figure, we show various milestones in the history of the Universe. We will address the most important of them in the following subsections.

2.1.1 Cosmological parameters

The basic cosmological theory follows Einstein's general relativity theory and field equation

$$G_{\mu\nu} + \Lambda g_{\mu\nu} = \frac{8\pi G}{c^4} T_{\mu\nu}, \tag{2.1}$$

where Λ is the cosmological constant, $G_{\mu\nu} = R_{\mu\nu} - \frac{1}{2} g_{\mu\nu} R$ is the Einstein tensor, $R_{\mu\nu}, R$ are respectively Ricci tensor and scalar, $g_{\mu\nu}$ is a metric tensor, $T_{\mu\nu}$ is the stress-energy tensor, c is the speed of sound and G is the gravitational constant. Indices μ and ν denote components of the tensors.

The cosmological principle says that the Universe is on large (>100 Mpc) scales isotropic (same in all directions) and homogeneous (same in all points of the space). Using the Friedmann-Lemaítre-Robertson-Walker metric

$$ds^2 = c^2 dt^2 - a^2(t) \left[\frac{dr^2}{1 - kr^2} + r^2 (d\theta^2 + sin^2 \theta d\phi^2) \right], \tag{2.2}$$

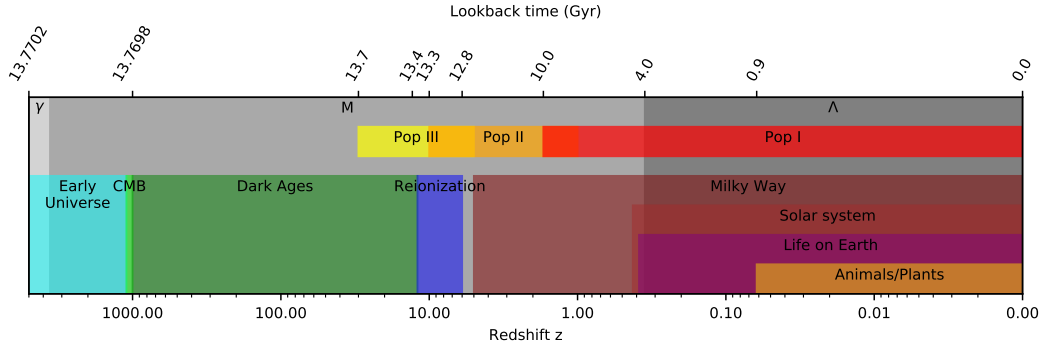

Figure 2.1: This figure shows a schematic timeline of the Universe in the ΛCDM model. The bottom x-axis shows the cosmological redshift z, and on the top, we add corresponding physical lookback times. Different shades of the grey show three main epochs of the Universe expansion: γ-radiation, M-matter, and Λ-dark energy (DE) dominated. Colorful rectangles mark the selection of several time ranges. Ranges of different star populations partially overlap.

where c is the speed of light, $a(t)$ is the time-dependent scale factor, k is the curvature parameter of the (open k=1, flat k=0, or closed k=-1) space and (r, θ, ϕ) are comoving polar coordinates, one can derive for the 00 component of the Einstein's field equation the following Friedmann equation

$$H^2 = \left(\frac{\dot{a}}{a}\right)^2 = \frac{8\pi G}{3}\rho - \frac{kc^2}{a^2} \tag{2.3}$$

where $H \equiv \frac{\dot{a}}{a}$ is a Hubble parameter and $\rho(t)$ is a time-dependent density.

A common choice of the scale factor at present time is $a(0) = 1$. The scale factor is also important for observational astronomy because one can use it indirectly as a measure of time in the early universe. From the redshift z of the light emitted from a distant object, one can calculate the scale factor at the time the object originally emitted that light using $a = \frac{1}{1+z}$.

The Equation 2.3 can be further rewritten in terms of density parameter components

$$\frac{H^2}{H_0^2} = \Omega_{0,R}a^{-4} + \Omega_{0,M}a^{-3} + \Omega_{0,k}a^{-2} + \Omega_{0,\Lambda}, \tag{2.4}$$

where $\Omega \equiv \frac{\rho}{\rho_c}$ is defined as the ratio of the observed density ρ to the critical density $\rho_c = \frac{3H^2}{8\pi G}$ of the Friedmann universe. Density components at present in the above equation correspond to the relativistic particles (e.g. photons or neutrinos) $\Omega_{0,R}$, matter (dark and baryonic) $\Omega_{0,M}$, spatial curvature density $\Omega_{0,k} = 1 - \Omega_0$, and density of the vacuum (cosmological constant) $\Omega_{0,\Lambda}$. The sum of the above components is

$$1 = \Omega_{0,R} + \Omega_{0,M} + \Omega_{0,k} + \Omega_{0,\Lambda}. \tag{2.5}$$

Most recent values of the cosmological parameters from the Planck Collaboration (2019) are summarized in the Table 2.1. The values show that the Universe is almost perfectly flat (k=0 and $\Omega_0 \approx 1$). The 68.9% of the total energy in Universe is distributed in dark energy (DE), 26.2% in dark matter (DM) and only 4.9% in visible baryonic matter.

Parameter		Value	Units
Total matter density	Ω_m	0.3111 ± 0.0056	
Dark matter density	$\Omega_c h^2$	0.120 ± 0.001	
Baryon matter density	$\Omega_b h^2$	0.0224 ± 0.0001	
Dark energy density	Ω_Λ	0.6889 ± 0.0056	
Spatial curvature	Ω_K	0.0007 ± 0.0019	
Hubble constant	H_0	67.66 ± 0.42	km s^{-1} Mpc^{-1}
Age of the Universe		13.787 ± 0.020	Gyr

Table 2.1: Best fit of cosmological parameters measured by the Planck Collaboration (Planck Collaboration, 2019). The small h (Hubble parameter) is defined as $h = H_0/(100 \text{ km s}^{-1} \text{ Mpc}^{-1})$.

2.1.2 Expansion of the universe

Equation 2.4 from the previous section, together with the measurements of the Planck telescope (Planck Collaboration, 2019), give one the most comprehensive model of the Universe evolution. One can estimate from the solutions of the scale factor the time when all distances in the space were near to zero $a(t_{\text{age}}) = 0$. The results of the Planck data estimate this time (age of the Universe, or time of the BB) as $t_{\text{Age}} = 13.787$ Gyr.

After the BB and cosmic inflation, all matter in the early universe was in the form of a very dense primordial quark-gluon plasma. Detailed physics of this early stage requires further, comprehensive knowledge of particle physics and is beyond the scope of this thesis. The important characteristic of this period is that the light was coupled with the matter and could not propagate freely in the space. Approximately 47 kyr after the BB, the energy density of matter exceeded both the energy density of radiation and the vacuum energy density. This event marked the transition between the Radiation-dominated (γ) and the Matter-dominated era (M), also shown in Figure 2.1. Solution of the expansion factor in the Friedmann equation for the former is $a(t) \propto t^{1/2}$ and for the latter $a(t) \propto t^{2/3}$.

As the Universe expanded, also the distances between all particles in the primordial plasma were growing. Eventually, 378 kyr after the BB light could decouple from the matter and started to propagate freely through space. Today, we can observe these free photons in the form of the Cosmic Microwave Background (CMB). One refers to this epoch as "recombination" because charged electrons and protons first became bound and formed the electrically neutral Hydrogen. After this event, the only light in the Universe was that of the CMB. This period is also called "Dark Ages". Space was at this time filled only by DM and the simplest baryonic matter. In terms of the mass fraction, there was $X_{\text{H}} \approx 76\%$ of Hydrogen and $X_{\text{He}} \approx 24\%$ of Helium.

Initial density fluctuations of the primordial plasma caused that some regions in the space started to collapse under their gravity. First, the dominant component of the mass, DM, formed so-called Cosmic Web. This large scale structure consists of many filaments and knots (halos) that form in the over-density regions. Less abundant baryonic matter followed the gravitational potential of the DM and accumulated in the forming halos. This gas accretion continued until densities in the central parts were high enough and led to the

ignition of the first thermonuclear fission in stars. Different stellar populations are discussed in the next 2.1.3. Star-forming regions in these halos later formed star clusters and galaxies.

Newly formed stars produced radiation, which in turn started to ionize surrounding neutral ISM and intergalactic medium (IGM). This process between redshifts $z = 12 - 6$, called Epoch of Reionization (EoR), brought our Universe into the fully ionized state. The same as we observe up to the present day.

The last milestone in the history of the Universe is the transition between matter-dominated and DE-dominated era. This transition happened when the Universe was about 9.8 Gyr old. Increasing energy of the vacuum Λ (DE) started to accelerate the expansion of the Universe. The solution of the Friedmann equation at this epoch $a(t) \propto exp(Ht) = exp(t\sqrt{\Lambda/3})$ also reflects this exponential growth.

2.1.3 Stellar populations

The standard division of star population in the historical context of the Universe is according to their abundance of the heavy metals (Z, metal enrichment, or metallicity). In our terminology, we call metals all elements with atomic masses higher than Hydrogen and Helium. Fusion processes within the stars and accretion of the enriched ISM increases the metallicity. Metal lines are visible in the spectral emission. In this section, we give a brief overview of each group ordered from the present time to the past.

Population I stars (Pop-I) (or present-day stars) are stars found in the spiral arms and star-forming regions of the Milky Way, or similar galaxies. They form from the metal-rich ISM and are highly luminous and most frequent at z=0. We classify these stars according to their color and luminosity, and the famous Hertzsprung–Russell diagram summarizes their life cycles. During their lifetime, stars produce energy by fusing lighter elements into heavier elements through a process known as nucleosynthesis (e.g., the proton-proton (PP) chain, CNO cycle, triple-α process of helium burning and the carbon and oxygen burning. Since explanation of these processes is beyond the scope of this thesis, we refer our reader to the standard literature.) The metallicity of present-day stars is comparable to the Sun $Z \approx Z_{\odot} = 0.0134$ or as high as $Z = 0.03$.

Population II stars (Pop-II) have extremely low metallicities $Z \approx 10^{-4}\ Z_{\odot}$. They formed as a second generation of stars from gas enriched by exploded Pop-III supernovae. Within our Galaxy, they are located mainly in the outer parts of the galactic halo and in globular clusters.

Population III stars (Pop-III) (or first stars) are the oldest stars that are thought to have formed around 400-1000 million years after the BB, between redshifts $z = 30 - 5$. They differ from present-day stars because they formed from the most pristine primordial gas, and their metallicities are zero $Z = 0$. Their composition is the same as the composition of the primordial gas: Hydrogen and Helium. Higher elements and metals were introduced into the IGM medium after the first supernovae exploded and enriched their environment. Because

of the zero metallicity of the accreting gas, the primary source of energy was Deuterium and Hydrogen burning. We will discuss more details about the Pop-III formation in the following section.

2.2 Formation of Population III stars

In this Section, we will discuss in more detail the formation of Pop-III stars, their interaction with the environment through radiation, and their importance for the later stages of the universe and structure formation.

2.2.1 Initial cloud collapse

Molecular clouds with an efficient cooling give birth to the new stars. The self-gravity in this region needs to be stronger than the internal pressure of the gas. In the present-day star formation, the essential coolants are metals. However, in the primordial scenario, metals were not yet present in the interstellar medium.

Heating and cooling processes lower the thermal energy of the gas cloud until it collapses under its gravity. First, the infalling gas heats up to the virial temperature[1] of its minihalo. The most efficient coolant at temperatures $T \simeq 10^4$ K is collisional excitation cooling, also called Lyman-α cooling. Below this temperature is cooling time shorter. Reaction of the atomic hydrogen with the free-electron ($H+e^- \rightarrow H^-+\gamma$) and subsequent detachment of these atoms with neutral hydrogen atoms ($H^-+H \rightarrow H_2+e^-$) results in formation of molecular Hydrogen. In temperature range between 200 K $\leq$ T $\leq$ 5000 K, the rotational and vibrational states of H_2 in the electronic ground state are excited by collisions with other particles. The decay of these states allows the gas to cool down to $T \simeq 200$ K. In Section 6.3, we use this stage of gas collapse in our initial conditions and follow the subsequent gas evolution in 3D simulation.

Nearly isothermal collapse of the cloud continues to densities $n_H \simeq 10^8$ cm^{-3} until three-body reactions (Palla et al., 1983) start to produce even more molecular Hydrogen ($H+H+H \rightarrow H_2+H$) and increase the cooling rate. At gas number densities $n_H \geq 10^{10}$ cm^{-3} gas becomes optically thick to H_2 line emission. Further on, when gas reaches densities $n_H \geq 10^{14}$ cm^{-3}, collision-induced emission (CIE) becomes important (Omukai and Nishi, 1998; Ripamonti and Abel, 2004). This is characterized by formation of 'super-molecule' from two hydrogen molecules that approach each other. Such super-molecules have higher cooling rates than H_2 due to their dipole moments. At densities $n_H \geq 10^{15}$ cm^{-3} a collisional dissociation of H_2 becomes important (Turk et al., 2012; Hartwig et al., 2014; Greif, 2014).

An additional cooling agent is hydrogen deuteride (HD) because, unlike H_2, it possesses a permanent electric dipole moment that has higher radiative transition probabilities. It forms at densities $n_H \sim 10^6$ cm^{-3} through reactions of the molecular hydrogen with deuterium ions. It can cool the gas to temperatures below 200 K and possibly down to the temperature of the CMB.

[1] For typical halos with virial masses $M_{vir} \simeq 10^6 M_\odot$ at redshift $z = 19$ the virial temperature is $T_{vir} \simeq 2 \times 10^3 K$

Jeans stability criterion (Jeans, 1902) of the gas cloud describes a balance between self-gravity and thermal pressure in a gas. If the former is stronger than the later, the cloud collapses. For a molecular cloud with a mass $M_{\rm cloud}$ and radius $R_{\rm cloud}$ one can derive it from the Virial theorem

$$2K + U = 0, \tag{2.6}$$

where $K = \frac{3}{2}NkT$ is the kinetic and $U \approx -\frac{3}{5}\frac{GM_{\rm cloud}^2}{R_{\rm cloud}}$ potential energy of the gas in a cloud. From the above assumptions, one can derive a criterion

$$M_{\rm cloud} > M_J \tag{2.7}$$

for the collapse. The corresponding Jeans mass is

$$M_J \approx \left(\frac{5kT}{G\mu m_H}\right)^{3/2}\left(\frac{3}{4\pi\rho_0}\right)^{1/2}, \tag{2.8}$$

where the ρ_0 is the gas density of the cloud. Similarly, one can derive a Jeans length as

$$R_J \approx \left(\frac{15kT}{4\pi G\mu m_H \rho_0}\right)^{1/2} \tag{2.9}$$

Toomre's stability criterion (Toomre, 1964) is a relationship between parameters of differentially rotating gaseous disks, such as accretion disks around forming stars. In addition to the Jeans criterion (for a spherical symmetry), the shear force of a rotating disk provides an additional stabilizing force against the collapse. Toomre parameter in the gas is defined as

$$Q_{\rm gas} \equiv \frac{c_s \kappa}{\pi G \Sigma}, \tag{2.10}$$

where c_s is the speed of sound, κ is the epicyclic frequency, G is the gravitational constant, and Σ is the surface density of the disk. A gaseous disk is stable against collapse under the following condition: $Q_{\rm gas} > 1$.

Subtypes of Population III stars can be categorized according to the influence of external radiation feedback that is present during their formation and life (Bromm et al., 2009). The very first population, Pop-III.1, formed without the influence of an external radiation field. It can be classified (Hirano et al., 2014) into two subclasses depending on whether HD molecular cooling affects the thermal evolution of the star-forming cloud or not (Pop-III.$1_{\rm HD}$ or Pop-III.$1_{\rm H_2}$, respectively).

The second type of stars, Pop-III.2, is formed in environments with an external radiation field. This can be further divided into cases (Hirano et al., 2015) where the external radiation is photodissociation-dominated (Pop-III.$2_{\rm D}$) or photoionization-dominated (Pop-III.$1_{\rm I}$). The former dissociates the H_2 and HD molecules and makes the temperature of the collapsing cloud and final stellar mass higher. In the latter case, the gas environment is pre-ionized and leads to creation of more H_2 and HD molecules. In turn, such clouds evolve at low temperatures due to enhanced cooling.

2.2.2 Radiation

In the previous sections, we focused on the formation process of the first stars. In this section, we will discuss the fundamental principles of how stars interact with their environment. In the case of Pop-III stars, this interaction is more straightforward than in the case of present-day stars because it includes only reactions with molecular and atomic Hydrogen or Helium. In the cosmological context, it is often necessary to simulate radiation on large scales and from a large number of sources. Therefore, having an efficient radiation transfer code is essential for research in this field.

Lyman-Werner (LW) radiation is an ultra-violet radiation band with energy between 11.2 – 13.6 eV. This range corresponds to the band of absorption lines of molecular Hydrogen. The absorbed radiation put H_2 into higher electronic states that rapidly decay. Roughly 15% of the states decay into the vibrational continuum of the molecule and result in its dissociation. Therefore, photodissociation of H_2 needs much more energy than the H_2 binding energy. Strong LW radiation, however, can act against the formation of H_2, decrease the cooling, and prevents the star formation. This feedback is especially effective in molecular clouds around the accreting stars.

Ionizing radiation strips electrons of the atoms or molecules and puts them into a higher energetic state. Volumes of Hydrogen gas irradiated by photons more energetic than 13.6 eV are commonly known as HII regions. Ionization front (I-front) is a transition between the neutral ISM and the ionized gas around a star. Helium, with its two ionization states, HeII and HeIII, can also form ionized regions in a similar way. In this case, the ionization requires photons with energies above 24.6 eV and 54.4 eV, respectively. Radii of their I-front can differ from that of the ionized Hydrogen. Formation of the HeII is comparable to the HII regions, but HeIII regions are present only around sources with hard spectra, such as active galactic nuclei (AGN).

We distinguish two phases of the I-front. The first, rarified-type (R-type), phase propagates fast and ends when the number of ionizations in the gas reaches equilibrium with the number of recombinations. The analytical solution of this physical problem is known as Strömgren radius. We will discuss this in detail in the following Chapters 4 and 5.

Second, density-type (D-type), comes in the uniform medium at later times as a thermodynamic response of the gas. Each ionizing photon carries some excess energy, which goes during the ionization process into gas heating. Ionized gas can reach temperatures up to several 10^4 K and expand. A shock wave at the surface of the expanding ionized bubble propagates through the medium and forms a D-type I-front. The expansion stops when the pressure on both sides of the I-front becomes equal.

21 cm line in the radio spectrum corresponds to the radiation emitted during the change of the spin between two hyperfine levels of the hydrogen 1s ground state. The name comes from the actual wavelength of such radiation (1420 MHz = 21 cm). Due to its long lifetime Δt,

the line has a small[2] natural width ΔE, and most of its broadening is due to Doppler shifts. This fact is used in radio astronomy to measure relative velocities of gas in galaxies. In cosmology, one uses the 21 cm line to study the "Dark Ages", to estimate the matter power spectrum in the period after recombination and to understand the epoch of reionization.

Lyman-α is an ultraviolet spectral emission line of hydrogen. It corresponds to the transition of electrons from the n=2 (1216 Å) to the n=1 orbital. Observation of Lyman-α radiation is essential for cosmology because it contains information about the end of the reionization. Light from distant galaxies or quasars travels through multiple gas clouds with different redshifts. Its interaction with neutral hydrogen in such clouds results in multiple absorption lines in its spectrum.

Blackbody radiation is often a good approximation of stellar spectra, particularly for Pop-III stars, which have a lower opacity than Pop-I stars. This concept is useful when simulating photon emission from the star because it depends only on the surface temperature. A simple formula of such spectrum, derived by Planck, has a form

$$B_\lambda(T) = \frac{2hc^2}{\lambda^5} \frac{1}{e^{hc/\lambda kT}}, \tag{2.11}$$

where T is surface temperature, h is the Planck constant, λ is a wavelength, k is the Boltzmann constant, and c is the speed of light.

The stellar spectrum, in reality, does not have a smooth profile. It has different features, absorption, or emission lines depending on the different frequencies from chemical processes and elements contained in the star. One can get more precise stellar spectra for low or zero metallicity from Starburst99 (Leitherer et al., 1999) or BPASS (Eldridge and Stanway, 2016) that also involves binary evolution.

2.2.3 Growth and final fate

During their lives, stars accrete material from the surrounding ISM, and their masses increase. The mass and accretion rate has an impact on their radii and the amount of radiation they produce (Schaerer, 2002; Haemmerlé et al., 2018). The lifetimes of the most massive Pop-III stars (50-1000 $M_\odot$) range around 1-3 Myr. Stars with lower masses ($\lesssim$50 $M_\odot$) live several tens of Myr. The smallest stars, with masses below 0.8 $M_\odot$, could survive long enough (Kippenhahn et al., 2012) that we could observe their light in the present.

Initial mass function of the first stars is still not fully understood because many factors influence gas collapse, its fragmentation into stars, and their possible merging. The first simulations of Pop-III (Omukai, 2001; Omukai and Palla, 2003; Bromm et al., 2002; Abel et al., 2002) proposed that the masses range from 10 to 1000 $M_\odot$. However, recent models (Susa et al., 2014; Stacy et al., 2016; Hirano and Bromm, 2017) that include various feedbacks predict ranges from below 1 to only several 100 $M_\odot$.

[2]This follows from the quantum mechanical uncertainty principle $\Delta E \Delta t \geq \frac{\hbar}{2}$.

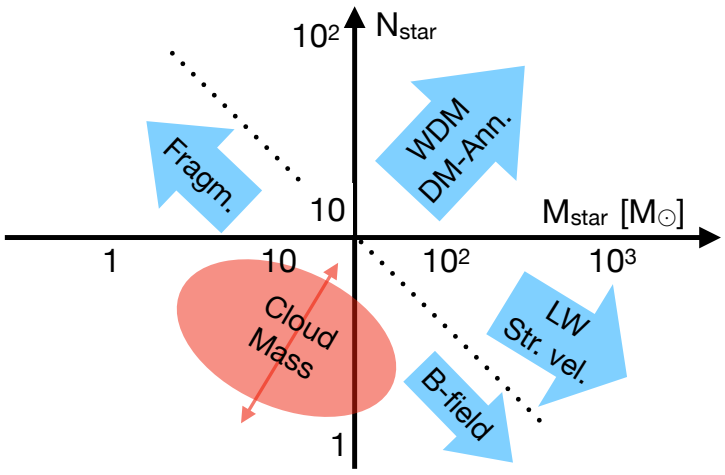

Figure 2.2: This Figure summarizes various feedbacks that influence the mass spectrum of the Pop-III stars. For more description, see the main text in Section 2.2.3. The dotted line approximately marks the ranges for the initial cloud masses below (left) or above (right) 1000 $M_\odot$.

In Figure 2.2 we summarize how different feedbacks influence mass spectrum of Pop-III stars. Initial mass of a collapsing gas cloud is the first factor that defines final mass spectrum. Gas fragmentation leads to higher number of stars and smaller masses. However, merging of fragments can decrease their number (Susa, 2019). On the other hand, magnetic fields delay the onset of fragmentation (Schober et al., 2012a,b; Bovino et al., 2013a) and lead to higher masses of the final stars. Similarily, LW radiation (Stacy et al., 2016; Hosokawa et al., 2016) dissociates H_2 and streaming velocities[3] (Stacy et al., 2011; Schauer et al., 2019) reduce baryon overdensity in ninihalos. This, in both cases, delays the onset of cooling and reflects on small number of stars and higher masses. Finally, the annihilation of DM or alternative cosmology WDM may both increase the number of stars and their masses. However, we will not discuss these in more detail in this work.

Final fate of the Pop-III stars can be divided into several scenarios (Heger and Woosley, 2002, 2010; Heger et al., 2003): Low-mass stars with masses below 10 $M_\odot$ end their life as CO or NeO white dwarfs. Stars with intermediate masses ignite carbon and oxygen burning and end up as neutron stars (<25 $M_\odot$) and fallback (<40 $M_\odot$) or direct (40-100 $M_\odot$) black holes. The resulting supernova explosion expels the hydrogen-rich envelope and parts of the helium core of stars below 40 $M_\odot$. Stars in the mass range between 140-260 $M_\odot$ are thought to end as strong pair-instability supernovae, which can lead to the total disruption of the star. Self gravitation of the stars above this mass limit results in a direct collapse to a black hole.

First supernovae in the primordial universe gradually changed the composition of the ISM. Nuclear processes during the first stars' lifetimes and the resulting supernova explosions

[3]Streaming velocities are relative velocities between the DM and baryonic matter.

produced higher elements and enriched their surrounding environment. Later generations of stars formed from such metal-enriched gas. This transition from Pop-III to Pop-II needs to be studied on large spatial and time scales and still require more research (Johnson et al., 2013; Jaacks et al., 2018). Our simulations in Chapter 6 do not evolve stars long enough to consider their explosions as supernovae and subsequent mixing of metals in the ISM. Nevertheless, we already use SIMPLEX on projects that address also these issues (see also Section 7.2).

3 Simulation methods

In this chapter, we give an introduction to the computational simulation methods used to study nonlinear processes in the Universe.

3.1 Hydrodynamics

Behavior of the DM and baryonic matter in the universe can be on large scales approximated by hydrodynamics. The main set of equations that describe the movement of fluids is the Euler equations. In their compact form, they describe conservation laws of mass, momentum, and energy

$$\frac{\partial}{\partial t}\begin{pmatrix}\rho\\ \rho\boldsymbol{v}\\ \rho e\end{pmatrix}+\nabla\begin{pmatrix}\rho\boldsymbol{v}\\ \rho\boldsymbol{v}\boldsymbol{v}^T+P\\ (\rho e+P)\boldsymbol{v}\end{pmatrix}=0, \tag{3.1}$$

where $\boldsymbol{v}$ is the velocity field, $e = u + \boldsymbol{v}^2/2$ is the total energy per unit mass with a thermal energy per unit mass u. From the equation of state, one can derive the gas pressure as

$$P = (\gamma - 1)\rho u, \tag{3.2}$$

where γ is the polytropic index of the gas.

There are two approaches to solve the equations describing hydrodynamics numerically. Lagrangian codes trace the particles representing gas particles that move in the field. An example of such code is the GADGET-2 code (GADGET) (Springel, 2005). Eulerian codes calculate fluid fluxes as they pass through the cell faces of a grid. A typical code using a fixed Eulerian grid is the RAMSES code (RAMSES) (Teyssier, 2002). A compromise between the above two concepts is a moving mesh hydrodynamics of the AREPO code (AREPO) (Springel, 2010). We use this code for our simulations, because it performs excellently in simulations with multi-scale systems, conserve the angular momentum, and does not produce square-shaped artifacts found in codes that use Cartesian girds.

AREPO uses grid cells with irregular shapes. Each cell is defined by a point, that carries all the information about the gas that it contains. From these points, one can construct unique Voronoi tessellation or so-called Voronoi mesh. However, we will not discuss details of the construction algorithms here. One of the properties of the Voronoi cells is that their faces are lying directly between the points of neighboring cells. During the simulation, AREPO calculates various properties, fluxes, and gradients of the gas on these interfaces.

The coordinates and subsequent shapes of the Voronoi mesh are not static but adjust to the gas properties. Cells drift with the flowing gas and use a regularization algorithm that coincides their locations with the center-of-mass of the cells. One can also ensure that

the cells preserve some fixed masses, or they can be additionally refined and de-refined according to the density or other criteria. In this way, the cells can adapt to the shape of the simulated gas structure.

AREPO calculates gravitation using tree-based approach for collisionless dynamics in a similar way as GADGET. Near field gravitation interactions are calculated directly. For a distant field, it uses hierarchical multipole expansion with an opening angle. Because of the large dynamic ranges in densities, AREPO uses hierarchical time steps. This approach ensures that the computational power is used mainly for those cell regions that need frequent updates. We discuss this approach and its implications for the SPRAI more in Section 4.2.1.

3.2 Radiation transfer

Radiation in the universe is present near the radiation sources that include stars, AGN, and other objects that generate electromagnetic radiation. However, physically accurate and computationally efficient modeling of radiative transfer remains still a challenge for conventional supercomputers. Due to the almost instantaneous and non-local nature of the photon reactions, such calculations require considerably more computing time and memory than simulations without radiation. In this section, we will introduce the basic equation for the radiation transfer and describe several radiation transfer methods that solve them numerically.

One can derive the equation of radiation transfer from a simple example. Consider a ray of light with intensity I_ν passing through a medium in a small cylindrical element of cross-section $d\sigma$ and height ds. The difference in the radiant energy of the ray in the frequency interval $d\nu$, time interval dt and solid angle element $d\omega$ is given by

$$\frac{1}{c}\frac{dI_\nu}{dt} + \frac{dI_\nu}{ds} = j_\nu - (\kappa_{\nu,s} + k_{\nu,a})I_\nu + \frac{1}{4\pi}k_{\nu,s}\int_\Omega I_\nu d\Omega, \tag{3.3}$$

where j_ν is the emission coefficient, $k_{\nu,s}$ is the scattering opacity, $k_{\nu,a}$ is the absorption opacity and Ω is the solid angle. The last term on the right side represents radiation scattered from other directions in the same direction as the ray. Since the radiation usually dominates regions around the stars, one can use an on-spot-approximation and neglect the far-field effects of scattering. In our study, we use a time-independent version of this equation without scattering

$$\frac{dI_\nu}{ds} = j_\nu - \kappa_\nu I_\nu. \tag{3.4}$$

The equation above is a first-order linear differential equation with a constant coefficient with the following solution on the path length s

$$I_\nu(s) = I_\nu(s_0)e^{-\tau_\nu(s_0,s)} + \int_{s_0}^{s} j_\nu(s')e^{-\tau_\nu(s',s)}ds', \tag{3.5}$$

where the optical depth is defined as

$$\tau_\nu(s_1, s_2) = \int_{s_2}^{s_1} \kappa_\nu ds. \tag{3.6}$$

The first term on the right hand side (RHS) of the Equation 3.5 is an intensity of the ray starting from $s = 0$ that is reduced exponentially by the absorption. The second term on the RHS is an integral of all photons emitted by sources along the path s. If the medium does not contain many sources and is not diffusive, this second part is usually equal to zero.

We can divide the solution of Equation 3.4 into partial solutions and follow individual rays on their discrete paths. At the proximity of the source, we need a relatively small number of rays to cover the whole solid angle and achieve converging results. The solid angles of the rays have to be smaller than the volume elements around the source. Far-field solutions of radiation transfer needs additional ray splitting techniques. The surface of the solid angle increases quadratically with the radius, and one needs more rays to cover the full solid angle.

Currently, there are several approaches used to solve radiation transfer in hydrodynamical simulations, each of which has its advantages and limitations. In the following text, we give a summary of each of them.

Ray tracing is the first of the three main methods. This comes in two varieties, one using long characteristics, in which the radiative transfer equation is solved along a set of rays that are traced from each source to each computational cell (e.g. Feautrier, 1964; Abel et al., 1999; Greif et al., 2010; Greif, 2014; Baczynski et al., 2015; Frostholm et al., 2018), with ray splitting or merging sometimes used to reduce the computational cost (e.g. Abel and Wandelt, 2002; Wise and Abel, 2011), and one using short characteristics, in which the radiative transfer equation is solved along a set of ray segments (one per angular direction per cell) passing through the cell centres, with initial intensities interpolated from neighbouring grid cells (e.g. Mihalas et al., 1978; Kunasz and Auer, 1988; Mellema et al., 2006; Davis et al., 2012; Mackey, 2012). Ray tracing methods based on long characteristics can be highly accurate and are particularly good at capturing the shadows cast by high density regions. However, their computational cost typically scales with the number of individual sources of radiation and hence they can become prohibitively expensive when the number of sources is large. Methods based on short characteristics can in principle avoid this expense, but are typically more diffusive (Kunasz and Auer, 1988) and can also create artificial structure in the radiation energy distribution if run with low angular resolution (Finlator et al., 2009).

Moment based radiation transport in large hydrodynamical simulations involves the solution of the radiation moment equations using some suitable closure. The most common variants of this approach are flux-limited diffusion (FLD) (see e.g. Levermore and Pomraning 1981; Turner and Stone 2001) and methods based on the M1 closure (e.g. Aubert and Teyssier, 2008; Rosdahl et al., 2013; Kannan et al., 2019), although more accurate variants also exist (e.g. Hayes and Norman, 2003). Moment-based methods that use an approximate closure (FLD or the M1 method) can be computationally efficient, particularly for problems involving many sources of radiation, but do not guarantee that radiation is always propagated in the correct direction, resulting in problems in capturing effects such as shadowing. Methods using more accurate closures generally do not have the same weaknesses, but are computationally expensive.

Monte-Carlo method is the third approach in common usage, in which probabilisitic methods are used to model the transport of individual photon packets through the gas (see e.g. Roth and Kasen 2015, Vandenbroucke and Wood 2018 and Harries et al. 2019 for examples of this approach being used for time-dependent radiation hydrodynamics problems, or Maselli et al. 2003, Ercolano et al. 2008, Dullemond et al. 2012 and Reissl et al. 2016, 2018 for examples of how it can be used as a post-processing technique). The Monte Carlo approach has a number of advantages: it generally avoids introducing grid-related artefacts into the solution, it is conceptually easy to understand, and it is also relatively easy to combine with complicated treatments of the radiation/matter microphysics, since it deals directly with the number of photons, rather than more abstract quantities such as the angular moments of the specific intensity. However, it has the disadvantage that numerical errors in the solution decrease only as the square-root of the number of photon packets, making it computationally expensive to obtain highly accurate solutions. It is also difficult to combine with highly-parallel hydrodynamical simulations. The natural way to parallelise Monte Carlo radiation transport is by partitioning the photon packets amongst the different processors, but this is efficient only if each processor has information on the full spatial distribution of the relevant gas quantities (e.g. density, chemical composition), and the memory requirements for doing this can quickly become prohibitive for large hydrodynamical simulations.

Simplex is an alternative to the three methods mentioned above. It is a variant of the short-characteristic ray-tracing since it calculates photon attenuation on the ray paths with lengths corresponding to the sizes of the simulated grid cells. Photon rays can merge within the cells, while they still preserve their original directions and resolve shadows. This behavior is advantageous in simulations with many sources, and it is also a reason why we chose this technique in our simulations. We will discuss this method in more detail in the following Chapters 4 and 5.

4 SPRAI-I: Basics of the method

This chapter is based on the article (Jaura et al., 2018) published in 2018 by Monthly Notices of the Royal Astronomical Society. The first author is me, and I wrote all the main parts of the paper and performed the simulations. S.C.O.Glover partially wrote parts regarding the chemistry module. Contributors to the final editing were also R.S.Klessen and J.-P.Paardekooper. The original stand-alone version of the SIMPLEX radiation transfer code (C++) was written by J.-P.Paardekooper. The SPRAI implementation of the SIMPLEX algorithm is a new code (C, MPI), adapted and extended by me to work with the hydrodynamical code AREPO.

In this part, we introduce our implementation of the SIMPLEX radiation transfer, describe its fundamental principles, and explain its integration into the AREPO. We include here four standard tests of the HII region expansion and discuss the usability of the code in our further work.

4.1 Introduction

Radiation feedback plays an important role in cosmic structure formation on small scales (e.g. protostellar disk fragmentation during Population III star formation; see for example Stacy et al. 2016 or Hosokawa et al. 2016) as well as on large scales (e.g. re-ionization of the universe; see e.g. Paardekooper et al. 2015, Pawlik et al. 2017, or Xu et al. 2016). Most modern hydrodynamical codes use either ray tracing, moment-based or Monte Carlo methods to calculate the ionizing radiation field in a simulated medium. However, since the computational cost of most methods scales linearly with the number of sources, simulations with many sources are computationally very expensive. Therefore, in many cases radiation is treated either in a post-processing step (Paardekooper et al., 2015), or it is coupled to hydrodynamics, but with just a small number of sources (Hosokawa et al., 2016; Stacy et al., 2016). Use of such approximations in simulations neglects local dynamical and ionization variations in the gas that can be properly resolved only for multi-frequency and multi-source ray tracing.

There are many codes and implementations available that are able to follow the ionizing radiation from different astrophysical sources. Properties and performance of the most widely used codes are summarised in code comparison projects by Iliev et al. (2006, 2009) and Bisbas et al. (2015). One of the codes that is commonly used in computational astrophysics is the moving mesh hydrodynamical code AREPO (Springel, 2010). Because of its versatility, it has been used in several large scale cosmological simulation projects like ILLUSTRIS (Vogelsberger et al., 2014), AURIGA (Grand et al., 2017) or ILLUSTRIS-TNG (Pillepich et al., 2017), as well as numerous small-scale simulations, ranging from the formation of the first stars (Greif et al., 2011a) to the formation of structures in present-day molecular clouds

(Smith et al., 2016). Although various efforts have been made to add radiation transfer to AREPO (e.g. Petkova and Springel, 2011; Greif, 2014; Bauer et al., 2015), none of the current implementations is suitable for computationally challenging multi-source simulations where radiation feedback plays an important part in structure formation. Since our future work in the field of first star formation will involve such environments, it is our priority to develop a radiative transfer method that will address this challenge.

In this chapter we introduce an alternative method for ray tracing, SIMPLEX, that we implement in AREPO. The SIMPLEX method was originally developed for use with static Voronoi grids and is described and analyzed in Ritzerveld and Icke (2006), Paardekooper et al. (2010) and Kruip et al. (2010). Our implementation is the first time that the method has been used on-the-fly within a hydrodynamical simulation, and takes advantage of the moving mesh already present during the hydrodynamical calculations of the AREPO code. This makes the combination of the two concepts easier and more efficient.

A characteristic feature of the SIMPLEX method is that the computational cost does not scale with the number of sources, as is the case for conventional ray-tracing algorithms. Sources in SIMPLEX only inject new photons into corresponding grid cells. All photons on the grid are subsequently transferred from cell to cell in a sequence of radiation transfer steps. From the movement of photons one can than calculate the corresponding fluxes and ionisation rates in each cell. The collective transfer of photons during the radiation transfer makes this method especially useful in simulations with a high number of sources.

This chapter is structured as follows. In Section 4.2, we describe details of the SIMPLEX method and its coupling to a primordial chemistry network. Section 4.3 shows how the code performs for some standard test problems (e.g. the growth of the ionization front in uniform density gas in the R-type or the D-type regime). In the final Section 4.4, we summarise our results and give an overview of our future plans.

4.2 Description of the method

SPRAI is based on the SIMPLEX radiative transfer method developed by Ritzerveld and Icke (2006), Paardekooper et al. (2010) and Kruip et al. (2010) and used in Paardekooper et al. (2015). This method was previously used only for post-processing results from hydrodynamical simulations of cosmic structure formation. The original SIMPLEX code uses its own integrated chemistry model that includes ionization, recombination and cooling of hydrogen and helium in several frequency bins.

Our implementation of the radiative transport (RT) of ionizing photons in AREPO (Springel, 2010) is based on the updated version of the original SIMPLEX algorithm discussed in Paardekooper et al. (2010). In our implementation, the photon transfer is now calculated directly on the Voronoi mesh created in AREPO, rather than on a mesh created during a post-processing step. From the photon transfer, we obtain photon fluxes in each cell, and from these we can derive the corresponding ionization and heating rates. These rates are subsequently used by a separate chemistry module to update the chemical and thermal state of the gas. In the following sections we will introduce physical and numerical aspects of the radiation transfer as well as the chemistry module.

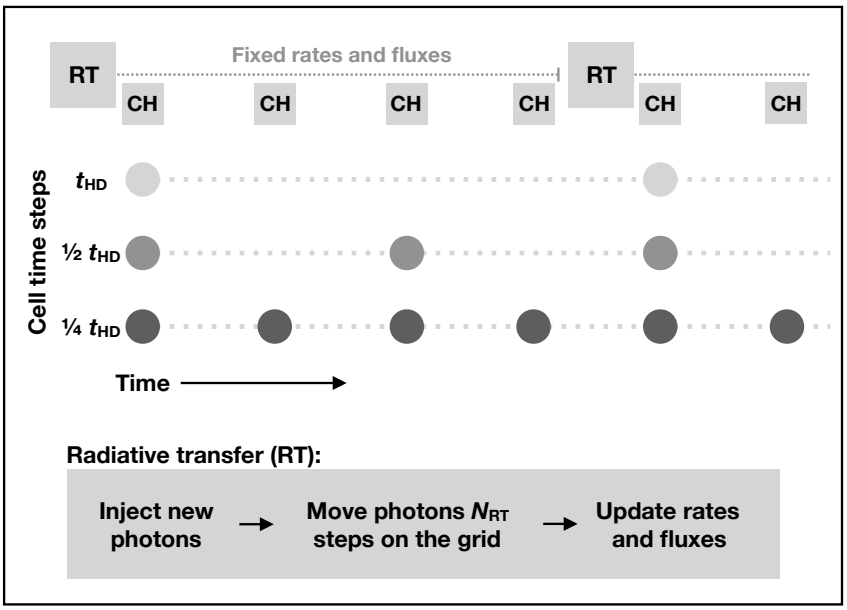

Figure 4.1: Schematic structure of the SPRAI implementation. RT is computed at the end of each full hydrodynamical step t_{HD}, when all cells are synchronised and the complete Voronoi mesh is available. The calculated rates and fluxes are stored and used by the chemistry module (CH) during subsequent hydrodynamical steps.

4.2.1 Photon transfer

The original SIMPLEX algorithm was discussed in Paardekooper et al. (2010) and mathematical analysis of the method[1] was studied by Kruip et al. (2010). In this section we will focus on our implementation which is adapted to work with the AREPO code.

AREPO is a multipurpose and multi-physics hydrodynamical code developed by Springel (2010) and it is well established in the astrophysical community. In comparison with conventional Eulerian codes with static or adaptive meshes, AREPO uses a Voronoi mesh that is constructed at each step from a set of mesh generating points that move with the gas flow. Once the Voronoi mesh is constructed, AREPO calculates fluxes and gradients between cells and updates the cell values accordingly. An advantage of this method is that such a Voronoi mesh follows the underlying gas structure and effectively reduces grid artefacts that can arise from conventional mesh codes. Besides that, AREPO uses adaptive time stepping that reduces computational time of the simulation.

In Figure 4.1 we show a schematic description of our implementation. Since construction and maintenance of the Voronoi mesh is already an integral part of the AREPO code, it can be easily used for SIMPLEX photon transport calculations. A complete mesh is constructed only on time steps when all gas cells are synchronised. This means that the radiation transport in

[1] The transfer method that we use is a modified version of the direction-conserving transport (DCT) method discussed in the paper of Kruip et al. (2010)

all cells can occur only at full hydrodynamical (HD) steps $t_{\rm HD}$. During HD sub-steps when only some cells are active we keep the ionization rates and radiation fluxes fixed[2]. When modelling D-type ionization front (I-front), this limitation is usually unimportant, as in this case the time taken for the front to propagate from one cell to the next is typically of the order of $t_{\rm HD}$. However, when modelling R-type fronts, which can propagate through many cells during a single hydrodynamical timestep, this limitation is potentially more significant. In practice, because we ensure that the number of photons absorbed in a cell during a single RT step cannot exceed the number of H atoms and H_2 molecules available for ionization (see Equation 4.8 below), we find that we recover the correct I-front propagation velocity provided that the recombination time $t_{\rm rec} \gg t_{\rm HD}$, as our tests in Section 4.3.1 demonstrate. In cases where this condition is not satisfied, it is necessary to limit the size of the hydrodynamical timestep, as in Baczynski et al. (2015).

At the beginning of each RT calculation we find all sources (ideal sources, stars, sink particles, ...) and calculate their immediate photon emission rates[3]. For each source we find the nearest gas cell and assign to it the number of photons emitted by the source during $t_{\rm HD}$. Then we move photons on the Voronoi grid from cell to cell and calculate the ionization rates and radiation fluxes due to these photons as described in Section 4.2.2. One RT step is a movement of photons from one cell to a neighbouring cell. The number of RT steps $N_{\rm RT}$ depends on the ionization state of the gas through which the photons are passing. In general, the photons are propagated until they are completely attenuated in the gas.

It is important to note that in the present version of the method, we do not constrain the distance that the photons can propagate during $t_{\rm HD}$, i.e. we treat the speed of light as if it were infinite. For many applications, this is a reasonable approximation, but it may potentially cause problems in large cosmological simulations with the box sizes $L \gg c\ t_{\rm HD}$, where c is the speed of light.

The number of photons associated with each mesh cell, as well as the ionization rates and radiation fluxes are stored directly on the mesh. Each cell of the mesh has information about the number of photons that are passing through its volume, as well as their direction. For numerical convenience we define a set of $N_{\rm dir}$ solid angles (directional bins) equally distributed over the sphere using simulated annealing. During the transfer, photons are moved from a directional bin of an initial cell to the corresponding directional bin of a destination cell. The photons are spatially moved, but their direction stays the same. We distinguish two types of photon transport, directional and isotropic. Both types are schematically described for a 2D Voronoi mesh in Figure 4.2; the behaviour in 3D is similar, but harder to visualize.

Directional transport is used to transfer photons in a particular direction. Since the Voronoi mesh is not regular, it is not possible to move photons on straight lines defined by the directional vectors. Instead, we look for the most straightforward path along the particular directional bin (bottom panel). First we randomly choose a directional vector (red arrow) from the given solid angle $\Omega_{\rm dir}$ (red cone). This is done in order to prevent

[2] In principle one could also use a partially constructed mesh during HD sub-steps to update radiation fields in regions that require higher precision. However, this introduces several non-trivial challenges to the current algorithm that we will try to address in the future.

[3] In Section 4.3, we use only ideal monochromatic sources with fixed ionization rates. However, the method can easily be extended to handle more realistic source spectra.

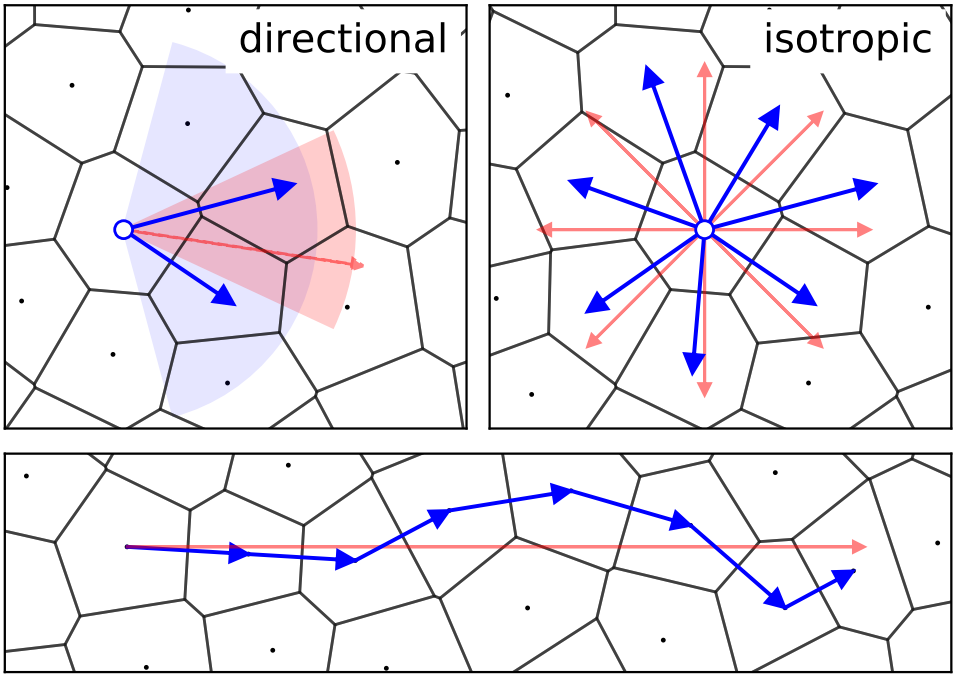

Figure 4.2: The two types of the photon transport used in SPRAI, directional and isotropic. For ease of visualization, the methods are shown here using a 2D Voronoi mesh, but they work in a similar fashion in 3D. Red arrows denote directional bin vectors and blue arrows show photon paths during the transport. The red cone depicts the solid angle Ω_{dir} of the directional bin from which a random directional vector is chosen. The blue cone is the solid angle Ω_θ from which we choose most straightforward photon paths along the directional vector. The bottom panel shows a possible sequence of photon paths along the original direction. Please see the text for a further explanation of the panels in this figure.

preferred paths on the grid and add some scatter to the photon beam. Then we look for three[4] neighbour cells for which the angles between their path vectors (blue arrows) and the directional vector are the smallest, and redistribute initial photons between them. By varying the solid angle Ω_θ (blue cone) we can exclude those paths which diverge too much from the original direction[5].

Isotropic transport is similar to directional transport, but it is performed only for cells with sources. At the beginning of a RT step we calculate the number of new photons from the source emission rate and distribute them equally into each directional bin of a cell. In this case we compute random directional vectors (red arrows) for each directional bin (cones are not shown). Then we find all neighbourhood cells and compute their path vectors (blue arrows). In the last step we find for each directional vector the closest path vector and assign its photons to the corresponding directional bins of a neighbour cell.

4.2.2 Radiation field

In contrast with the original SIMPLEX code that updates chemistry after each photon step, our implementation of the SPRAI code first calculates a static ionization rate field and then passes it to an independent chemistry module. The module is similar to the one used in the radiative transfer module for the magnetohydrodynamical adaptive mesh refinement code FLASH-4 (FERVENT) (Baczynski et al., 2015). We divide ionizing photons into two energy bins:

$$13.6 \text{ eV} < \gamma_{13.6+} < 15.2 \text{ eV},$$

$$15.2 \text{ eV} < \gamma_{15.2+}$$

Photons in the 13.6+ bin can ionize atomic hydrogen but not molecular hydrogen. Photons in the 15.2+ bin can ionize both H and H_2. We therefore have three possible reactions:

$$\mathrm{H} + \gamma_{13.6+} \rightarrow \mathrm{H}^+ + e^-$$

$$\mathrm{H} + \gamma_{15.2+} \rightarrow \mathrm{H}^+ + e^-$$

$$\mathrm{H}_2 + \gamma_{15.2+} \rightarrow \mathrm{H}_2^+ + e^-.$$

We further assume (as in Baczynski et al., 2015) that all of the H_2^+ ions formed by the third reaction are immediately destroyed by dissociative recombination:

$$\mathrm{H}_2^+ + e^- \rightarrow \mathrm{H} + \mathrm{H}.$$

We note that it is easy to extend the number of energy bins to treat e.g. helium photoionization, or the ionization of metal atoms in the present-day ISM. The method can also be extended to model the photodissociation of H_2 by Lyman-Werner photons. However, the test problems in this chapter are restricted to the simple ionization of hydrogen gas by photons with energies above 13.6 eV. Multifrequency tests will be included in subsequent Chapter 5.

[4]For clarity, in Figure 4.2 we show only two neighbour paths.

[5]This can happen if the number of directional bins $N_{\rm dir}$ is small, as in that case $\Omega_{\rm dir}$ is large. In general, it is enough to exclude only backwards directions and set $\Omega_\theta = 2\pi$ sr.

As already discussed in the previous section, the chemistry of the gas is computed for any active mesh cells on each hydrodynamical sub-step, whereas the radiation field is updated only on full hydrodynamical steps $t_{\rm HD}$. To account for this, we could in principle introduce an additional restriction on the AREPO timestep to prevent the ionization state of the gas from changing too quickly. In practice, we have not found this to be necessary for the tests presented in this chapter.

Photons in the system do not keep information about their previous path and therefore their attenuation in the gas has to be calculated locally for each cell. The number of photons N_α^γ from the frequency bin γ that are attenuated by the species α is calculated as

$$N_\alpha^\gamma = N_{\rm in}^\gamma \left(1 - e^{-d\tau^\gamma}\right) \frac{\langle\sigma_\alpha^\gamma\rangle x_\alpha}{\Sigma^\gamma}, \tag{4.1}$$

where $N_{\rm in}^\gamma$ is the number of photons coming in to the cell, $\langle\sigma_\alpha^\gamma\rangle$ is the mean absorption cross-section, x_α is the mass fraction of the species in the cell and the optical depth,

$$d\tau^\gamma = dn\Sigma^\gamma, \tag{4.2}$$

is summed over all species $\Sigma^\gamma \equiv \sum_\alpha \langle\sigma_\alpha^\gamma\rangle x_\alpha$. We calculate values for the mean cross-sections $\langle\sigma_\alpha^\gamma\rangle$ and mean deposited energies $\langle E^\gamma\rangle$ (see below) in the same way as in Baczynski et al. (2015). However, in the tests in this chapter, we use fixed values for these quantities, for simplicity. The column density of nucleons in the cell,

$$dn = n_{\rm cell}\langle dr\rangle, \tag{4.3}$$

is calculated from the mean distance[6] $\langle dr\rangle$ to the neighbouring cell and the nucleon number density,

$$n_{\rm cell} = \frac{\rho_{\rm cell}}{m_{\rm p}(1 + 4\,Y_{\rm He})}, \tag{4.4}$$

where $\rho_{\rm cell}$ is the mass density of the cell, $m_{\rm p}$ is the proton mass, and $Y_{\rm He}$ is the fractional abundance of He in the gas.

From the number of attenuated photons N_α^γ and the number of species α available for the reaction in the cell volume $V_{\rm cell}$ at the beginning of the RT,

$$\mathcal{N}_\alpha = n_{\rm cell}\, x_\alpha\, V_{\rm cell}, \tag{4.5}$$

we can calculate the corresponding reaction rate

$$k_\alpha = \sum_\gamma k_\alpha^\gamma = \sum_\gamma \frac{N_\alpha^\gamma}{\mathcal{N}_\alpha} \frac{1}{t_{\rm HD}}, \tag{4.6}$$

[6]We can assume spherical shapes of cells since the particle mesh in AREPO code is regularised. All mesh-generating points are automatically moved to the center-of-mass of their cells, so that the shape of cells is more regular and volumes of the neighbours are very similar.

where $t_{\rm HD}$ is the time of the previous full hydrodynamical step. Given the average deposited energy $\langle E^\gamma \rangle$ for the reaction, we can also calculate for each species a total heating rate

$$\Gamma_\alpha = \sum_\gamma k_\alpha^\gamma \langle E^\gamma \rangle. \tag{4.7}$$

Values of k_α and Γ_α are stored for each cell and used by the chemistry module.

When dealing with photons in multiple direction bins entering a mesh cell, the fact that the equations above are linear in $N_{\rm in}^\gamma$ means that we can proceed in one of two ways. We can compute individual values of k_α and Γ_α for each direction bin, and then simply sum them to get the final values for the mesh cell. Alternatively, we can sum the incident photons to get a single value of $N_{\rm in}^\gamma$ for the mesh cell and then use this to calculate k_α and Γ_α for the mesh cell, as above. The only complication in this case is the need to account for the fact that the photons lost in the cell, N_α^γ, are spread over multiple directional bins. The linearity of the equations means that both approaches yield identical results for the final values of k_α and Γ_α. In our current implementation, we have chosen to use the latter approach.

In our calculations we constrain the number of photons entering the reaction by the total number of species available for reactions[7],

$$N_\alpha^\gamma = \begin{cases} N_\alpha^\gamma & \text{if } N_\alpha^\gamma < \mathcal{N}_\alpha \\ \mathcal{N}_\alpha & \text{if } N_\alpha^\gamma \geqslant \mathcal{N}_\alpha, \end{cases} \tag{4.8}$$

where $\mathcal{N}_\alpha$ is the number of available species α in the cell at the current RT step. If the number of photons entering the cell $N_{\rm in}^\gamma$ is larger than the number of atoms or molecules available to ionize, the excess photons are transferred together with the unattenuated photons to the next cell.

The calculations described in this section are photon conserving. However, in order to enhance the computational performance of the code we stop calculations when the number of photons is too small. If the number of photons leaving the cell $N_{\rm out}^\gamma = N_{\rm in}^\gamma - \sum_\alpha N_\alpha^\gamma$ is smaller than some threshold value $N_{\rm th}$, then we do not transfer them further to the neighbouring cells, but instead remove them from the system. In our simulations we set the threshold value four orders of magnitude lower than the number of available species in the particular cell, so that $N_{\rm th} \ll \sum_\alpha \mathcal{N}_\alpha$ and the photon loss is minimized.

4.2.3 Chemistry

The chemical evolution of the gas is calculated separately for each cell after the end of the RT step, using as an input the photoionization rates calculated during the RT step (see Section 4.2.2 above). To model the chemical evolution, we use the primordial chemistry network that is available as part of the SGCHEM chemistry module (SGCHEM) in AREPO. This network was originally implemented in AREPO by Hartwig et al. (2015) and is based on earlier work by Glover and Jappsen (2007), Glover and Abel (2008), Clark et al. (2011b) and Glover

[7] It is necessary to mention that the total number of available species for reaction should also include species created during the recombination in the cell. Since the recombination is treated later in the chemistry module we neglect it at this point. Nevertheless, for large $t_{\rm HD}$ this contribution might become important.

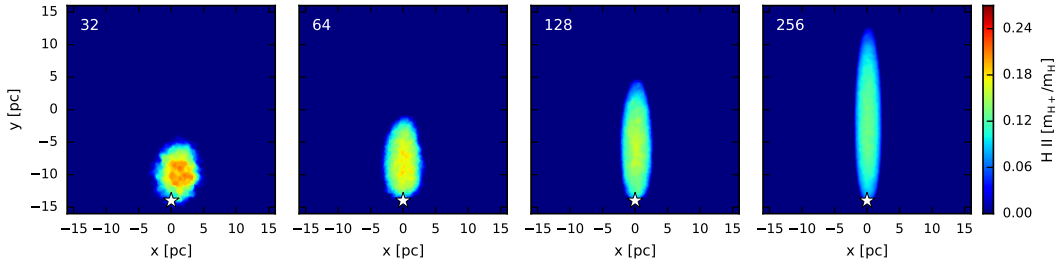

Figure 4.3: Mass-weighted projection of ionised hydrogen gas in the box produced by a single photon ray. Positions of sources are marked with stars and a single directional bin is orientated along the y-axis. Plotted rays are in an early stage of their growth. At later times all rays reach the upper border of the box, although their widths remain different.

(2015a). We also include several improvements to the treatment of He^+ recombination and H^- photodetachment described in Schauer et al. (2017b). As previously noted, when we include H_2 photoionization in this network, we follow Baczynski et al. (2015) and assume that in the conditions in which this process is important, all of the resulting H_2^+ ions will be almost immediately destroyed by dissociative recombination, yielding atomic hydrogen, so that the net effect is:

$$H_2 + \gamma \rightarrow H_2 + e^- \rightarrow H + H. \tag{4.9}$$

We solve for the thermal evolution of the gas due to radiative heating and cooling at the same time as the chemical evolution. We use the cooling function presented by Glover and Abel (2008) and updated by Glover (2015a). We also account for the heating due to the photoionization of H and H_2, which is computed as described in Section 4.2.2.

We note that in principle, SPRAI is not restricted to modelling photoionization in metal-free gas and that it would be a relatively simple matter to couple the scheme to a present-day chemical model of the kind used e.g. in Baczynski et al. (2015). However, this lies outside the scope of the present chapter.

4.2.4 Behaviour of photon rays on a Voronoi grid

Properties of the photon rays generated by SIMPLEX vary for different resolutions. In Figure 4.3, we show results of a single ray ionization. In this setup we placed an ideal source similar to that in Test 1 at the bottom of a box filled with hydrogen gas, at coordinates (x,y,z) = (0, -14, 0). We enabled only one directional bin pointing in the direction of the y axis and switched on the ionizing source. From the plot, we can see that the thickness and length of the ray depends significantly on the resolution. This is due to the fact that photons emitted from the sources are not moving on straight lines. Instead, they experience random side-shifts which depend on the size of the individual grid cells. Since the mean diameter of the cells for resolution 32 is eight times bigger than for resolution 256, photons rays are able to ionise gas further from the original directional axis. The length of the ray varies because low resolution cells contain more gas that can be ionised and therefore the same number of photons is used up closer to the source.

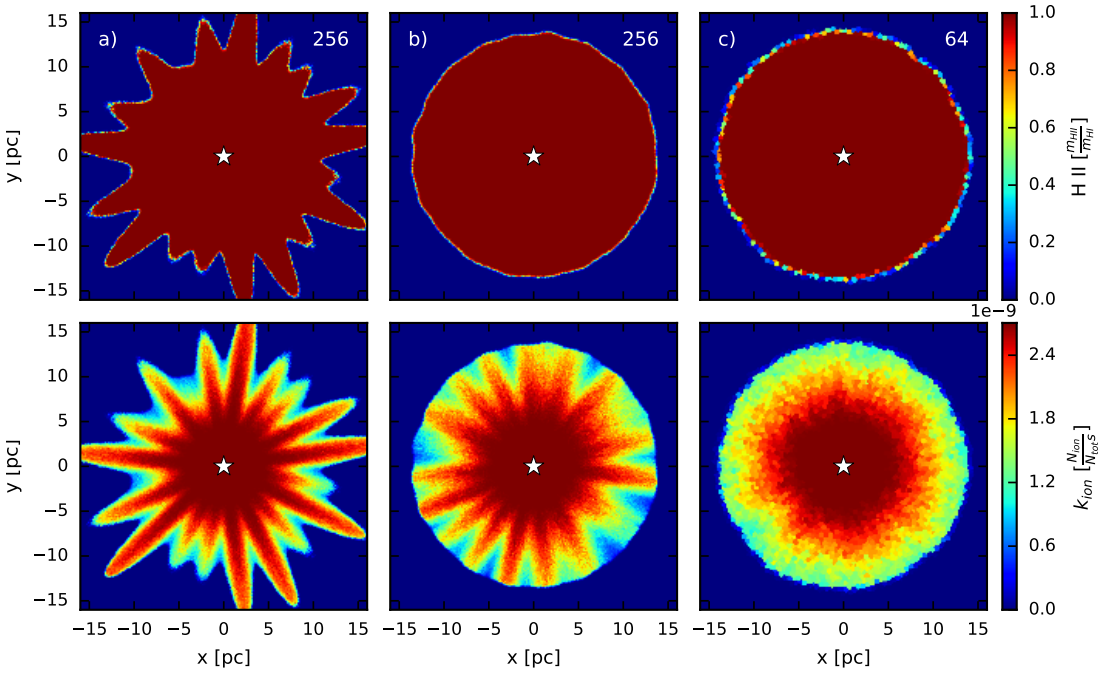

Figure 4.4: Effect of variable ray widths on the shape of a Strömgren sphere. The top panels show the mass fraction of ionised gas and the bottom panels the corresponding instantaneous ionization rate at time t=2.4 kyr for resolutions 256 and 64. In simulation a) a set of directional bins is fixed for all RT runs, whereas in simulations b) and c) the directional base is rotated five times per radiational transfer. The plots show slices through the box in the plane $z = 0$.

Test		$T_{\rm gas}$ [K]	$n_{\rm H}$ [cm^{-3}]	$L_{\rm box}$ [pc]	γ	$\dot{N}$ [ph/s]	$t_{\rm rec}$ [yr]	$R_{\rm St}$ [pc]
1	R-front	100	0.001	1.28×10^4	1.0001	10^{49}	1.22×10^8	6.79×10^3
2	D-front	100	0.001	3.2×10^4	5/3	5×10^{48}	1.22×10^8	5.39×10^3
3	r^{-2}	100	100	13	1.0001	10^{49}	1.22×10^3	3.15
4	Blob test	1000	1	32	5/3	1.62×10^{48}	1.22×10^5	36.95

Table 4.1: Summary of the parameters used in different tests

Behaviour of rays at high resolutions results in an inhomogeneous distribution of photons far from the source and subsequent deformation of the I-front. In Figure 4.4a, we plot a $z = 0$ slice through the box of an R-type I-front simulation similar to Test 1 (but with a higher gas density and much smaller box) at time t=2.4 kyr and resolution 256. The top panel shows the ionised hydrogen fraction and the bottom panel the corresponding ionization rate. As we can see, although the I-front should be circular, given the symmetry of the problem, in practice it develops pointed features orientated parallel to the directional bins within the plane. At lower resolution, these feature are not present, because photon rays are able to overlap with each other (see Figure 4.4c). However, with increasing resolution, the radius of the overlap gets closer to the source and these features become visible.

There are several ways to deal with this problem. One solution is to increase number of directional bins. The higher the number, the smaller the angle between two neighbouring photon rays, meaning that rays continue to overlap out to greater distances from the source. Nevertheless, it is important to note that using larger numbers of directional bins implies the use of more memory and the need for more calculations per cell.

Another solution is to construct the total ionsisation field from a set of randomly rotated partial fields. In practice, this means that we divide the total number of photons at the beginning of the RT by $N_{\rm rot}$, and for each part perform separate radiation transfer. Summing the resulting $N_{\rm rot}$ fields gives the final field that is provided to the chemistry module. Results of a simulation using this method are plotted in Figure 4.4b. Note that the instantaneous ionization rate on the figure is still not completely homogeneous, but since the whole field is rotated $N_{\rm rot}$ times during each RT run, the time average of the resulting ionization rate is homogeneous and I-front features are effectively suppressed. In general for higher resolutions one needs to do more rotations for the same number of $N_{\rm dir}$. Also this method requires more RT steps and therefore increases the required computational time.

4.3 Tests and results

In this section, we present results from a set of standard tests to verify the accuracy of our implementation. The first test is a simple expansion of an HII region in a homogeneous environment. For this test, we disable photoionization heating and keep the gas temperature constant, allowing us to examine the behaviour of the I-front in the R-type regime. In the second test, we re-enable photoionization heating and allow the gas temperature to vary, enabling us to study the behaviour of the I-front in the D-type regime, where the propagation of the front is sensitive to the dynamical response of the gas. The setup of the third test is similar to Test 1, but instead of a homogeneous environment we select a radial density

gradient proportional to $1/r^2$ for the gas (a setting similar to the Bonnor-Ebert sphere (BES)). In the last test we study the formation of a shadow behind a dense clump irradiated by two sources. Initial parameters and values for all of our test simulations are summarised in Table 4.1. At the end of this section we discuss comparison of simulation times for different numbers of sources and resolutions.

In all of the tests, we use a directional base with $N_{\rm dir} = 128$ bins, solid angle $\Omega_\Theta = 2\pi$ sr and the ionization rate is integrated from $N_{\rm rot} = 5$ rotations of the directional base. The mesh cells in our initial conditions are created using uniform Poisson sampling, and the mesh is relaxed prior to the run, so that all cells have approximately similar masses and shapes. For the tests below, we do not use any mesh refinement criteria, but in principle these could easily be combined with the basic algorithm.

4.3.1 Test 1: R-rtype expansion of an HII region

In the first test we look at the rarified-type (R-type) expansion of a single HII region in a homogeneous gas environment with four different resolutions: 32^3, 64^3, 128^3 an 256^3 cells. (For brevity, we refer to these hereafter simply as resolutions of 32, 64, 128 and 256, respectively).

Expansion of an HII region is a well known problem. Strömgren (1939) showed that in ionization equilibrium, a point source of ionizing photons in an uniform density gas of pure hydrogen creates a spherical HII region with radius:

$$R_{\rm St} = \left[\frac{3\dot{N}_\gamma}{4\pi\alpha_{\rm B}(T)n_{\rm e}^2}\right]^{1/3}, \tag{4.10}$$

where $\alpha_{\rm B}(T)$ is the case-B recombination coefficient of hydrogen, and $n_{\rm e}$ is the electron number density. If the gas inside the HII region is almost entirely ionized, then $n_{\rm e} \simeq n_{\rm H}$, the H atom number density of the undisturbed gas. Provided that the density of the ionized gas remains approximately constant, the time evolution of the ionization front (I-front) radius can be parametrised as

$$R_{\rm I}(t) = R_{\rm St}\left(1 - e^{-t/t_{\rm rec}}\right), \tag{4.11}$$

where the recombination time is calculated as

$$t_{\rm rec} = [\alpha_{\rm B}(T)n_{\rm H}]^{-1}. \tag{4.12}$$

In order to directly compare our implementation with the FERVENT code we use the same initial conditions as in the R-type test of Baczynski et al. (2015). Our simulation runs in a 3D box of size $L_{\rm box} = 12.8$ kpc with periodic boundary conditions. A single idealised source with photon emission rate $\dot{N}_\gamma = 1 \times 10^{49}$ photons per second is located at the centre of the box. The box is filled with a homogeneous gas with number density $n_{\rm H} = 10^{-3}$ cm^{-3}. We assume that the initial gas in the box consists only of neutral hydrogen ($x_{\rm H^+} = 0$) and has initial temperature $T_{\rm i} = 100$ K. Since in this test we are not interested in the density response of the gas, we assume a quasi-isothermal equation of state where $\gamma = 1.0001$, to keep the

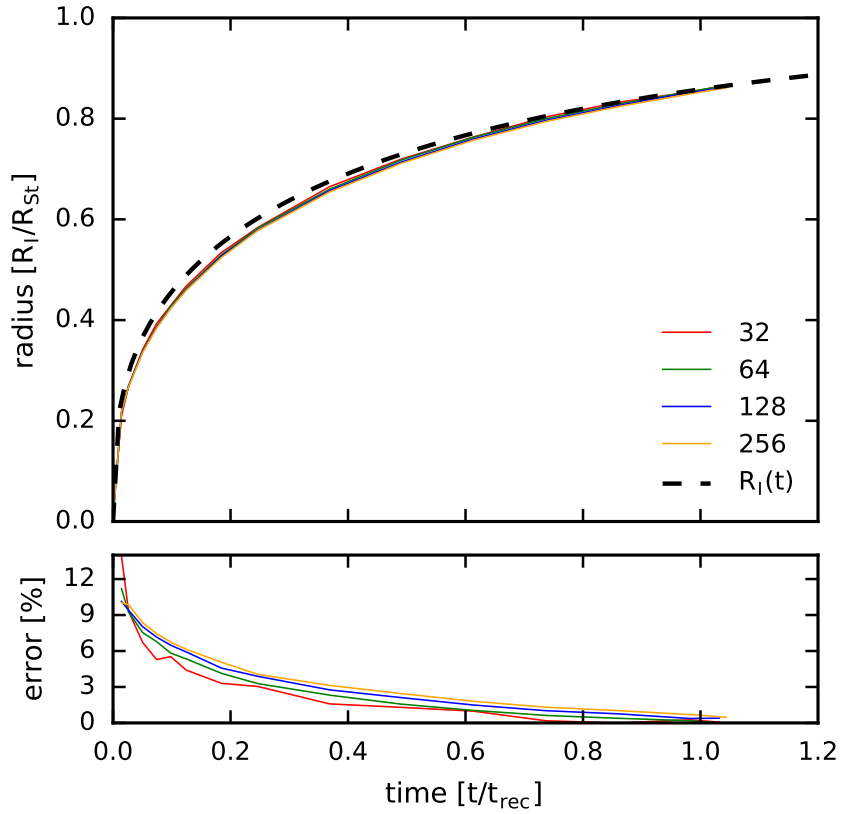

Figure 4.5: Results of Test 1: time evolution of the radius of the HII region, R_{I} (top) and its deviation from the analytical solution (bottom). Coloured lines represent results of our simulations with different resolutions: 32, 64, 128 and 256. The black dashed line shows the values given by Equation 4.11. In this test we use the maximal time step of $t_{\mathrm{HD}} = 0.3$ Myr.

pressure constant across the ionization front. Besides that, we also fix the recombination rate coefficient to $\alpha_{\mathrm{B}} = 2.59 \times 10^{-13}$ cm^3 s^{-1} and the photoionization cross-section of the hydrogen to $\sigma_{\mathrm{H}} = 6.3 \times 10^{-18}$ cm^2. These values lead to a Strömgren sphere with radius $R_{\mathrm{st}} \approx 6.79$ kpc and the recombination time $t_{\mathrm{rec}} \approx 122.34$ Myr.

The time dependent evolution of the I-front for all four resolutions (solid lines) as well the analytic solution (dashed line) for the I-front radius R_{I} are shown in Figure 4.5. In the bottom panel, we plot the relative error between the simulated and analytical radius. From the figure we can see that the I-front in the simulations closely follows the analytical solution. Significant errors are only visible in the initial stage but with increasing time this difference decreases. This is due to the relatively coarse time resolution of the radiative transfer, which is restricted by the time interval of the highest hydrodynamical step. From Figure 4.6 we see that the error in the I-front radius decreases as we decrease the time step t_{HD}. Overall, our results match very well with the results of Baczynski et al. (2015).

In Figure 4.7 we plot the mass fraction of ionised hydrogen in the plane $z = 0$ for each

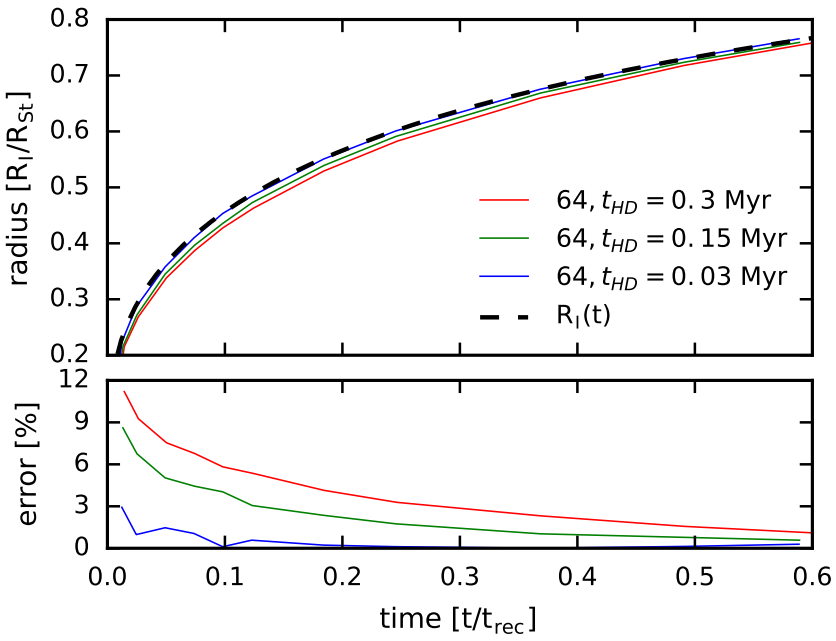

Figure 4.6: Results of Test 1: the time evolution of the radius of the HII region for different values of $t_{\rm HD}$. In this figure we plot only the initial stages of the test with resolution 64. The radius of the I-front converges to the analytical solution $R_{\rm I}$ as $t_{\rm HD}$ decreases. For other resolutions, we observe similar behaviour.

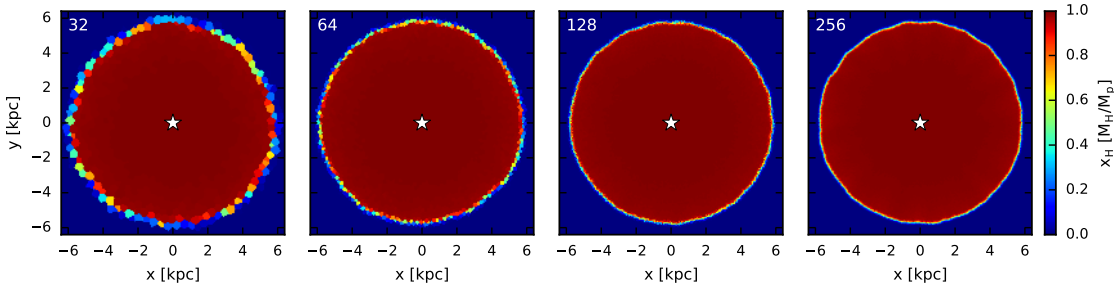

Figure 4.7: Results of Test 1: mass fraction of the ionised gas in the z=0 plane. Results are for all simulated resolutions 32, 64, 128 and 256 at time t=75 Myr. The white star marks the position of the ionizing source.

Resolution	32	64	128	256
Mean cell size [pc]	400	200	100	50
I-front width [pc]	477.5	329.5	204.4	193.6
Mean number of cells	1.19	1.65	2.04	3.87

Table 4.2: Comparison of the I-front widths for different resolutions corresponding to Figure 4.7 . The width of I-front is calculated as the difference between radii where the ionization drops from 90% to 10%. We give also the average number of cells that cover this radial difference.

resolution. In the lowest resolution case we can clearly distinguish the cell structure of the Voronoi mesh. This is especially visible at the edge of the ionization front. With increasing resolution, these features disappear and the I-front itself gets thinner. From the initial parameters of this test we can calculate the mean free path of the photons traveling through the gas as $l = (n_{\rm H}\sigma_{\rm H})^{-1} \approx 51.4$ pc. Provided that the photons on their way to the I-front move on non-straight paths we expect that the width of the I-front will be scattered on scales of the order of a few l. From the Table 4.2 we see that with the increasing resolution the width of the I-front converges to the value of $4l \approx 200$ pc, which corresponds with our expectations.

4.3.2 Test 2: D-type expansion of an HII region

In the previous test we simulated the quasi-isothermal case of the HII region expansion. In this test we allow ionising photons to heat the gas. Any change of the temperature increases the gas pressure around the source. Initially, the ionization front propagates so rapidly that the gas has no chance to respond hydrodynamically to this increase in pressure. However, once the speed of the I-front drops below $2c_{\rm s}$, where $c_{\rm s}$ is the speed of sound in the ionized gas, the expansion of the gas causes a shock to separate from the I-front and proceed it into the surrounding neutral gas. Once this occurs, we describe the ionization front as a density-type (D-type) front.

Due to the dynamical response of the matter, the position of the I-front is no longer given by Equation 4.11. Instead it enters as (Spitzer, 1978b)

$$R_{\rm Sp}(t) = R_{\rm St}\left(1 + \frac{7}{4}\frac{c_{\rm s}t}{R_{\rm St}}\right)^{4/7}, \tag{4.13}$$

where the speed of the sound $c_{\rm s}$ can be calculated from the average temperature $T_{\rm avg}$ in the ionised gas as

$$c_{\rm s} = \sqrt{\frac{\gamma k_{\rm B} T_{\rm avg}}{m_{\rm H}}}, \tag{4.14}$$

where $k_{\rm B}$ is the Boltzmann constant and in case of a pure hydrogen gas with atomic weight $m_{\rm H}$ we use $\gamma = 5/3$.

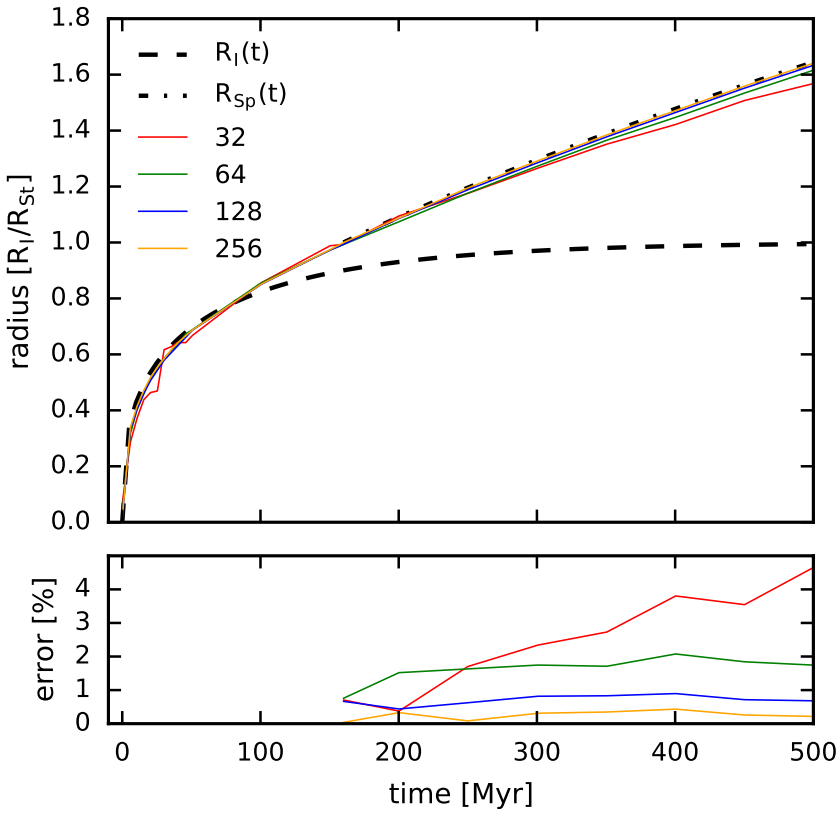

Figure 4.8: Results of Test 2: Time evolution of the D-type I-front for resolutions 32, 64, 128 and 256. The black dashed line shows the values given by Equation 4.11. The black dashed-dotted line is the Spitzer radius, computed assuming an average HII region temperature $T_{\rm avg} = 1.1 \times 10^4$ K. The Spitzer solution is calculated from the time $t \approx 160$ Myr when the radius of the I-front first reaches the Strömgren radius. In the bottom panel, we plot the fractional amount by which each simulation differs from the analytical Spitzer solution.

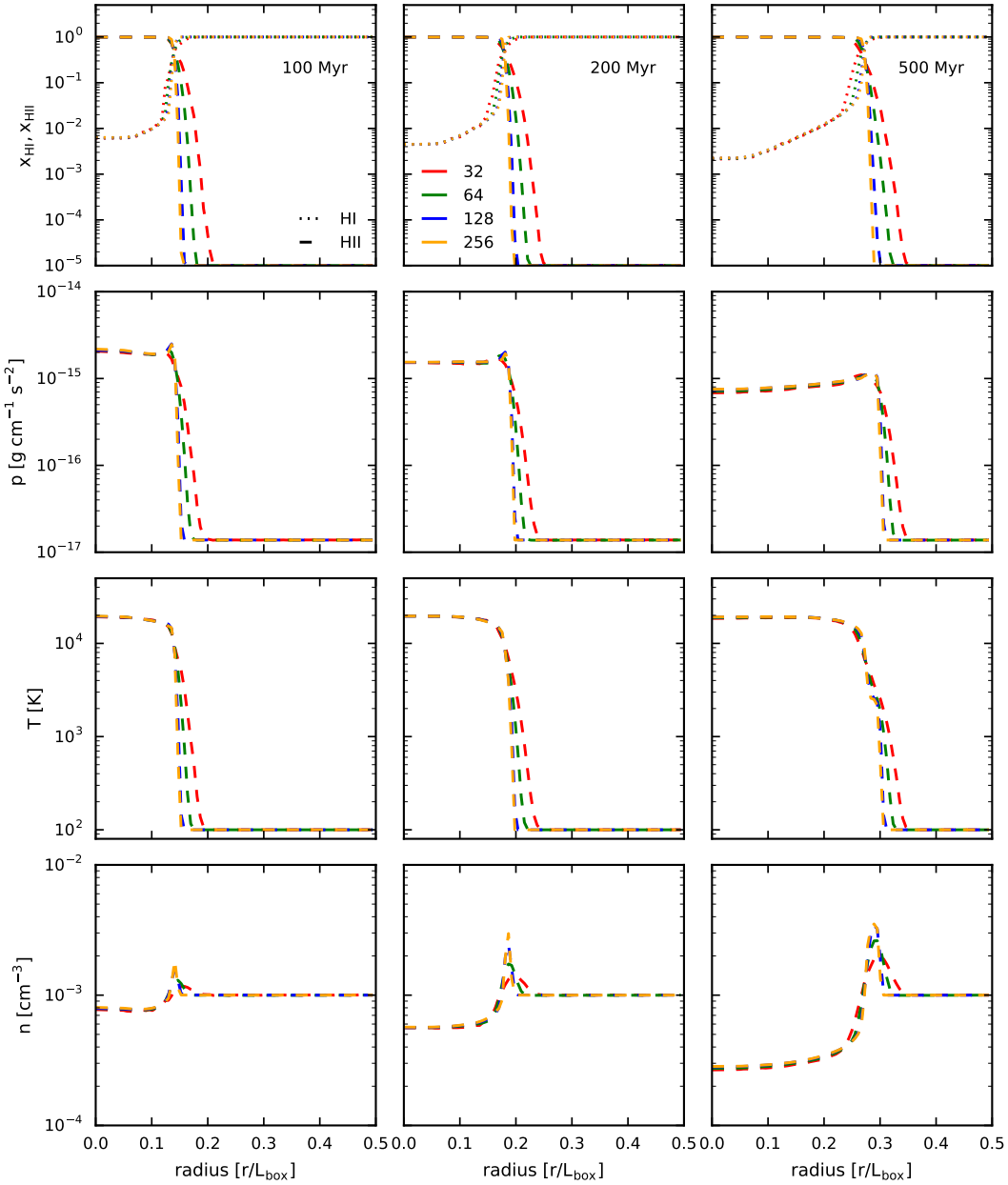

Figure 4.9: Results of Test 2: various properties of the gas at times 100, 200 and 500 Myr as functions of distance from the star. In the first row we plot mass fraction of neutral and ionised hydrogen. The second, third and fourth rows show pressure, temperature and the proton density of the gas, respectively.

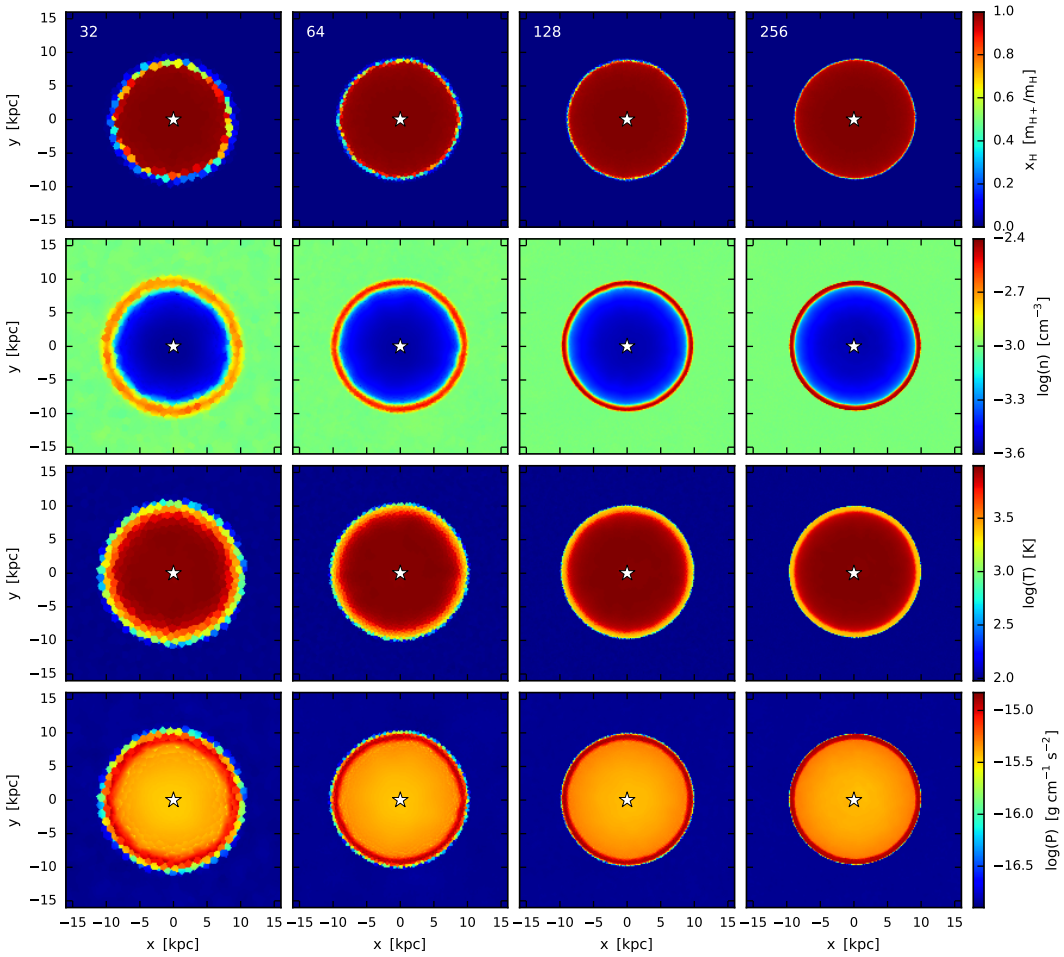

Figure 4.10: Results of Test 2: slices through the simulated box in the plane $z = 0$ at time $t = 500$ Myr. From the top to the bottom, the rows show the mass fraction of ionised gas, the temperature, the proton number density and the pressure of the gas, respectively. From left to right, the columns show results for different resolutions: 32, 64, 128 and 256, respectively.

Initial conditions for this test are similar to the D-front simulation (Test 5) of Iliev et al. (2009). In our case we put an ideal ionization source $\dot{N}_\gamma = 5 \times 10^{48}$ s^{-1} into the centre of a box with $L_{\rm box} = 32$ kpc [8]. The box is filled with neutral hydrogen gas with initial density $n_{\rm H} = 10^{-3}$ cm^{-3} and temperature $T = 100$ K. Each ionization event deposits an energy of 2 eV to the corresponding gas cell. The values of $\alpha_{\rm B}$ and $\sigma_{\rm H}$ are fixed to the same values as in the Test 1. The corresponding Strömgren radius and recombination time for these values are $R_{\rm St} = 5.4$ kpc and $t_{\rm rec} = 122.4$ Myr, respectively. In order to see the later stages of the I-front evolution we run the simulation for $4 \times t_{\rm rec} \approx 500$ Myr.

The time evolution of the I-front for all four resolutions is shown on Figure 4.8. The dashed black line indicates the Strömgren radius and the dashed-dotted line is the Spitzer solution. The coloured lines are results for each resolution, where the I-front is defined as a radial distance from the source where the ionization fraction of atomic hydrogen drops below 50%. We find that the simulated data are in a good correspondence with the analytical solutions and results of Iliev et al. (2009). Large errors for the run with resolution of 32 are caused by the relatively large size of the gas cells in comparison to the physical size of the shock front.

The next set of plots in Figure 4.9 show several gas properties in the box as a function of radial distance from the source at three different times: 100, 200 and 500 Myr. In the first column we plot mass fractions of neutral and ionised hydrogen. In the second, third and fourth rows we plot pressure, temperature and density, respectively. These results are also in good agreement with the results of Iliev et al. (2009). From all the plots we can see that the thickness of the shock decreases with increasing resolution. Grid cells for the two lowest resolutions, 32 and 64, are bigger than the physical size of the shock and therefore it is not well resolved. However, the size of the shock front settles on a constant value for the two highest resolutions.

4.3.3 Test 3: HII region expansion in a density gradient

The previous two tests assumed that the radiation is transferred in an environment with homogenous density. This is, however, not the case for the astrophysical processes that we want to study. Stars are usually formed in the centre of a collapsing gas cloud with a strong radial density gradient. Therefore, in this test we focus on the idealised case used also in Baczynski et al. (2015).

We place a source of radiation at the centre of a sphere with the density profile

$$n(r) = \begin{cases} n_{\rm c} & \text{if } r \leq r_{\rm c} \\ n_{\rm c}(r/r_{\rm c})^{-2} & \text{if } r > r_{\rm c}, \end{cases} \tag{4.15}$$

and let it evolve. We pick a central density of $n_c = 100\,{\rm cm}^{-3}$ and a core radius of $r_c = 1.97$ pc. For this choice of density profile it is possible to calculate an analytical solution (Franco et al., 1990; Whalen and Norman, 2005; Mellema et al., 2006) for the radius of the I-front as

$$R_{\rm grad}(t) = r_{\rm c}(1 + 2tn_{\rm c}\alpha_{\rm B})^{1/2}. \tag{4.16}$$

[8] Note that Iliev et al. (2009) used $L_{\rm box} = 30$ kpc.

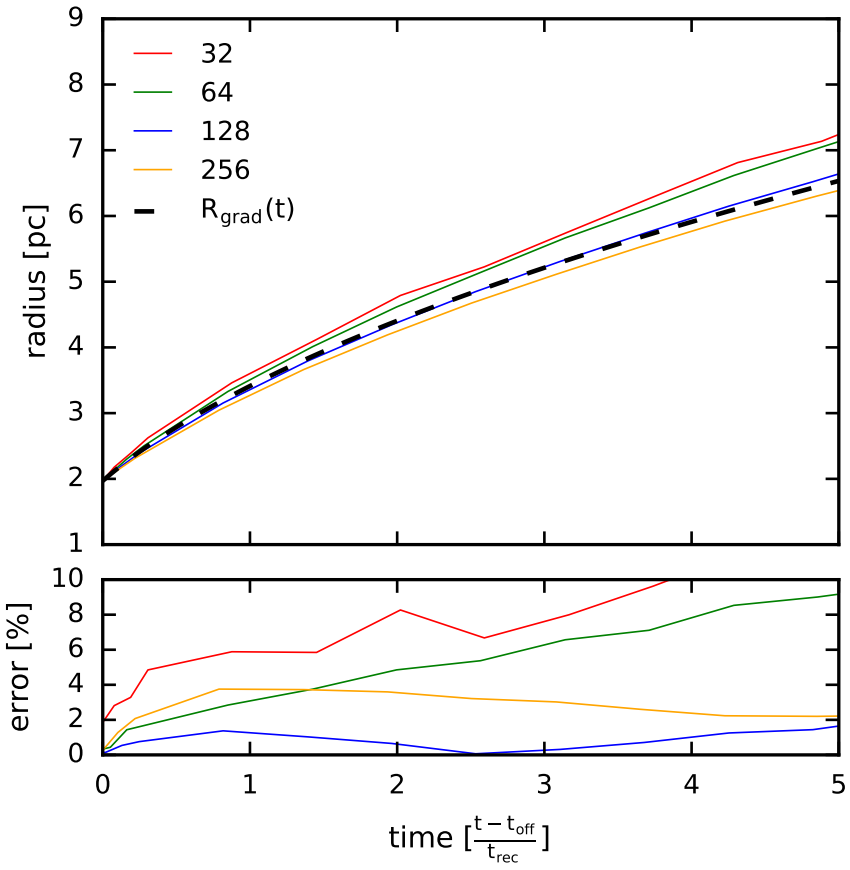

Figure 4.11: Results of Test 3: time evolution of the R-type I-front for resolutions 32, 64, 128 and 256 in gas with a radially decreasing density profile. The black dashed line is the analytical solution calculated for this test. The coloured lines are results of the simulations starting from t_{off} when the I-front reaches the core radius r_c. In the bottom panel we plot relative errors for each simulation compared to the analytical values.

We take $t = 0$ to be the time when the ionization front reaches the edge of the dense core, i.e. $R_{grad}(0) = r_c$.

In this test, we again set γ=1.0001 to prevent the density response due to gas heating. The ionization source produces $\dot{N}_\gamma = 1 \times 10^{49}$ photons per second. The recombination rate is fixed to a value of $\alpha_B = 2.59 \times 10^{-13}$cm^3 s^{-1} and the photoionization cross-section of the helium to $\sigma_H = 6.3 \times 10^{-18}$ cm^2.

Results of this test are shown in Figure 4.11. The duration of the simulation is approximately five times the recombination time ($5 \times t_{rec} \approx 6.73$ kyr) in the dense core.

We define the radius of the I-front as the distance from the source where the fraction of ionised hydrogen drops below 90% of the total mass of the gas in the corresponding spherical shell. From the plots we can see that the two lowest resolutions, 32 and 64, have the largest errors. The grid cells in these two simulations are not small enough to properly

resolve density gradients at large radii and therefore the shapes of their I-fronts are not entirely spherically symmetric. Instead, they depend on the mass inhomogeneities caused by the grid. Simulations with higher resolution give proper radially symmetric I-fronts that evolve according to expected values.

4.3.4 Test 4: Photo-evaporation of a dense clump by two sources

In this test we show how well our method resolves the formation of shadows behind dense objects. Our initial settings are similar to Baczynski et al. (2015) (see their Section 3.6). The difference is that here we use only a hydrogen ionising frequency bin. A box of size $L_{\rm box}$ = 32 pc is filled with neutral hydrogen gas with density n = 1 cm^{-3} and temperature 1000 K. In the middle of the box we placed a dense clump of gas with n = 1000 cm^{-3}, radius $r_{\rm clump}$ = 4 pc and temperature 10 K. The clump is irradiated by two sources located at positions $p_1(x,y,z)$ = (-14, 0, 0) pc and $p_2(x,y,z)$ = (0, -14, 0) pc. Each of these sources emits $\dot{N}_\gamma = 1.61 \times 10^{48}$ photons per second. The photoionization cross-section of hydrogen is fixed to $\sigma_{\rm H} = 5.38 \times 10^{-18}$ cm^2 and each photoionization heats the gas by 0.72 eV. The recombination rate is as usual fixed to value $\alpha_{\rm B} = 2.59 \times 10^{-13}$ cm^3 s^{-1}. The simulation runs until both ionization fronts pass around the dense clump (64 kyr) and form a shadow of non-ionised gas behind it.

In Figure 4.12 we present the results of the simulation with resolution[9] 128 at four different times: in the first column, the I-fronts are about to intersect. In the second column, the two regions of ionised gas are already joined and start ionising the dense clump. In the third column the clump is being heated and we see the formation of a shadow behind it. In the last column, the shadow is clearly visible. Its contours are not perfectly aligned with the white dashed lines because photons of our rays can experience small side-shifts that ionise the cells also within the shadow region. This artefact of the SIMPLEX method can be reduced by increasing the resolution.

The rows in Figure 4.12 correspond to different properties. The top row shows temperature, the middle row pressure and the two bottom rows illustrate the mass fraction of ionised hydrogen and its density. White dashed lines are added in order to indicate the edges of the shadow region behind the dense clump. Both from the pressure and temperature plot we can see that the part of the clump that faces the two sources is being heated and slowly evaporated, whereas parts in the shadow stay unaffected by the radiation.

4.3.5 Performance scaling with number of sources

A very common problem of ray-tracing radiative transfer simulations is that the required computation time increases linearly with the number of sources. However, this is not the case for the SIMPLEX method. Every cell in the grid can be considered as a source that radiates photons only to its neighbours. Therefore the main factor that influences the time required for a simulation is given by the resolution of the Voronoi grid and the maximum

[9] We show results for resolution 128, because our simulation with resolution 256 did not finish in a reasonable time. For highly ionised environments, as in this test, communication between processors appears to be slow. We plan to address this problem in future work.

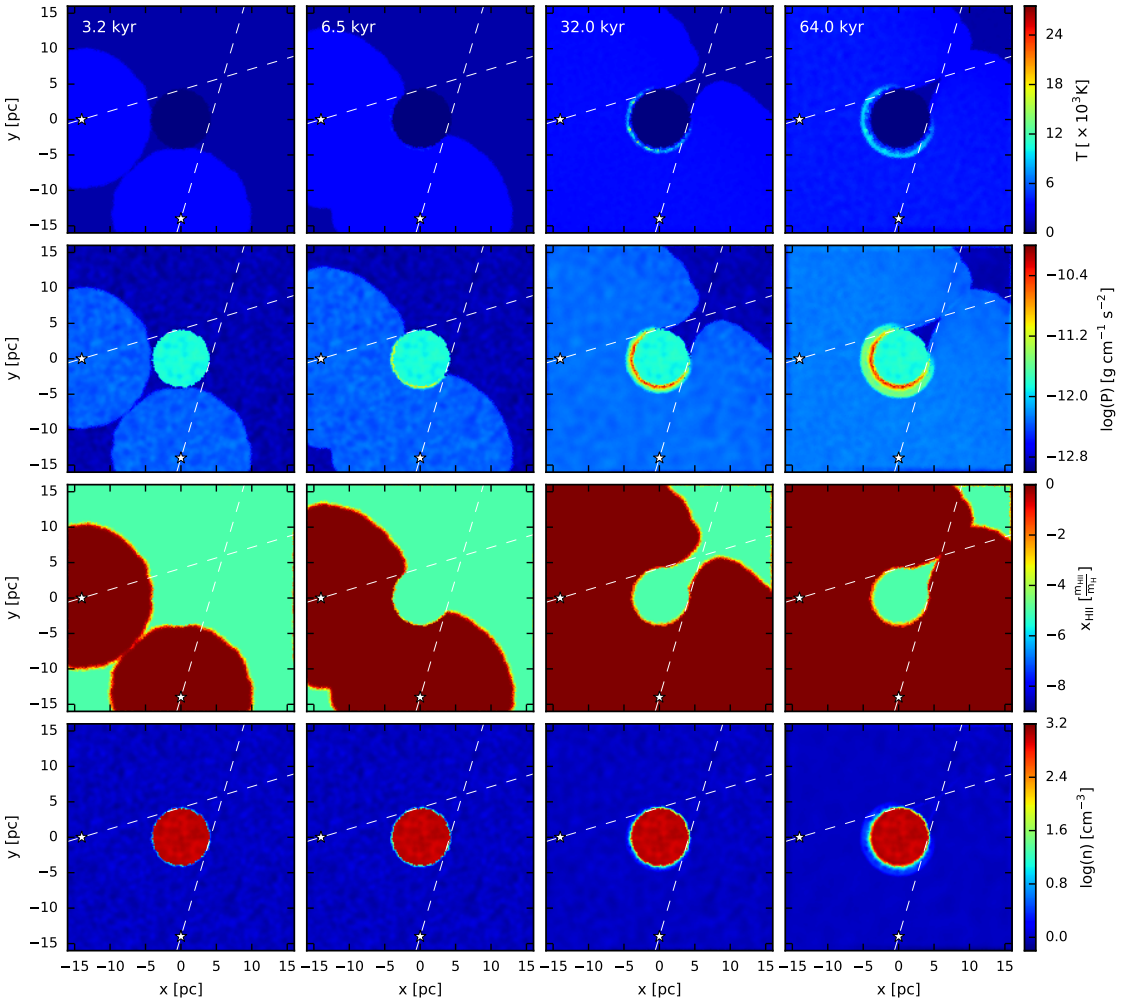

Figure 4.12: Results of Test 4: this figure shows the formation of the shadow behind a dense clump placed in the centre of the simulation box irradiated by two sources marked by stars. From left to right, the columns show $z = 0$ slices through the box at output times 3.2, 6.5, 32 and 64 kyr, respectively. From the top to the bottom, the rows show gas temperature, pressure, the mass fraction of the ionised gas and the total density of the gas, respectively. Dashed white lines are added to show the boundaries of the expected shadow behind the clump.

Resolution		32	64	128	256
Number of procesors		16	32	160	320
Run time [seconds]	1 source	2311	10265	36433	268938
	10 sources	2525	13042	51925	411294
	100 sources	2741	14492	58529	462979

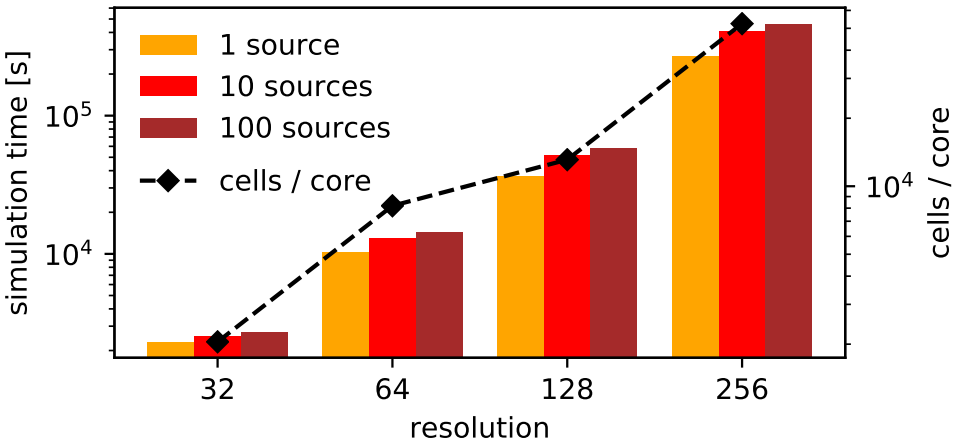

Figure 4.13: Dependance of the simulation time (in seconds) on the number of sources and the resolution. For simulations with resolutions 32, 64, 128 and 256, we used 16, 32, 160 and 320 cores, respectively. Times are calculated from time balance reports produced by the AREPO code.

number of steps in the radiative transfer phase, which in turn is determined by the maximum number of cells photons can travel within the box.

In order to show this advantage we performed a set of simulations of R-type I-fronts where we used 1, 10 and 100 sources, each with ionization rate 10^{49}, 10^{48} and 10^{47} photons per second, respectively, so that in all three simulations the total production rate of ionising photons was the same. The setup of the simulation box is identical to Test 1. In simulations with 10 and 100 sources, we placed sources evenly on a spherical shell of radius $r \approx 700$ pc around the original position of the single source.

The total running times of simulations in seconds are summarised in Figure 4.13. From the results we can observe an increase of the time for larger source numbers. This time increase is, however, mainly related to the part of the code that searches gas cells near source locations and injects new photons into them, and the functional increase is small compared to the increase in the number of sources.

It is important to note that just as with other ray tracing algorithms, in SIMPLEX the computation time increases in regions with low radiation opacity. The time increase is caused by copying unattenuated photons from cell to cell. For example in Test 4, one can observe an sudden increase of the computational time when the two Strömgren spheres meet each other, since at this point photons from the first source have to travel through the ionised region of the second source until they reach the ionization front on the other side, and vice versa.

4.4 Summary

In this chapter, we introduced a new implementation of the SIMPLEX radiation transfer algorithm on the moving mesh of the hydrodynamical code AREPO. We refer to our combination of SIMPLEX and AREPO as SPRAI: SIMPLEX Photon Radiation in the AREPO Implementation. We show the results when SPRAI is applied to several simple test problems that have analytical solutions: the expansion of an HII region in homogeneous gas in both the R-type and D-type regimes, and the expansion of an HII region in gas with a radially decreasing density profile. All our tests produce results that are in good agreement with the analytical solutions and with the results of the ray-tracing code FERVENT, which uses the same chemistry module. In our last test, we irradiated a dense blob of gas with two identical sources and observed the formation of shadow behind it. This simulation is also in a good agreement with the results presented in Baczynski et al. (2015).

One of the main problems of this implementation is variation of the width of photon rays with different resolutions. This behaviour was already observed and described in the original SIMPLEX papers. In Section 4.2.4, we show that for higher resolution simulations this has an important impact on the homogeneity of the calculated ionization rates. Our solution to this problem is to construct the ionization field from randomly rotated partial fields. This method proved to be satisfactory for our testing problems, although it introduces additional demands on the computational time.

In the following Chapter 5, we will optimize the performance of the code and do some multifrequency tests that we did not include here. We will also discuss cases with the high

recombination rates and effects of radiation pressure. Nevertheless, our primary goal is to use this code for real astronomical problems, including simulations of the formation and fragmentation of accretion disks around Pop-III stars in the early universe. We will study this further in Chapter 6.

5 SPRAI-II: Extended version of the method

This chapter is based on the second paper from the SPRAI series that was submitted in October 2019 to the Monthly Notices of the Royal Astronomical Society. It is expected to be published after the submission of this thesis, and I am the first author. I did parts regarding multi-frequency treatment, radiation pressure, as well as all test simulations. M.Magg helped with the implementation of the recombination correction. S.C.O.Glover and R.S.Klessen did further text editing and proofreading.

This chapter extends on the previous chapter and describes further improvements of the SPRAI method. First, we introduce our modifications that were essential for the correct physical behavior of our method in simulations with various gas densities. We discuss here extension to the radiation model presented in the previous chapter: multi-frequency treatment of the radiation and radiation pressure, and include corresponding test cases.

5.1 Introduction

In the previous Chapter 4 which is based on Jaura et al. (2018), we introduced SPRAI (SIMPLEX Photon Radiation in the AREPO Implementation), an implementation of the SIMPLEX radiation transfer algorithm (Kruip et al., 2010; Paardekooper et al., 2010) in the AREPO moving-mesh code (Springel, 2010). As implemented in SPRAI, the SIMPLEX algorithm is essentially a variant of the short characteristics method designed for use on unstructured meshes, such as the Voronoi mesh used in AREPO. We demonstrated in Jaura et al. (2018) that the computational cost of SPRAI is almost independent of the number of sources of radiation, and that the non-spherical artifacts in the radiation distribution common to short characteristics methods can be almost entirely mitigated by randomly rotating the set of directional bins multiple times per radiation transport run and integrating the resulting fields. We also showed that SPRAI does an excellent job of modelling the time evolution of R-type ionisation fronts (I-fronts) and a good job of modelling the shadows cast by overdensities in the gas distribution. Together, these features make SPRAI a highly promising technique for modelling radiation transport on-the-fly in hydrodynamical simulations carried out with AREPO.

However, although the basic version of SPRAI (SPRAI-I) (Jaura et al., 2018) introduced in Chapter 4 does an excellent job of modelling R-type I-fronts, it is not well-suited for modelling D-type I-fronts, for reasons we explore in this chapter. This limits its usefulness for modelling the early evolution of HII regions around massive stars. In this chapter, we present an extended version of SPRAI (SPRAI-II) (Jaura et al., 2020) that addresses this weakness. In addition to the modifications required to enable the code to properly treat the evolution of D-type I-fronts, this updated version of SPRAI additionally includes a revised multi-frequency treatment that allows the code to model helium photoionisation. Moreover, SPRAI-II also now accounts for the effects of radiation pressure. In the remainder of the

chapter, we describe the modifications we have made to SPRAI to add this new functionality, and also present the results from a series of tests of the code.

The structure of this chapter is as follows. In Section 5.2, we first briefly summarize the basics of how SPRAI works, and then describe the new features that we have added to the code. In Section 5.3, we show how SPRAI-II performs well on several test problems chosen to highlight the new features in the code. Finally, we conclude in Section 5.4 with a summary of our results and a brief overview of the applications for which we plan to use SPRAI in the future.

5.2 Code modifications

In this section, we discuss the changes we have made in SPRAI-II. These address three main aspects of the code. Firstly, there is a set of changes that we have made in order to properly treat the behaviour of I-fronts in high density gas in a computationally efficient fashion (Section 5.2.2). Second, we have extended the code to treat the effects of H_2 photodissociation and helium photoionization, as described in Section 5.2.3. Finally, we have also added an option to the code that allows us to compute the radiation pressure exerted on the gas by the absorbed radiation (Section 5.2.4).

However, before discussing any of these changes, it is useful to remind the reader of a few basic details regarding the operation of SPRAI (Section 5.2.1). For brevity, we do not attempt to discuss every single feature of SPRAI, since this material is covered at some length in SPRAI-I. Instead, we focus on a few aspects that are particularly important for understanding the changes we have made to the code.

5.2.1 How SPRAI works

As we describe at greater length in Section 4.2 of SPRAI-I, the code computes the effects of radiation from an arbitrary set of sources on the surrounding gas using a two step process. The whole process is schematically depicted in Figure 5.1. The first step is the radiative transport (RT) step, during which photons are created by the sources and propagated from cell to cell on the Voronoi mesh. For technical reasons, this step is carried out once per full hydrodynamical timestep[1]. If the length of the full hydrodynamical timestep is $t_{\rm HD}$, then the number of photons created by each source in each of the photon energy bins tracked by SPRAI is simply the photon emission rate for that source and that energy bin multiplied by time $t_{\rm HD}$.

The photons created by each source are assigned to the Voronoi cell containing the source and distributed uniformly amongst a set of directional bins. Photons are then propagated from cell to cell using a directional transport algorithm that ensures that they always move in a direction that is approximately the same as the one defined by their directional bin

[1] AREPO uses a hierarchical time-stepping scheme, so on any given timestep only a subset of the Voronoi cells may be active. However, the nature of the time-stepping scheme ensures that periodically every cell will be synchronised and active on the same timestep. We term timesteps on which this is the case *full hydrodynamical timesteps*. Intervening timesteps on which only a subset of cells are active are termed *hydrodynamical sub-steps*.

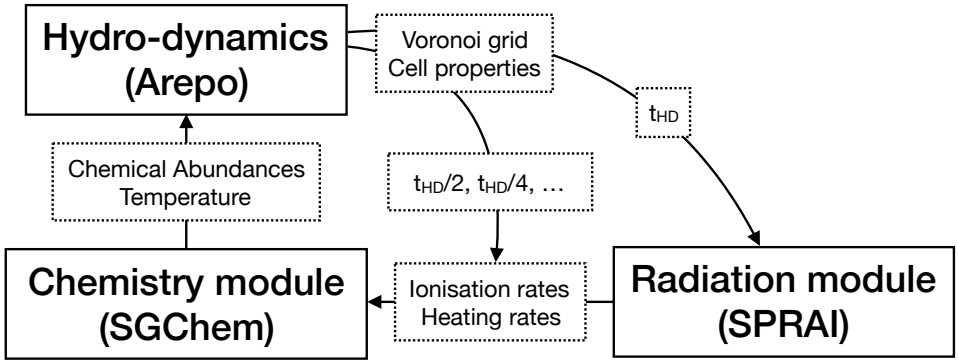

Figure 5.1: A schematic description of the SPRAI implementation. The length of a full hydrodynamical time-step is denoted as $t_{\rm HD}$, while sub-steps are denoted as power-of-two fractions of $t_{\rm HD}$.

(see Section 4.2.1 for more details). Whenever the photons enter a new cell, the number of photons absorbed in that cell during the period $t_{\rm HD}$ is calculated, using the current chemical and thermal state of the cell. Absorbed photons are removed from the calculation and are not propagated further. This procedure is then repeated until all photons have been attenuated or have escaped from the simulation volume.

At the end of this phase of the calculation, we therefore know the number of photons in each energy bin that have been absorbed in each cell in the Voronoi mesh during a time $t_{\rm HD}$. These numbers are then used to derive photoionization, photodissociation and radiative heating rates for each cell.[2] These rates are then passed as input to the second step of the calculation. This step is the chemical update, which is carried out by the primordial SGCHEM in AREPO. SGCHEM is a module designed to follow the non-equilibrium chemical evolution of the gas in an AREPO calculation in a variety of different simulations, ranging from present-day GMCs (e.g. Clark et al., 2019) to high-redshift minihaloes (e.g. Schauer et al., 2019). In the test calculations presented here and in SPRAI-I, we use a primordial chemistry network implemented as part of SGCHEM and described in Schauer et al. (2019) and other references therein, but in principle SPRAI can also be used with other chemical networks. The chemical evolution of the gas in a cell is followed on every hydrodynamical sub-step for which the cell is active, with the photochemical rates assumed to remain constant from sub-step to sub-step throughout the full hydrodynamical timestep $t_{\rm HD}$.

[2]Technically, these should be considered to be the time-averaged values of the various rates over the time period $t_{\rm HD}$.

5.2.2 Recombination correction at high densities

In SPRAI-I, the number of photons in energy bin γ removed by absorption in a given Voronoi cell is

$$\mathcal{N}^{\gamma} = \mathcal{N}^{\gamma}_{\rm in}\left(1 - e^{-\tau^{\gamma}}\right), \tag{5.1}$$

where $\mathcal{N}^{\gamma}_{\rm in}$ is the number of photons in the energy bin entering the cell during a time $t_{\rm HD}$ and τ^{γ} is the mean optical depth of the cell in energy bin γ. The latter is given by

$$\tau^{\gamma} = {\rm d}N \sum_{\rm X} \langle \sigma^{\gamma}_{\rm X} \rangle x_{\rm X}, \tag{5.2}$$

where dN is the column density of H nuclei in the cell, $x_{\rm X}$ is the fractional abundance of absorber X relative to the number of H nuclei, and $\langle \sigma^{\gamma}_{\rm X} \rangle$ is the frequency-averaged absorption cross-section for species X in energy bin γ. The sum is carried out over all chemical species likely to absorb photons from this energy bin (e.g. for an energy bin $13.6 < E < 15.2\,{\rm eV}$, we need only consider absorption by atomic hydrogen or by bound-bound electronic transitions in molecular hydrogen), since photons of this energy cannot photoionize H_2 or He).

Absorbed photons are allocated amongst the various different species according to the ratio

$$f_{\rm X} = \frac{\langle \sigma^{\gamma}_{\rm X} \rangle x_{\rm X}}{\Sigma^{\gamma}}, \tag{5.3}$$

where $\Sigma^{\gamma} = \sum_{\rm X} \langle \sigma^{\gamma}_{\rm X} \rangle x_{\rm X}$, so the total number of photons from energy bin γ allocated to species X during a time $t_{\rm HD}$ is $f_{\rm X}\mathcal{N}^{\gamma} \equiv \mathcal{N}^{\gamma}_{\rm X}$. If this number is greater than the total number of atoms/molecules of species X present in the cell, $\mathcal{N}_{\rm X}$, then the total number of photons absorbed is limited to this number, i.e.

$$\mathcal{N}^{\gamma}_{\rm X} = \begin{cases} \mathcal{N}^{\gamma}_{\rm X} & \text{if } \mathcal{N}^{\gamma}_{\rm X} < \mathcal{N}_{\rm X} \\ \mathcal{N}_{\rm X} & \text{otherwise.} \end{cases} \tag{5.4}$$

This last check was introduced in SPRAI-I in an attempt to ensure that the method was photon-conserving, i.e. that absorption in the cell did not remove more photons than were accounted for by ionization/photodissociation events in the chemistry. However, there is an unstated assumption here, which is that each atom/molecule in the cell can only be ionized/dissociated once during the timestep $t_{\rm HD}$. This assumption is valid when the number of recombinations $N_{\rm rec}$ occurring within the cell during the period $t_{\rm HD}$, is much smaller than the number of neutral hydrogen and helium atoms[3] in the cell, $N_{\rm nuc}$, as in this case the average number of photons absorbed per neutral nucleon will indeed be close to one. However, if our assumption that $N_{\rm rec} \ll N_{\rm nuc}$ is violated, as will generally be the case if the recombination time of the ionized gas, $t_{\rm rec}$, is shorter than $t_{\rm HD}$, then Equation 5.4 is no longer valid.

[3] In the case of H_2 photodissociation, we can make a similar argument regarding the number of H_2 molecules formed in the cell versus the number of molecules present initially, but to keep our explanation simple we focus here purely on the atoms.

We have addressed this issue in SPRAI-II by changing the way in which we calculate the upper limit on the number of photons that can be absorbed by a particular species in a given cell during a single timestep. Our new approach consists of the following three steps:

1. When initializing a cell for the radiation transport, we compute a recombination factor $f_{\rm rec}$ for hydrogen and helium which is the ratio of the current time-step Δt to the recombination time-scale $t_{\rm rec}$:

$$f_{\rm rec} = \frac{\Delta t}{t_{\rm rec}} = \Delta t \, n \, \alpha_{B,X}, \tag{5.5}$$

where n is the nucleon number density. X stands for the element the correction is applied to, i.e., helium or hydrogen, and $\alpha_{B,X}$ is the corresponding case-B recombination coefficient. Using the nucleon number density in Equation 5.5 in general gives an upper limit on how many photons can be absorbed, but becomes exact if the cell is fully ionized during the timestep. The values we use for the case-B recombination coefficients are taken from Glover and Jappsen (2007), and are based on Ferland et al. (1992) for hydrogen and Hummer and Storey (1998) for helium:

$$\begin{aligned}\alpha_{B,\rm H} = 2.753 \times 10^{-14} \, {\rm cm^3 \, s^{-1}} \left(\frac{315614}{T} \right)^{\frac{3}{2}} \\ \times \left(1 + \left[\frac{115188}{T} \right]^{0.407} \right)^{-2.242},\end{aligned} \tag{5.6}$$

$$\begin{aligned}\alpha_{B,\rm He} = 10^{-11} \, {\rm cm^3 \, s^{-1}} T^{-\frac{1}{2}} \left[11.19 - 1.676 \log_{10}(T) \right. \\ - 0.2852 \log_{10}(T)^2 \\ \left. + 0.04433 \log_{10}(T)^3 \right],\end{aligned} \tag{5.7}$$

where T is the temperature in Kelvin. When exposed to ionizing radiation, the cells heat up quickly, and so using the temperature at the start of the timestep can be inaccurate if this is particularly low. We therefore adopt a temperature floor of 6000 K in the computation of the recombination rate coefficients, using this value if $T_{\rm gas} < 6000$ K and otherwise using the actual temperature in the cell.

2. Each time a photon package hits a gas cell, the number of photons that are absorbed, $\mathcal{N}_{\rm X}^{\gamma}$, is limited to the number of atoms that can be ionized. To allow the absorption of more photons for regions with large recombination rates (i.e. $f_{\rm rec} > 1$) we define a new quantity $N'_{\rm X}$:

$$\mathcal{N}'_{\rm X} = \mathcal{N}_{\rm X} + \mathcal{N}_{\rm nuc,X} f_{\rm rec}, \tag{5.8}$$

where $\mathcal{N}_{\rm nuc,X}$ is the total number of nuclei of atom X in the cell. We then replace Equation 5.4 with

$$\mathcal{N}_{\rm X}^{\gamma} = \begin{cases} \mathcal{N}_{\rm X}^{\gamma} & \text{if } \mathcal{N}_{\rm X}^{\gamma} < \mathcal{N}'_{\rm X} \\ \mathcal{N}'_{\rm X} & \text{otherwise.} \end{cases} \tag{5.9}$$

We note that this modification is used only when computing the number of photons absorbed in the cell, not when computing the optical depth of the cell (Equation 5.2), for which we continue to use the unmodified column density.

3. If additional photon packages pass through the same cell during the same radiation transfer step, it is necessary to account for the fact that the cell has already absorbed some photons, meaning that it has less capability to absorb any further photons. We do this by reducing $f_{\rm rec}$ each time a cell absorbs photons during the radiation transfer step:

$$f_{\rm rec,new} = f_{\rm rec}\left(1 - \frac{N_{\rm X}^{\gamma}}{N_{\rm X}'}\right). \tag{5.10}$$

We also modify the optical depth of the cell by reducing the value of $x_{\rm X}$ by the same factor:

$$x_{\rm X,new} = x_{\rm X}\left(1 - \frac{N_{\rm X}^{\gamma}}{N_{\rm X}'}\right). \tag{5.11}$$

Note that we use this modified version of $x_{\rm X}$ only when computing the optical depth seen by additional photon packages passing through the cell. For updating the actual chemical state of the cell during the chemistry step, we continue to rely on the SGCHEM module as before.

These changes ensure that the number of photons in energy bin γ absorbed in the cell by species X during the radiation transport step cannot exceed $\mathcal{N}_{\rm X}'$. However, with these changes alone, we found that SPRAI did not always converge to the expected behaviour in the optically thin limit. This error is related to the photoionization rates being normalized to the abundance of neutral atoms. Our way of approximately accounting for the recombinations can lead to us slightly overestimating the number of atoms available through recombinations. For cells with very few remaining neutral atoms, such mis-estimates can have a large impact on the normalization factor and thus on the normalized ionization rates, resulting in these rates becoming larger in some cases than their values in the optically thin limit. To correct for this, we limit the photoionization rates to be no larger than their optically thin values. In other words, for a package of $\mathcal{N}^{\gamma}$ photons in energy bin γ, the rate at which they ionize species X is limited to be no larger than

$$R_{\rm ion} = \frac{\mathcal{N}^{\gamma}\langle\sigma_{\rm X}^{\gamma}\rangle {\rm d}r}{V t_{\rm HD}}, \tag{5.12}$$

where dr is the approximate size of the cell and V is its volume.

5.2.3 Improved multifrequency treatment

In order to properly treat several different ionization processes in the ISM one needs to divide the photon spectrum into several energy bins. In SPRAI-I, we were interested primarily in

Bin (eV)	H_2^{dis}	H^{ion}	H_2^{ion}	He^{ion}	RP
11.2 - 13.6	✓	-	-	-	-
13.6 - 15.2	✓	✓	-	-	✓
15.2 - 24.6	-	✓	✓	-	✓
24.6+	-	✓	✓	✓	✓

Table 5.1: List of energy bins and the processes for which they are responsible. 'RP' represents radiation pressure, discussed in Section 5.2.4 below.

two processes, the photoionization of atomic and molecular hydrogen:

$$H + \gamma \rightarrow H + e^-, \tag{5.13}$$

$$H_2 + \gamma \rightarrow H_2^+ + e^-. \tag{5.14}$$

We therefore dealt with photons in two different energy bins: photons with energies $13.6 < E < 15.2$ eV, which can ionize atomic hydrogen but not molecular hydrogen, and photons with energies $E > 15.2$ eV, which can ionize both atomic and molecular hydrogen. We denoted the first bin as the 13.6+ bin and the second as the 15.2+ bin.

However, this simplified treatment of the photochemistry neglects two additional processes that are important in the early Universe: the photodissociation of H_2 and the photoionization of helium:

$$H_2 + \gamma \rightarrow H + H, \tag{5.15}$$

$$He + \gamma \rightarrow He^+ + e^-. \tag{5.16}$$

To treat these additional processes, it is necessary to include two additional energy bins. Photons with energies in the range $11.2 < E < 13.6$ eV – often known as Lyman-Werner (LW) photons – can photodissociate H_2 but cannot photoionize H, H_2 or He. We track these photons in the 11.2+ bin. Photons with energies $E > 24.6$ eV can photoionize He as well as H and H_2. We have therefore introduced a 24.6+ bin to track these photons and have consequently changed the definition of the 15.2+ bin to include only those photons with energies $15.2 < E < 24.6$ eV. We continue to neglect the photoionization of He^+ to He^{++} as this is unimportant for most stellar sources, other than very massive Pop-III stars.

In Table 5.1, we summarize the set of energy bins included in SPRAI-II and the processes that the photons in each bin are responsible for. Note that we account for the photodissociation of H_2 by photons in the 13.6+ bin, even though most of these photons will instead be absorbed by atomic hydrogen if any is present. However, we assume that photons in the 15.2+ and 24.6+ bins photoionize H_2 in preference to photodissociating it.

In order to include H_2 photodissociation in SPRAI, it is necessary to determine an appropriate frequency-averaged cross-section for this process. This is not straightforward, as H_2 photodissociation is a two-stage process driven by line absorption rather than continuum absorption. For simplicity, in our present treatment we follow Baczynski et al. (2015) and adopt a frequency-independent cross-section of $\sigma_{H_2,dis} = 2.47 \times 10^{-18}$ cm^2 for this process. This value is derived by taking the ratio of the photodissociation rate D to the LW photon

flux F in the optically thin limit, i.e. $\sigma_{\rm H_2,dis} = D/F$. We use values for D and F computed for the Draine (1978) parameterization of the interstellar radiation field, but the ratio of D to F varies only weakly as we change the spectral shape, so the resulting value of $\sigma_{\rm H_2,dis}$ should also be reasonably representative of what we would expect for gas illuminated by Pop-III or metal-poor Pop-II stars. Unlike Baczynski et al. (2015), we do not currently account for the fact that the effective H_2 photodissociation cross-section decreases as the column density of H_2 between the gas and the radiation source increases owing to the effects of H_2 self-shielding. This effect is much harder to include in SPRAI than in a conventional ray-tracing code, as there is no simple way in which to compute the required H_2 column densities. By omitting it, we under-estimate the attenuation of the H_2 photodissociation rate at low H_2 column densities and over-estimate it at high H_2 column densities. However, this is only important in situations where the photodissociation region – which is often very narrow – is actually resolved in the simulation, and so there are many scenarios in which our approximate treatment is useful. Nevertheless, this remains a weakness of the SPRAI-II, and we intend to address it in future work.

We also account in our treatment of H_2 photochemistry for the heating produced by ultraviolet (UV) pumping of vibrationally-excited levels of H_2. This effect results from the fact that only $\sim$ 15% of the Lyman-Werner photons absorbed by H_2 actually result in photodissociation. The rest of the time, the electronically excited H_2 molecule instead radiatively de-excites to a bound ro-vibrational level in the electronic ground state. Most of the time, the level populated by this process has $v > 0$, and so this results in the production of a population of vibrationally-excited H_2 molecules. At low density, the energy associated with this vibrational excitation is eventually radiated away, but in dense gas it is instead converted to heat by collisions. We model this process using the same approach as in Baczynski et al. (2015): we adopt a UV pumping rate that is a factor of 6.94 times larger than the photodissociation rate (Draine and Bertoldi, 1996) and hence adopt a total photon absorption cross-section for H_2 that accounts for both dissociation and UV pumping and that has a magnitude $\sigma_{\rm H_2,tot} = 7.94\sigma_{\rm H_2,dis}$. The mean energy that is converted to heat per UV pumping event is calculated using the density-dependent prescription given in Appendix A of Burton et al. (1990).

Finally, in addition to the processes listed in Table 5.1, we also account for the absorption of photons in the 11.2+ energy bin by the Lyman series lines of atomic hydrogen. Although usually unimportant, this effect can become very important when the atomic hydrogen column density of the gas becomes very large (see e.g. Wolcott-Green and Haiman, 2011; Schauer et al., 2017a; Glover, 2017). We assume that photons absorbed by the Lyman β, γ, etc. lines (all of which fall within the 11.2+ bin) are converted to some mix of Lyman-α photons and lower energy photons. This process therefore removes H_2 photodissociating photons without a resulting chemical change in the gas. We account for this process using an effective absorption cross-section of $\sigma_{\rm Lyman} = 5.23 \times 10^{-25}$ cm^2, derived from the work of Wolcott-Green and Haiman (2011).

5.2.4 Radiation pressure

The final major change that we have made in SPRAI-II is the inclusion of a treatment of the effects of radiation pressure. Whenever a photon of energy E is absorbed in the gas, the gas gains a corresponding momentum E/c and the resulting force exerted on the gas can play a significant role in its dynamical evolution (see e.g. Haehnelt, 1995; Wise et al., 2012b; Rahner et al., 2017, for some examples of situations in which radiation pressure is dynamically important).

Our treatment of radiation pressure is relatively simple. For every absorbed photon, we calculate the amount of momentum it deposits. To do this, we need to know the energy and the direction of the photon. For the purposes of the radiation pressure calculation, we assume that every photon absorbed in a particular type of photochemical reaction R has an energy equal to

$$E = E_{\mathrm{th,R}} + \langle E_{\mathrm{R}} \rangle, \tag{5.17}$$

where $E_{\mathrm{th,R}}$ is the threshold energy for that reaction (13.6 eV for H ionization, 15.2 eV for H_2 ionization etc.) and $\langle E_{\mathrm{R}} \rangle$ is the mean excess energy deposited as heat in the gas by that particular reaction. The latter quantity depends on the spectrum of the source and is computed using the expression

$$\langle E_{\mathrm{R}} \rangle = N^{-1} \int_{E_{\mathrm{th,R}}}^{\infty} F_{\nu} \sigma_{\nu,\mathrm{R}} \left(1 - \frac{E_{\mathrm{th,R}}}{h\nu} \right) \mathrm{d}\nu \tag{5.18}$$

where

$$N = \int_{E_{\mathrm{th,R}}}^{\infty} \frac{F_{\nu} \sigma_{\nu,\mathrm{R}}}{h\nu} \mathrm{d}\nu, \tag{5.19}$$

and where F_{ν} is the radiative flux from the source and $\sigma_{\nu,\mathrm{R}}$ is the frequency-dependent cross-section for reaction R. Note that although Equation 5.17 is an approximation, it is a very good one whenever the number of photons absorbed in the cell is large, which is almost always the case. Finally, given the energy E of the photon, and the unit vector $\vec{n}$ describing its direction, the momentum it contributes to the gas follows as

$$\vec{p} = \frac{E}{c} \vec{n}. \tag{5.20}$$

During the radiation transfer step, we compute the total momentum deposited in each cell by summing the individual vector contributions from each photon. At the end of the radiation transfer step, we update the momentum of the gas in the cell to account for the accumulated photon momentum. We then use the updated gas momentum to update any other quantities in AREPO that depend on the momentum, such as the gas velocity and the total energy.

The accuracy with which this simple method captures the radiation pressure distribution around a single source depends on the hydrodynamical resolution. In situations where we resolve the Strömgren sphere around the source with a large number of cells, we do a good

job of capturing the correct angular dependence of the radiation pressure, as the tests in Section 5.3.3 demonstrate. However, the error we make increases as the number of cells in the ionized region decreases, and in the limit where the Strömgren radius becomes smaller than the cell size, our treatment breaks down as in this case the vector sum of the momentum injected by an isotropic radiation source is zero. To deal with this situation, it is necessary to modify the calculation of the momentum flux between grid cells, as outlined in Hopkins and Grudic (2019). This requires some deep-seated changes to the operation of the AREPO hydrodynamic solver that are out of the scope of our current study, and so for the time being we merely mention this as a caveat in the applicability of our radiation pressure treatment. However, as a preliminary measure to avoid the loss of the momentum within the source cell, we compute the momentum deposited by photons in each directional bin in the source cell and redistribute this instead to the neighbouring cells.

An additional caveat is that our current treatment of radiation pressure only accounts for the so-called direct radiation pressure due to photons emitted by individual luminous sources. We do not account for the indirect radiation pressure resulting from e.g. the scattering of Lyman-α photons owing to the computational complexity involved in modelling this correctly (see e.g. Smith et al., 2018, and references therein).

5.3 Test results

In the previous section, we described the technical changes introduced in SPRAI-II. Here, we present a set of tests to show how our code performs for several problems of interest.

5.3.1 Tests of the recombination correction

In order to test the recombination correction described in Section 5.2.2 it is necessary to carry out simulations in a regime in which we expect it to be important, i.e. a regime where $t_{\rm rec} \ll t_{\rm HD}$. This is most easily achieved by simulating the growth of an HII region in dense gas. We have therefore carried out a series of tests similar to the ones described in the STARBENCH code comparison project (STARBENCH) (Bisbas et al., 2015). In particular, we are interested in how well the code captures both the early and the late phase of the D-type expansion of the ionization front.

5.3.1.1 Early phase expansion

The initial conditions for this test consist of a simulation box with a size $L_{\rm box} = 4$ pc filled with a gas of pure hydrogen with a uniform initial temperature $T_0 = 100$ K and density $\rho_0 = 5.21 \times 10^{-21}\,{\rm g\,cm^{-3}}$. A source emitting $\dot{N}_{\rm ion} = 10^{49}$ photons per second in the 13.6+ energy bin and no photons in any other bin is placed at the center of the box. The spectrum of the source is that of a T=10^5 K black body, and so in the optically thin limit, each photoionization deposits a mean energy of 0.756 eV in the gas. Following Bisbas et al. (2015), we fix the value of the recombination coefficient at $\alpha_{\rm B} = 2.59 \times 10^{-13}$ cm^3 s^{-1} – the case-B value appropriate for a gas with temperature $T = 10^4$ K – rather than using the temperature-dependent value given by Equation 5.6. However, unlike in Bisbas et al. (2015),

Setup	$\Delta t_{\rm RT}$ (Myr)	Rec. Corr.	$X_{\rm H+}$	T (K)	R (pc)
wo_p1	3.768e-04	✗	0.50	7247	1.16
wo_0	3.768e-05	✗	0.88	7969	0.99
wo_m1	3.768e-06	✗	0.99	8568	0.96
w_p1	3.768e-04	✓	1.00	8749	0.94

Table 5.2: Simulation settings of the recombination test. The third column indicates whether or not the run was carried out using the recombination correction described in Section 5.2.2. The fourth and fifth columns list the mass-averaged values of the ionization fraction $X_{\rm H+}$ and temperature T within the central 0.5 pc of the Strömgren sphere at time of 80.4 kyr. The last column shows the radius R of the Strömgren sphere at the same time.

we do not fix the temperature of the ionized gas itself to 10^4 K, but instead solve for its actual temperature as a function of time using the SGCHEM module. We allow the simulation to evolve for a total of 141 kyr before terminating it.

$$M_{\rm target} = 1.53 \times 10^{-3} {\rm M}_\odot \left(\frac{n}{10^4 \, {\rm cm}^{-3}} \right)^{-1}, \tag{5.21}$$

where n is the nucleon number density. This value was chosen to ensure that the gas in the initial Strömgren volume is resolved by at least a few hundred cells regardless of the initial gas density provided that the flux of ionizing photons from the source exceeds $\dot{N}_{\rm ion} = 10^{48}$ s^{-1}, a requirement that is satisfied in all of the test problems presented in this chapter. We note that this Strömgren refinement criterion scales more steeply with density than the commonly used Jeans refinement (Truelove et al., 1997), which scales as $M_{\rm Jeans} \propto 1/\sqrt{n}$. This steeper scaling implies that at high enough densities Jeans refinement is always insufficient for resolving ionizing radiation feedback.

We set up four different simulations. Three of these are carried out without the modifications described in Section 5.2.2 while the fourth one includes our new changes. The radiation time-step $\Delta t_{\rm RT}$ in the first case *wo_p1* is an order of magnitude higher than the recombination time $t_{\rm rec}$. In the second simulation, *wo_0*, the two times are of the same order of magnitude. In the third simulation, *wo_m1*, $\Delta t_{\rm RT}$ is an order of magnitude lower than $t_{\rm rec}$. Finally, in the last simulation, *w_p1*, we use the same settings as in *wo_p1* but with the recombination correction switched on. The different settings are summarized in Table 5.2.

In the top panel of Figure 5.2, we show how the radius of the ionization front[4] (I-front) varies as a function of time in the four different simulations. In this Figure, we focus on the expansion of the I-front at early times ($t < 140$ kyr). The time resolution of our output dumps is too coarse to capture the extremely short initial phase of R-type expansion, which lasts for a period of the order of a single recombination time, but allows us to follow the later D-type expansion of the front. We see immediately from Figure 5.2 that the behavior of the I-front in run *wo_p1* is significantly different from its behavior in the other runs. If $\Delta t_{\rm RT} > t_{\rm rec}$ and we

[4]For the purposes of this test, we defined the radius of the ionization front to be the radial distance from the source at which the spherically-averaged mass fraction of ionized hydrogen first drops below 10%.

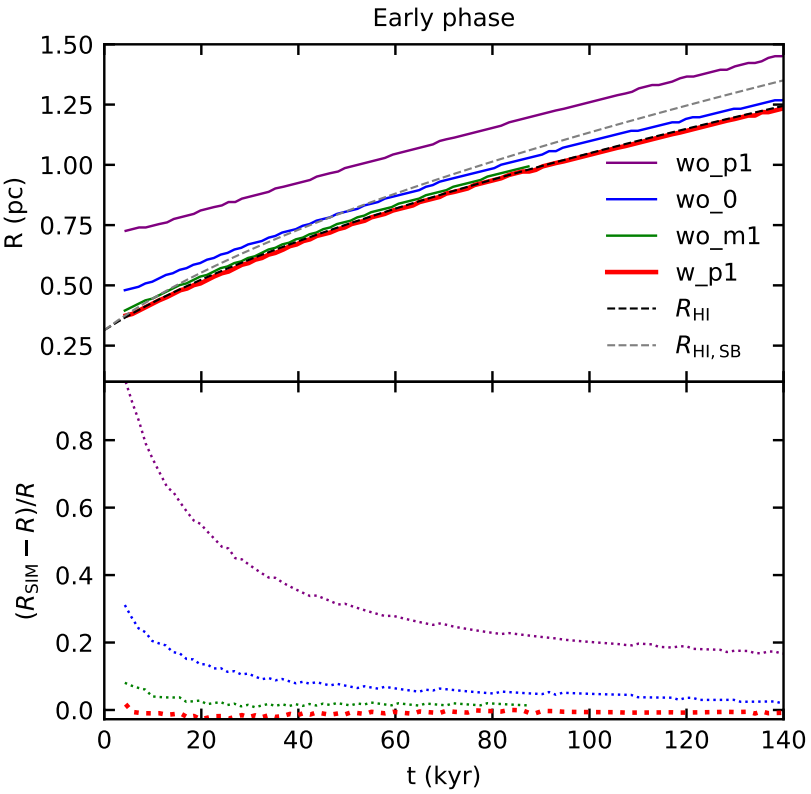

Figure 5.2: Early phase of the D-type expansion. The top panel shows the radius of the I-front as a function of time in our four test runs, plus two analytical solutions of Hosokawa and Inutsuka (2006a) marked by dashed lines: $R_{\rm HI}$, calculated using the mean sound speed of the ionized gas, and $R_{\rm HI,SB}$, calculated using a fixed sound speed of 12.85 km s^{-1}, as in the STARBENCH tests. The bottom panel shows the relative error in the radius in each simulation compared to $R_{\rm HI}$.

do not correct for the effects of recombinations within the ionized gas, the SPRAI algorithm removes too few photons within the ionized region. As a result, more photons reach the edge of the HII region than should be the case, leading to an overestimate of the size of the ionized region. At the same time, the photoionization and photoheating rates within the ionized gas are smaller than they should be, causing us to underestimate the ionization fraction and the temperature of the ionized gas. This is demonstrated quantitatively in Table 5.2, where we list the mean fractional ionization and temperature calculated within the inner 0.5 pc of the HII region in each run at a time 80.4 kyr. In run *wo_p1*, the gas in this region is only partially ionized and has a lower temperature than the gas in the same region in the runs with shorter $\Delta t_{\rm RT}$. This behavior can also be seen quite clearly in Figure 5.3, where we show spherically-averaged radial profiles of the fractional ionization, temperature, density and isothermal sound of speed at time $t = 80.4$ kyr.

Reducing the size of $\Delta t_{\rm RT}$ alleviates both problems, as expected. In particular, in run *wo_m1*, where $\Delta t_{\rm RT} \ll t_{\rm rec}$, we recover much more reasonable (although still slightly low) values for the fractional ionization and temperature in the HII region. However, the improved physical fidelity of the run with a smaller $\Delta t_{\rm RT}$ comes at a steep computational cost. Indeed, run *wo_m1* proved to be so costly that we were forced to terminate it after only 94.5 kyr.

Our new recombination correction also successfully eliminates the problems apparent in run *wo_p1*, but at much lower computational cost. From the Figures 5.2 and 5.3 and Table 5.2, we see that run *w_p1* produces very similar results to run *wo_m1* despite being carried out with a radiation timestep that is 100 times larger than in run *wo_m1*.

The expansion rate of the D-type front in *w_p1* also agrees well with the analytic solution of Hosokawa and Inutsuka (2006a):

$$R_{\rm HII} = R_{\rm St}\left(1 + \frac{7}{4}\sqrt{\frac{4}{3}}\frac{c_i t}{R_{\rm St}}\right)^{4/7}. \tag{5.22}$$

Here $R_{\rm St} = 0.314$ pc is the size of the Strömgren radius at point at which the I-front transitions from R-type to D-type. For the isothermal sound speed we took the value $c_i = 10.96$ km s^{-1}, which is the mean value within the ionized region in simulation *w_p1*. The main difference between the Hosokawa-Inutsuka solution and the better known Spitzer (1978a) solution is that the former accounts for the inertia of the shocked neutral gas, which is neglected in the Spitzer solution.

Note that although the setup of our test problem is very similar to the D-type ionization front test in the STARBENCH code comparison project, our solution for $R_{\rm HI}$ differs from their solution ($R_{\rm HI,SB}$, also shown in Figure 5.2). The reason for this is the difference in the temperature of the ionized gas in our calculation compared to the simulations presented in Bisbas et al. (2015). These simulations fix the temperature of the ionized gas at 10^4 K, corresponding to an isothermal sound speed $c_i = 12.85$ km s^{-1}. Our simulations do not prescribe the ionized gas temperature but instead solve for it self-consistently, with the result that we recover a slightly lower ionized gas sound speed and hence find slower expansion of the I-front than in Bisbas et al. (2015).

In the lower panel of Figure 5.2, we show the relative error between the position of the simulated I-front in each of the simulations and the Hosokawa-Inutsuka solution $R_{\rm HI}$. In

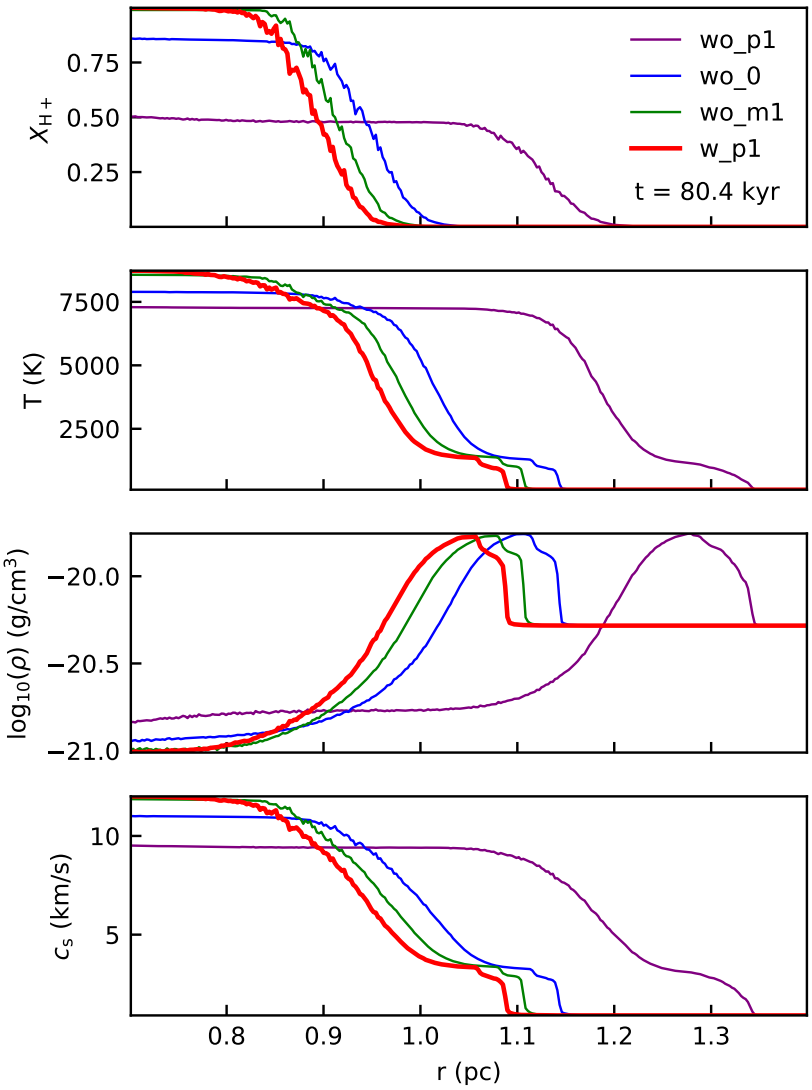

Figure 5.3: Radial profiles of various gas properties in the D-type test simulations at a time t = 80.4 kyr. From top to bottom, the panels correspond to the mass fraction of ionized hydrogen, the temperature, the density and the isothermal sound speed, respectively. The apparently extended nature of the transition from ionized to neutral gas is a consequence of the grid resolution: at a density of $10^{-20.5}$ g cm^{-3}, characteristic of this transition region, the radius of a single cell is $\sim$ 0.05 pc, and so the entire transition extends over only a couple of cell lengths.

the simulations without the recombination fix, the relative error is largest at the beginning of the simulation and decreases as the I-front grows. However, it remains significant in run *w0_p1* for the entirety of the time shown here, asymptoting to a value of around 20%. In contrast, in the run with the recombination fix, the relative error remains small throughout the simulation, never exceeding 2%.

5.3.1.2 Late phase expansion

We have also tested whether SPRAI recovers the correct behaviour of the D-type front at late times, as the ionized gas approaches pressure equilibrium with the surrounding neutral gas, again following the approach of Bisbas et al. (2015). The initial conditions in this case are similar to those for the early phase expansion described in Section 5.3.1.1, with a few minor changes. The simulation box now has a size of $L_{\rm box} = 10$ pc and the initial temperature of the hydrogen gas is $T_0 = 1000$ K. The higher initial temperature is necessary in order to ensure that the HII region can reach pressure equilibrium within a reasonable timescale. The other parameters of the problem are the same as in Section 5.3.1.1, except that in this case the system is evolved for 3 Myr, rather than 141 kyr.

We set up two different simulations. Simulation *wo_p1* is carried out without the recombination correction and with a radiation time-step that is an order of magnitude larger than the recombination time. Simulation *w_p1* is carried out with the same radiation time-step but includes the recombination correction. We do not carry out simulations analogous to the early phase runs *wo_0* and *wo_m1*, as the smaller size of the radiation time-step in these runs makes them too computationally demanding to run for long times.

In Figure 5.4, we demonstrate how the I-front radius evolves with time in simulations *wo_p1* (purple line) and *w_p1* (red line). The dotted lines show the late-time extension of the Spitzer solution given by Raga et al. (2012), denoted in the Figure as $R_{\rm RGI}$, with the grey line indicating what we obtain if we adopt a fixed sound speed of 12.85 km s^{-1}, and the black line showing the result when we use the mean sound speed of the ionized gas. The dot-dashed lines correspond to the late-time extension of the Hosokawa-Inutsuka solution (Raga et al., 2012), denoted in the Figure as $R_{\rm RGII}$, using the same color scheme. In their code comparison study, Bisbas et al. (2015) found that the actual late phase expansion of a D-type I-front initially overshoots $R_{\rm RGI}$, owing to the inertia of the expanding shell, before settling back to this solution at late times. They constructed the semi-empirical equation

$$R_{\rm SB} = R_{\rm RGII} + \left(1 - A\ \exp\left[-\frac{t}{\rm Myr}\right]\right)(R_{\rm RGI} - R_{\rm RGII})\,. \tag{5.23}$$

to describe this behaviour, with the fit parameter $A_{\rm SB} = 0.733$. This equation is denoted by the grey dashed line in Figure 5.4. The black dashed line shows a similar empirical fit in the case where we use the mean ionized gas sound speed, rather than the fixed value from Bisbas et al. (2015), with a smaller fitting parameter $A_{\rm SPRAI} = 0.474$.

Comparing the behaviour of our two simulations with these different predictions, we see first of all that run *wo_p1* agrees surprisingly well with the value of $R_{\rm SB}$ from STARBENCH. However, this appears to be a coincidence: the sound speed in the ionized gas in run *wo_p1*, and hence the thermal pressure, is lower than that assumed to derive $R_{\rm SB}$ and so there is

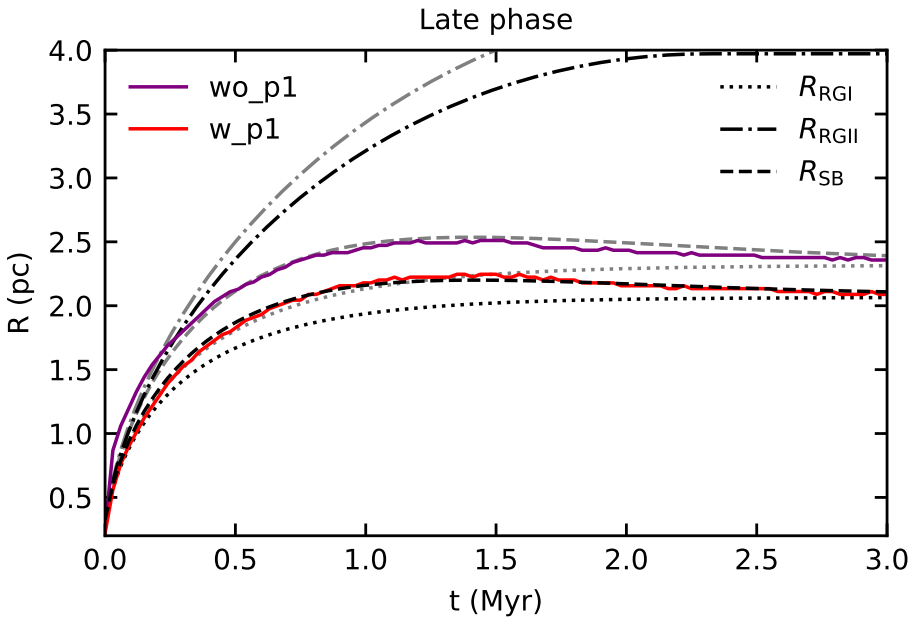

Figure 5.4: Test of the late phase expansion of a D-type I-front, using the same test setup as in the equivalent STARBENCH test. The purple line shows the result without the recombination correction (run *wo_p1*), while the red line shows the result when this is included (run *w_p1*). The other lines show various predictions computed using either a fixed ionized gas sound speed (grey) or the time-varying mean value taken from the simulation (black). For details of these predictions, see the discussion in Section 5.3.1.2.

no reason a priori why we should expect the results to agree. Looking at run *w_p1*, which we know from the previous section does a better job of modelling the early time evolution of the I-front, we see behavior which matches our expectations: the I-front radius initially overshoots the value of $R_{\rm RGI}$ computed using the appropriate ionized gas sound speed, but then settles back to this value at late times. This can be described with an equation of the form of Equation 5.23, but with a somewhat smaller fitting parameter than in the Bisbas et al. (2015) test ($A_{\rm SPRAI} < A_{\rm SB}$), likely due to the lower sound speed and consequent slower expansion of the I-front.

5.3.2 Multi-frequency ionization test

As described in Section 5.2.3, one of the new features in SPRAI-II is the inclusion of helium photoionization. In order to test that this new functionality is working correctly, we have run a test along the lines of the one presented in Paardekooper et al. (2015). We set up a 3D simulation box with a single source in the center. The box has a side length of 14 kpc and an initial particle density $n = 10^{-3}$ cm^{-3}. The gas consists of a mix of hydrogen and helium, with mass fractions of 0.76 and 0.24 respectively, and is initially neutral. Using this

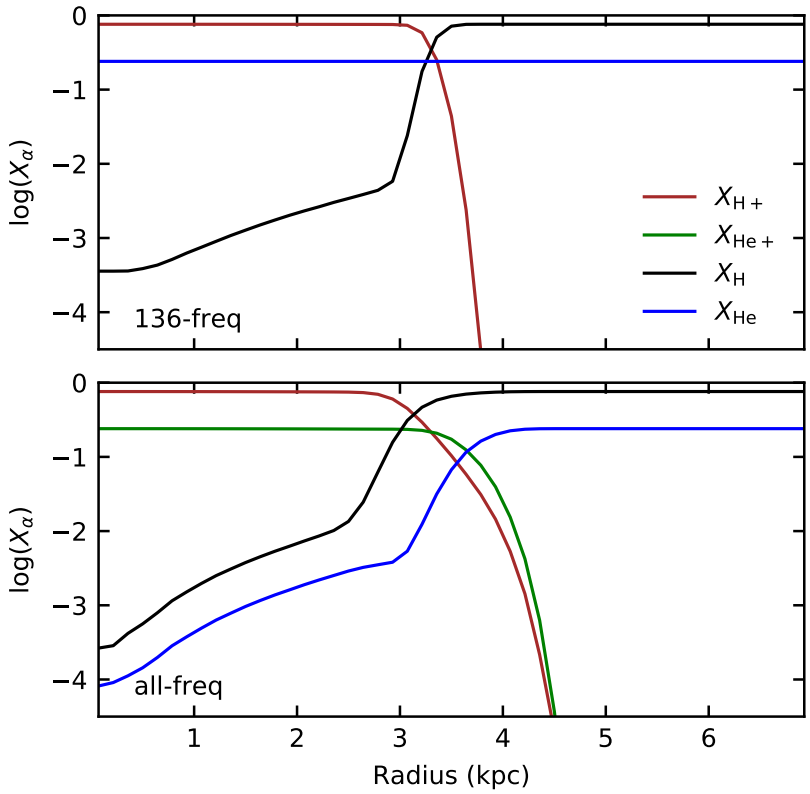

Figure 5.5: Results of the multi-frequency test (Section 5.3.2). The upper panel shows the radial profile at $t = 30$ Myr of the H, H^+, He and He^+ abundances surrounding a source emitting 5×10^{48} photons s^{-1} in the 13.6+ energy bin and no photons in any other energy bin. As expected, the photons create an HII region without an accompanying HeII region, as they have insufficient energy to ionized helium. In the lower panel, we show the abundance profiles we recover at the same output time if we instead distribute the same number of ionizing photons across all of the energy bins with the relative distribution matching that for a 10^5 K black body spectrum. In this case, an HeII region is formed that closely tracks the HII region.

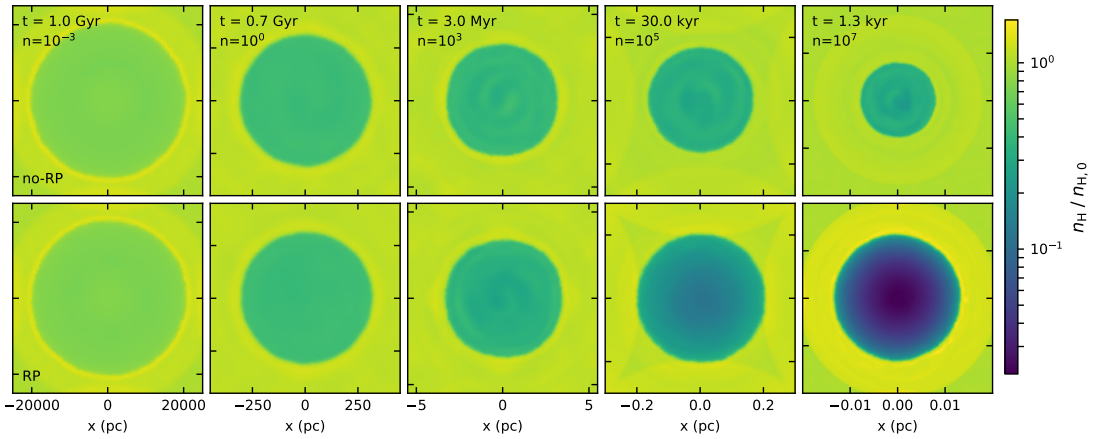

Figure 5.6: Density in a slice through the centre of each of the HII regions modelled in the radiation pressure test (Section 5.3.3). Each column has different initial settings. The labels in the upper row indicate the time corresponding to the slice and the initial density of the gas, in units of cm^{-3}. The upper row of panels shows results from runs without radiation pressure. The bottom row shows the same for runs with radiation pressure.

setup, we carry out two simulations. In the first, the source emits 5×10^{48} photons s^{-1} in the 13.6+ energy bin, with the emission in all of the other energy bins set to zero. In the second, we retain the same photon emission rate, but now distribute the photons amongst all of the different energy bins according to the spectral energy distribution of a 10^5 K black body. Both simulations are run for a total of 30 Myr each.

In Figure 5.5, we show the radial profile of the H, H^+, He and He^+ abundances at the end of each simulation. In the simulation with photons only in the 13.6+ energy bin, the expectation is that the code should produce an HII region but no HeII region, since the photons in this energy bin are unable to photoionize helium[5]. On the other hand, in the run with photons distributed over all bins, we expect the formation of an HeII region that coincides with the HII region (Osterbrock and Ferland, 2006). Figure 5.5 clearly demonstrates that the behaviour we recover in the simulations is completely in line with these theoretical expectations, demonstrating that helium photoionization is being treated correctly by the code.

5.3.3 Tests of direct pressure from ionizing radiation

This test is based on a similar test in the RAMSES radiation transfer implementation (RAMSES-RT) (Rosdahl and Teyssier, 2015). The setup is very simple. An ideal monochromatic source emitting 1.8×10^{50} photons s^{-1} in the 13.6+ radiation bin is placed at the centre of a box filled with hydrogen gas. The gas initially has a uniform H nuclei number density n_0 and

[5]Collisional processes within the HII region, such as collisional ionization of He or charge transfer from H^+ are able to produce some He^+ even in the absence of photoionization, but in practice the resulting He^+ fraction is very small.

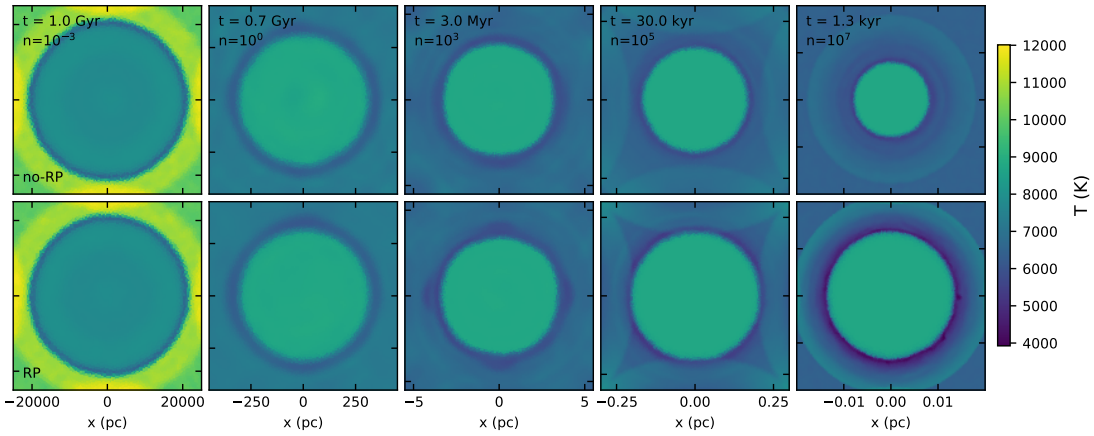

Figure 5.7: As Figure 5.6, but showing the temperature in the slice. The initial value of the gas temperature at the beginning of the simulation is 10^4 Kelvin.

n_0 (cm^{-3})	$L_{\rm box}$ (pc)	$t_{\rm max}$ (Myr)
10^{-3}	5×10^4	10^3
10^0	9×10^2	10^3
10^3	1.1×10^1	10^1
10^5	6×10^{-1}	3×10^{-1}
10^7	4×10^{-2}	10^{-2}

Table 5.3: Initial conditions for the radiation pressure tests. The columns from left to right correspond to the initial number density, the box size and the maximum time of the run, respectively.

temperature $T_0 = 10^4$ K. For the purposes of the test, we set the hydrogen photoionization cross-section to $\sigma_H = 2.32 \times 10^{-18}$ cm^2 and the mean excess energy to $\langle E_R \rangle = 0.756$ eV. In all tests we use periodic boundary conditions and an initial grid resolution of 64^3 zones. However, in the vicinity of the source, we further refine the cells using the same criterion as in Section 5.3.1.1.

We carry out five sets of simulations, which cover 10 orders of magnitude in number density, ranging from values characteristic of the high-redshift intergalactic medium to those found within dense, star-forming cores, as summarized in Table 5.3. Since the size of the low density bubble created by the radiation depends on the gas density, we use different box sizes L_{box} for the different simulations. For each initial density, we run two simulations: one in which we include the effects of radiation pressure (denoted *RP* below) and one in which we do not include its effects (denoted *no-RP*). All of the simulations make use of the recombination correction described in Section 5.2.2.

In Figure 5.6 we show slices through the density distribution in each simulation at the specified time. We see that in every case, the effect of the radiation source is to produce a low density bubble within the surrounding higher density gas. In the *no-RP* runs, this bubble is created purely by the thermal pressure of the ionized gas, as in the D-type I-front tests in the previous section. The runtime of each simulation is long enough to ensure that in every case the ionized bubble has reached pressure equilibrium by the end of the simulation. We therefore expect the final ionized gas density in the *no-RP* runs to be given by

$$n_{ion} = \frac{1}{2} n_{neut} \frac{T_n}{T_{ion}}, \tag{5.24}$$

where n_{ion} and n_{neut} are the number densities of H nuclei in the ionized and neutral gas, respectively, and T_{ion} and T_{neut} are the corresponding temperatures. The factor of two accounts for the presence of the electrons in the ionized gas. This expression assumes that the ionized gas and neutral gas are both isothermal. This assumption is violated in our simulations, but in practice the deviations from isothermality are small (see Figure 5.7) and so Equation 5.24 remains a useful guide to the expected value of n_{ion}. From Figure 5.7, we see that the temperature of the neutral gas at the end of the simulation ranges from $T_{neut} \sim 1.1 \times 10^4$ K in the lowest density run to $T \sim 7000$ K in the highest density run, while $T_{ion} \sim 9000$ K in every run. We therefore expect n_{ion}/n_{neut} to vary between 0.6 in the lowest density run and 0.4 in the highest density run, in good agreement with the behaviour we see in the upper panel in Figure 5.6. We have also verified that the final size of the HII region in each case is consistent with the value expected for the corresponding n_{ion} and T_{ion}.

In the *RP* runs, radiation pressure provides an additional outwards-pointing force on the ionized gas. The importance of this force depends on its size in comparison to the thermal pressure force: in cases where thermal pressure dominates, we expect to see very little change between the *no-RP* and *RP* runs, while in cases where radiation pressure dominates, or is simply comparable in magnitude to the thermal pressure, its inclusion should result in a much larger difference between the *no-RP* and *RP* runs. Following Rosdahl and Teyssier (2015), we can get a simple estimate of the likely importance of radiation pressure in each *RP* simulation by comparing the size that the bubble would have if it were entirely radiation pressure supported, r_γ, with the size of the thermal pressure supported bubble formed in

the corresponding *no-RP* simulation. In the case where radiation pressure dominates, the absorption of radiation occurs mostly at the edge of the bubble, and r_γ satisfies (Rosdahl and Teyssier, 2015)

$$n_{\rm neut} k_{\rm B} T_{\rm neut} = \frac{L}{4\pi r_\gamma^2 c}, \tag{5.25}$$

where $k_{\rm B}$ is Boltzmann's constant, L is the ionizing photon luminosity of the central source and c is the speed of light. In our test case, $L = 4.1 \times 10^{39}$ erg s^{-1} and so this yields

$$r_\gamma \simeq \frac{29}{(n_{\rm neut} T_{\rm neut,4})^{1/2}} \ {\rm pc}, \tag{5.26}$$

where $T_{\rm neut,4}$ is the temperature of the neutral gas in units of 10^4 K. Evaluating this for the different simulations, we find that for the runs with $n_0 = 10^{-3}, 10^0$ and 10^3 cm^{-3}, r_γ is much smaller than the size of the thermal pressure-supported bubble. We therefore expect radiation pressure to have little impact on the outcome of these simulations. On the other hand, for the run with $n_0 = 10^5$ cm^{-3}, r_γ is roughly half the size of the radius of the thermal pressure-supported bubble, while for the run with $n_0 = 10^7$ cm^{-3}, it is slightly larger. We would therefore expect radiation pressure to play a dynamically significant role in these two simulations.

Examination of Figure 5.6 shows that the results we obtain with SPRAI are completely in line with these expectations. In the three lower-density runs, the inclusion of radiation pressure has no significant effect on the size or density structure of the ionized bubble. On the other hand, in the run with $n_0 = 10^5$ cm^{-3}, where radiation pressure is important but sub-dominant, the bubble in the *RP* simulation is appreciably larger than in the *no-RP* simulation, and the radiation pressure has started to clear away some of the gas from the centre of the HII region. Finally, in the run with $n_0 = 10^7$ cm^{-3}, the size of the HII region in the *RP* simulation is substantially larger than in the *no-RP* simulation, and in addition the radiation pressure has driven most of the gas out of the centre of the HII region and into a thin dense shell at the edge of the ionized region.

5.4 Summary

In this chapter, we have presented extended version of SPRAI, an implementation of the SIMPLEX radiation transfer algorithm in the AREPO moving-mesh code. This new version of the code differs from the SPRAI-I, presented in Chapter 4, in three main respects. First, we have changed the way in which we compute the number of photons absorbed within each cell during a single timestep in order to properly account for the recombinations occurring in the cell during the timestep. This modification enables us to use SPRAI to model the growth of HII regions in dense gas without the need to limit the hydrodynamical timestep to be smaller than the recombination time $t_{\rm rec}$, thereby dramatically improving the computational performance of the code.

Second, we have improved the multifrequency treatment implemented in SPRAI by accounting for two new photochemical processes not included in SPRAI-I, the photoionization

of helium from He to He^+ and the photodissociation of H_2. We also account for the gas heating associated with these processes. These modifications improve the fidelity with which we can model the chemistry of metal-free HII regions and photodissociation regions (PDRs).

Finally, we have included a treatment of the effects of radiation pressure. We now track the momentum imparted to the gas each time an ionizing or Lyman-Werner photon is absorbed and update the gas velocity at the end of each radiation transfer step to account for the accumulated momentum.

Together, these updates to SPRAI equip it with the essential physical tools that are necessary to model radiative feedback from Pop-III stars in the early Universe. Our tests of the new features (Section 5.3) show that all are working well and we therefore consider SPRAI-II ready to be used for science applications. These will include the study of ionization feedback in Pop-III star formation (see the following Chapter 6), as well as investigations of cosmological reionization, the transition from Pop-III to Pop-II star formation and X-ray feedback from high-redshift X-ray binaries.

6 Radiation in Population III star formation

This chapter is an excerpt from the prepared paper about Population III stars star formation that we plan to submit to the journal after the publication of this thesis. I am the first author and prepared and ran all the simulations. We base our initial conditions of the cloud collapse from the previous simulations of K.M.J.Wollenberg. L. Haemmerlé and S. Geen helped on setting up the primordial stellar spectra. R.S.Klessen did the editing of the introduction text and S.C.O.Glover on the part with chemistry.

In this chapter, we present an application of the SPRAI radiation transport in the process of star formation. In the Section 6.1, we give an introduction and motivation for our simulations. Afterward, in Section 6.2, we describe the physics that we included in the model and in Section 6.3 our initial conditions. In the last two Sections 6.4 and 6.5, we present our results and give a discussion, respectively. The final Section 6.6 concludes our results.

6.1 Introduction

In this chapter, we study the impact of radiative feedback on the dynamical evolution of the star-forming gas with specific emphasis on resolving the immediate vicinity of the stars with very high precision. Since the protostellar Kelvin-Helmholtz contraction time decreases rapidly with increasing stellar mass, massive stars enter the hydrogen burning main sequence while still accreting (Zinnecker and Yorke, 2007; Maeder and Meynet, 2012). The resulting stellar parameters strongly depend on the details of the mass growth history, stressing again the importance of properly resolving the accretion flow onto the protostar in numerical simulations. In the low-mass halos investigated here, with typical accretion rates below $\dot{M} \approx 10^{-3}\,\mathrm{M}_{\odot}$, the resulting Pop-III stars are compact and very hot at their surface (Hosokawa and Omukai, 2009; Hosokawa et al., 2010, 2012). They emit large numbers of Lyman-Werner and ionizing photons (Schaerer, 2002) that can significantly influence their birth environment. And so, the question of how long the resulting HII regions remain small and compact, and when or whether they break out of the parental halo, is crucial for our understanding of how they might affect stellar birth in neighboring halos. Many aspects of this problem have been addressed, for example by Kitayama et al. (2004), Whalen et al. (2004), Alvarez et al. (2006), Abel et al. (2007), Yoshida et al. (2007), Greif et al. (2008), Wise et al. (2012b), Wise et al. (2012a), or Jeon et al. (2014). Here we focus on the impact of radiative feedback on the immediate birth environment of the star and on the question of how this influences the fragmentation behavior of the disk and the resulting stellar mass spectrum.

When studying this problem in primordial star formation, we can seek guidance from models of stellar birth at present days. Radiation hydrodynamic simulations in 2D and 3D (Yorke and Sonnhalter, 2002; Krumholz et al., 2009; Kuiper et al., 2010, 2011; Peters

et al., 2010, 2011; Commerçon et al., 2011; Rosen et al., 2016) demonstrate that once a protostellar accretion disk has formed, it quickly becomes gravitationally unstable and so material in the disk midplane flows inwards along dense filaments, whereas radiation escapes through optically thin channels above the disk. Even ionized material can be accreted, if the accretion flow is strong enough (Keto, 2007). Radiative feedback is thought not to be able to shut off the accretion flow onto massive stars. Instead it is the dynamical evolution of the disk material that controls the mass growth of individual protostars. Accretion onto the central object is shut off by the fragmentation of the disk and the formation of lower-mass companions which intercept inward-moving material (see, e.g. Girichidis et al., 2012). This requires 3D simulations, since the fragmentation process is not properly captured in two dimensions.

Due to the lack of metals and dust, the accretion disks around Pop-III stars can cool less efficiently and are much hotter than disks at present days (Tan and McKee, 2004; Glover, 2005). Similarly, the stellar radiation field couples less efficiently to the surrounding because the opacities are smaller (Glover, 2011). It is thus not clear how well the above results can be transferred to the primordial case. Radiation hydrodynamic simulations in 2D, for example, have been presented by Hosokawa et al. (2011), Hirano et al. (2014), and Hirano et al. (2015). They find that radiative feedback can indeed stop stellar mass growth and blow away the accretion disk, resulting in large HII regions that break out of the parental halo. They also report final stellar masses in the range from a few $10\,\mathrm{M}_\odot$ up to about $1000\,\mathrm{M}_\odot$. However, these calculations cannot capture disk fragmentation and the formation of multiple stellar systems. Three-dimensional calculations have been reported by Stacy et al. (2012), Susa (2013), Susa et al. (2014), and Hosokawa et al. (2016). These studies find widespread fragmentation, again with a wide range of stellar masses down to $\sim 1\,\mathrm{M}_\odot$. And again, they find that HII regions eventually break out and grow extremely large. But, also these simulations have their limitations and shortcomings, both in terms of resolution or in the number of physical processes included. High resolution is essential for correctly computing the recombination rate in ionized or partially ionized gas. It goes quadratic with the density, and consequently, not resolving the high-density shell of gas swept up by the expanding ionized bubble can result in dramatically wrong HII region expansion rates and sizes (see, e.g. Rahner et al., 2017, 2019). Similarly, treating only ionizing radiation and neglecting the impact of Lyman-Werner wavebands can lead to large errors in the overall photon escape fraction (Schauer et al., 2015).

Our goal here is to improve on both aspects. We demonstrate that sufficient numerical resolution and the correct treatment of all key radiative transfer processes lead to a qualitatively different picture than what was previously presented. We find that in many cases, the HII regions surrounding high-mass Pop-III stars are locally trapped and *do not* break out easily. This has considerable consequences for our understanding of the epoch of reionization and for cosmic metal enrichment. If photons do not travel far, Pop-III stars may not be important for the initial phases of cosmic reionization. Similarly, if the supernovae of Pop-III stars do not explode in large ionized cavities, but instead in regions of relatively high density, then the heavy elements produced in such events may not get far and early enrichment and mixing may be inefficient.

This chapter is structured as follows. The Section 6.2 describes numerical methods used

in our simulation setup. In the Section 6.3 we introduce our set of initial conditions and simulation settings. Results of the simulations are given in the following Section 6.4. After that, in Section 6.5 we discuss our results, show caveats of our model and compare our simulation technique with the recent literature. The last section concludes our findings and describes our further plans.

6.2 Numerical Methods

For our simulations we use a version of the cosmological hydrodynamical code AREPO (Springel, 2010) that incorporates several modules that we have developed for modelling Pop-III star formation. These include a detailed model of the chemistry and thermal physics of primordial gas, collisionless sink particles, which we use to represent individual Pop-III stars, and the SPRAI radiative transfer module (SPRAI-I: Jaura et al. 2018; SPRAI-II: Jaura et al. (2020)). The latter is a novel treatment of the effects of ionizing and photodissociating radiation based on the SIMPLEX algorithm (Kruip et al., 2010; Paardekooper et al., 2010). In this section, we describe each of these modules in more detail.

6.2.1 Chemistry and thermal physics

To model the chemistry of primordial gas, we use a similar chemical network to the one used by Wollenberg et al. (2019). This network is based on the one described in detail in Clark et al. (2011a), but includes several updates to the chemical rate coefficients, as outlined in Schauer et al. (2017b). The only significant difference between the chemical network used in our current study and the one adopted in these previous studies is the inclusion of the effects of photodissociating and photoionizing radiation from massive Pop-III stars. We include four main processes: Lyman-Werner (LW) photodissociation of H_2, and photoionization of H, He and H_2. The first three of these correspond to the reactions

$$H_2 + \gamma \rightarrow H + H, \tag{6.1}$$

$$H + \gamma \rightarrow H^+ + e^-, \tag{6.2}$$

$$He + \gamma \rightarrow He^+ + e^-. \tag{6.3}$$

The photoionization of H_2 in principle should be represented by the reaction

$$H_2 + \gamma \rightarrow H_2^+ + e^-, \tag{6.4}$$

but in the dense ionized gas that we are concerned with in this study, we assume that all of the resulting H_2^+ will rapidly be destroyed by dissociative recombination, resulting in the production of two hydrogen atoms. We therefore include this process using the pseudo-reaction

$$H_2 + \gamma \rightarrow H + H. \tag{6.5}$$

The reaction rates for these four processes are computed using the SPRAI radiation transfer module, described in Section 6.2.3 below. In principle, we should also account for the

photodetachment of H^- and photodissociation of H_2^+ by photons from the massive Pop-III stars. However, in practice, we do not expect these reactions to be important in the conditions simulated here, since we are primarily interested in the behaviour of the dense gas close to the stars, and in this dense gas, three-body formation of H_2 dominates over formation via the H^- or H_2^+ pathways.

As in Wollenberg et al. (2019), we also make the simplification that in gas denser than $n = 10^8$ cm^{-3}, the HD/H_2 ratio and atomic D/H ratio are both simply equal to the cosmological D to H ratio, $x_{\rm D,tot} = 2.6 \times 10^{-5}$, enabling us to neglect the portions of the chemical network involving deuterium. At high densities, the reactions responsible for converting H_2 to HD (or vice versa) and for transferring charge from H^+ to D and from D^+ to H are extremely rapid, and modelling them accurately in the chemical module is therefore computationally costly, and yet results in HD/H_2, D/H etc. ratios that are very close to the cosmological D to H ratio. Making this simplification therefore allows to substantially speed up our simulations while resulting in very little difference in the behaviour of the gas. As a consequence of this simplification, we do not explicitly treat the photoionization of D or photodissociation of HD in our model.

As well as the chemical evolution, we also solve simultaneously for the thermal evolution of the gas due to the effects of radiative and chemical heating and cooling. To model radiative cooling from H_2 rotational and vibrational line emission, we use the detailed H_2 cooling function presented in Glover and Abel (2008), updated as described in Glover (2015a). The effects of H_2 line opacity in dense gas are accounted for using the modified Sobolev approximation introduced by Clark et al. (2011b). Cooling due to collision-induced emission (CIE) from H_2 is accounted for using an optically thin rate from Ripamonti and Abel (2004) and the opacity correction described in Clark et al. (2011b). For HD cooling, we use the temperature and density-dependent rate given in Lipovka et al. (2005). We also account for radiative cooling due to electronic excitation of H, He and He^+, the recombination of H^+ and He^+, Compton cooling and bremsstrahlung using the rates given in Glover and Jappsen (2007). Radiative heating due to the photoionization of H, H_2 and He and the photodissociation of H_2 is computed using SPRAI (see later). Chemical heating due to H_2 formation and chemical cooling due to the collisional dissociation of H_2 and the collisional ionization of H and He are modelled as in Clark et al. (2011b).

Finally, we account for the fact that in gas with a significant molecular fraction, the adiabatic index γ varies as a function of the temperature and H_2 fraction. We use the HLLD Riemann solver built into AREPO (Pakmor et al., 2011), which supports the use of a variable γ, and compute the variation of γ with temperature and chemical composition using the same approach as in Boley et al. (2007).

6.2.2 Sink particles

Ideally, when modelling the formation of Pop-III stars, we would like to be able to follow the gravitational collapse of the gas down to the scale of the individual stars themselves. Unfortunately, the computational demands of doing so are extremely high. For example, Greif et al. (2012) follow the collapse of primordial gas down to scales of less than a solar radius, corresponding to protostellar densities. However, as a consequence, they are only

able to follow the evolution of the system for ~ 10 yr. This is orders of magnitude shorter than the time required to form even a single massive star, making this approach impractical for our purposes. Instead, it is necessary to use an approach in which the collapse of the gas is not followed down to such small length scales.

There are two main ways in which this can be accomplished. One possibility is to force the gravitational collapse of the gas to stop earlier than it would do in reality, by modifying either the equation of state or the cooling function (see e.g. Vorobyov et al., 2013; Machida and Nakamura, 2015; Hosokawa et al., 2016; Hirano and Bromm, 2017; Susa, 2019). Alternatively, collapsing regions can be removed from the simulation entirely and replaced with collisionless sink particles or sink cells (e.g. Clark et al., 2011b; Susa et al., 2014; Stacy et al., 2016).

In our simulations, we have chosen to use the latter approach. Our sink particle model is described in detail elsewhere (Wollenberg et al., 2019) and so here we give only a few basic details. AREPO grid cells become eligible for conversion into sink particles if they have densities exceeding a threshold density $n_{\rm th}$ and are also situated at a local minimum of the gravitational potential. In addition, the gas within a sphere of radius $r_{\rm acc}$ (the accretion radius) around the candidate cell must be gravitationally bound and collapsing. Finally, sink formation is suppressed in cells that are already closer than $r_{\rm acc}$ to an existing sink particle.

Once created, sink particles can accrete gas from any cells that are located at a distance $r \leq r_{\rm acc}$ from the sink. The gas must be gravitationally bound to the sink and the cell must have a density $n > n_{\rm th}$. If both of these conditions are satisfied, then the sink accretes sufficient gas from the cell to reduce the cell density to $n_{\rm th}$ (or 90% of the total cell gas mass if this is smaller). In the simulations presented in this chapter, we adopt a density threshold $n_{\rm th} = 7.248 \times 10^{13}\,{\rm cm}^{-3}$. We carry out simulations with three different values of the sink accretion radius, 2, 10 and 30 AU, as summarized in Table 6.2 and discussed in more detail Section 6.3.

As our sinks represent individual protostars (or, later, main sequence stars), it is also necessary to account for the energy released as gas accretes onto their surfaces. The contribution that this makes to the flux of ionizing and photodissociating photons is accounted for using the method described in Section 6.2.3.1 below. However, in addition, it is also necessary to account for the heating of the gas by the accreting protostars prior to them reaching the main sequence. This accretion luminosity is typically characterised by a low radiation temperature and hence does not contribute to the aforementioned fluxes, but nevertheless is important for regulating the fragmentation of the gas (Smith et al., 2011). We treat the effects of this accretion luminosity heating using the method described in detail in Wollenberg et al. (2019), which itself is a slightly modified version of an approach first used in Smith et al. (2011). Briefly, we use a simple model of the pre-main sequence evolution of the protostars to solve for their bolometric luminosity as a function of their mass and their current accretion rate. Since the effective temperatures of the protostars during the pre-main sequence phase are typically $T_{\rm eff} \ll 10^4$ K, we assume that the gas surrounding them is optically thin to their continuum emission, meaning that the flux of radiation at a distance R from a protostar with accretion luminosity L is simple $F = L/(4\pi R^2)$. The heating rate of

the gas due to this flux then follows from

$$\Gamma_{\rm acc} = \rho \kappa_{\rm P}(\rho, T) F, \tag{6.6}$$

where ρ is the gas density and $\kappa_{\rm P}$ is the Planck mean opacity of the gas at its current density and temperature, which we interpolate from the values tabulated by Mayer and Duschl (2005).

6.2.3 Modelling ionizing and photodissociating radiation with SPRAI

While the accreting protostars remain in the pre-main sequence phase of their evolution, they have large radii and low effective temperatures (Omukai and Palla, 2001, 2003) and primarily affect their surroundings via the accretion luminosity heating discussed in the previous section. However, as a Pop-III protostar approaches the main sequence, its radius significantly decreases and its effective temperature substantially increases (see Figure 6.1). As a consequence, the star becomes a source of both ionizing and photodissociating photons, provided its mass is large enough.

To manage the transport of ionizing and photodissociating radiation through the Voronoi mesh cells in our simulations and to compute the resulting photochemical and heating rates, we use the SPRAI radiation transfer module, described in previous Chapters 4 (Jaura et al., 2018) and 5 (Jaura et al., 2020), SPRAI is a ray-tracing method based on the SIMPLEX algorithm of Kruip et al. (2010) and Paardekooper et al. (2010), which is a variant of the short characteristics approach. At the beginning of each full hydrodynamical timestep[1], SPRAI calculates the number of photons emitted by each source in each of the tracked energy bins, using the procedure described in Section 6.2.3.1 below. These photons are distributed equally amongst a set of directional bins associated with the gas cell in which the source resides. The photons are then moved step by step on the mesh along paths that approximately follow the directions defined by the directional bins. The effects of attenuation are computed for each cell that the photons pass through and the photons are propagated until they are completely attenuated. Finally, the number of photons in each energy bin absorbed in each cell during the timestep is used to calculate the corresponding photoionization, photodissociation and photoheating rates, which are passed on to the chemistry module.

A strength of SPRAI in comparison to more conventional long characteristics methods (e.g. Wise and Abel, 2011) is that every cell can potentially act as a source cell and hence the computational cost of the method is determined by the number of cells that are ionized and not be the number of ionizing sources. This makes it a good choice for situations containing multiple sources of radiation, as in the simulations described later in this chapter.

6.2.3.1 Emission from accreting Population III stars

The sink particles formed in our simulations are taken to represent individual Pop-III stars, and therefore each acts as a source of radiation. To model the emission from each sink, we make use of the Pop-III stellar models presented in Haemmerlé et al. (2018). These models

[1] A full hydrodynamical timestep in AREPO is one on which all of the mesh cells are synchronized.

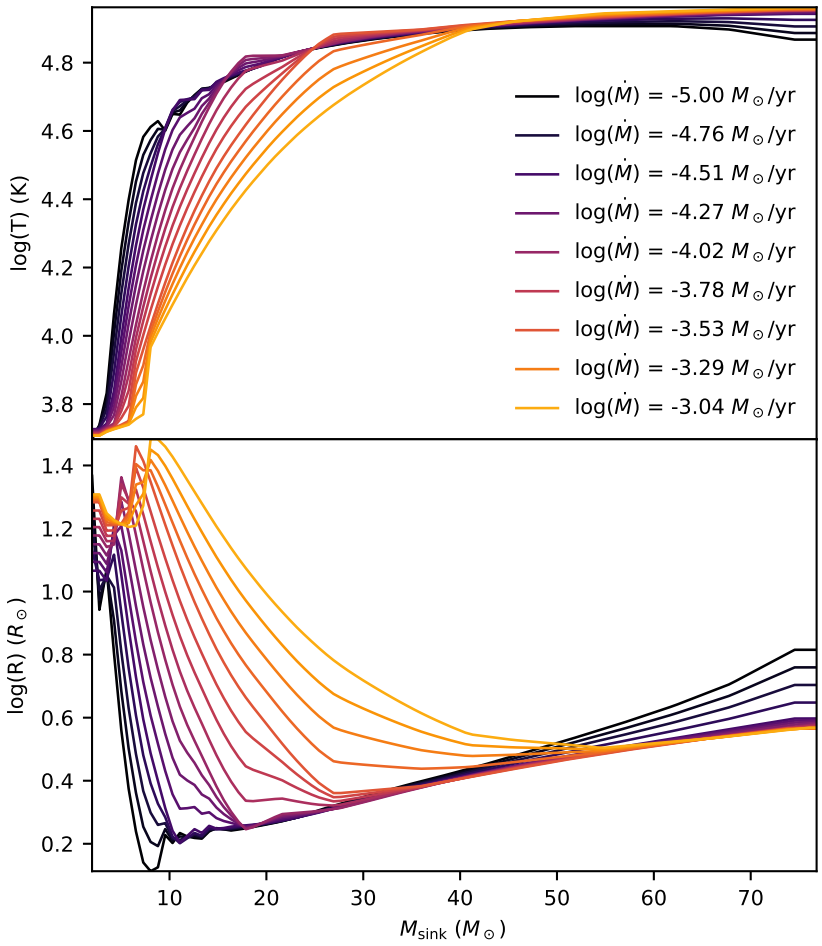

Figure 6.1: Dependence of the stellar effective temperature (top) and the stellar radius (bottom) on the mass of the star and its accretion rate. Radii and temperatures for stars heavier than 75 $M_\odot$ stay constant.

Bin (eV)	H_2^{dis}	H^{ion}	H_2^{ion}	He^{ion}
11.2 - 13.6	✓	-	-	-
13.6 - 15.2	✓	✓	-	-
15.2 - 24.6	-	✓	✓	-
24.6+	-	✓	✓	✓

Table 6.1: List of energy bins and the processes for which they are responsible.

use the current mass of the star together with its mass accretion rate in order to compute the stellar radius R_* and effective temperature $T_{\rm eff}$ of the accreting stars. The total luminosity then follows trivially from the Stefan-Boltzmann equation:

$$L = 4\pi\sigma_{\rm SB} R_*^2 T_{\rm eff}^4, \tag{6.7}$$

where $\sigma_{\rm SB}$ is the Stefan-Boltzmann constant. The dependence of R_* and $T_{\rm eff}$ on the stellar mass and accretion rate is illustrated in Figure 6.1.

The values of R_* and $T_{\rm eff}$ in Figure 6.1 depend significantly on the current accretion rate onto the star. To calculate this accretion rate, we divide the change in mass of the sink over the last full hydrodynamical timestep by the size of the timestep. A maximum possible full hydrodynamical timestep $\Delta t_{\rm max}$ in all our simulations is set to 1 year.

Given the luminosity and effective temperature of each star, we can then compute the number of photons per unit time that each emits in the various photon energy bins tracked by SPRAI. As discussed in more detail in Chapter 5, we currently track photons in four bins with the following energy ranges:

$$\begin{array}{rcrcl} 11.2 & < & E & < & 13.6\,\text{eV} \\ 13.6 & < & E & < & 15.2\,\text{eV} \\ 15.2 & < & E & < & 24.6\,\text{eV} \\ & & E & > & 24.6\,\text{eV} \end{array} \tag{6.8}$$

For consistency with SPRAI-II, we will refer to these as the 11.2+, 13.6+, 15.2+ and 24.6+ bins, respectively.

Our choice of energy bins is motivated by the fact that the four photochemical processes we are interested in tracking – H_2 photodissociation and the photoionization of H, H_2 and He – have different energy thresholds. Table 6.1 summarizes which bins correspond to which processes, and Figure 6.2 shows the cross-section adopted for each process. The cross-sections we use for the photoionization of H, H_2 and He are taken from Osterbrock (1989), Liu and Shemansky (2012) and Verner et al. (1996), respectively. Our treatment of H_2 photodissociation is slightly more complicated and is discussed in Section 6.2.3.2 below.

For H_2 photodissociation, we follow Baczynski et al. (2015) and use an effective, frequency-independent cross-section derived by taking the ratio of the photodissociation rate to the Lyman-Werner photon flux in the optically thin limit. We discuss the limitations of this approach in more detail in Section 6.2.3.2 below.

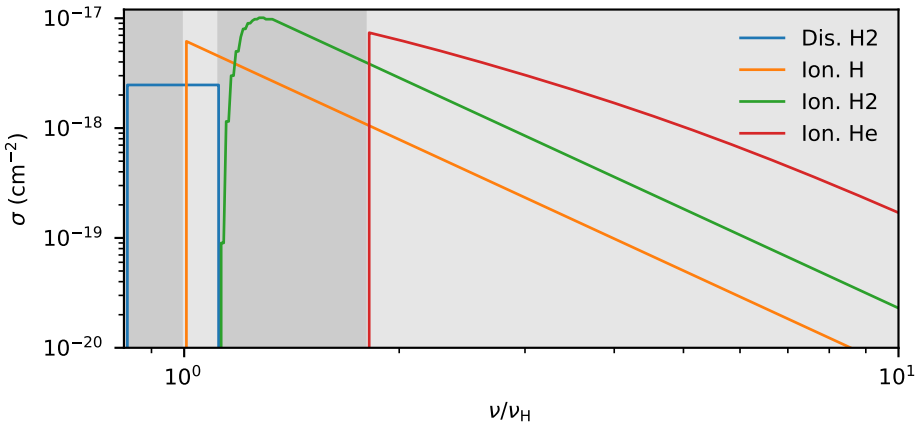

Figure 6.2: Cross-sections adopted for the different photochemical processes included in our chemical model. The shaded regions correspond to the different energy bins: from left to right, we have the 11.2+, 13.6+, 15.2+ and 24.6+ bins, respectively.

6.2.3.2 Treatment of Lyman-Werner radiation

H_2 photodissociation by photons in the LW bands of molecular hydrogen is a two-stage process driven by line absorption, and is hence inherently more complicated to model than the photoionization of H, H_2 or He. Accurately modelling the absorption of radiation in each of the individual Lyman and Werner lines would require an extremely high number of frequency bins and hence is not computationally feasible in the context of our simulations. Instead, we follow Baczynski et al. (2015) and adopt a frequency-independent cross-section of $\sigma_{H_2,\mathrm{dis}} = 2.47 \times 10^{-18}$ cm^2 for this process. Baczynski et al. (2015) derived this value by taking the ratio of the photodissociation rate computed by Röllig et al. (2007) for the Draine (1978) interstellar radiation field and the photon flux given by Draine and Bertoldi (1996) for the same field. Although the Draine (1978) field is unlikely to be a particularly good representation of the ultraviolet radiation field produced by massive Population III stars stars, the ratio of the photodissociation rate and photon flux varies only weakly with changes in the spectral shape, and so our adopted value of $\sigma_{H_2,\mathrm{dis}}$ should still a reasonable representation of the behaviour we expect in the optically thin regime.

A more significant problem is the fact that we expect $\sigma_{H_2,\mathrm{dis}}$ to decrease as the H_2 column density between the gas and the source of radiation increases, owing to the increasing effectiveness of H_2 self-shielding. This is commonly accounted for through the use of a self-shielding function that is a function of the H_2 column density (see e.g. Draine and Bertoldi 1996, Wolcott-Green and Haiman 2011). Unfortunately, this approach is not viable in SPRAI, as the LW photons entering a cell carry no information with them on their source (or sources), and so it is not clear what H_2 column density should be used to compute the self-shielding function. We deal with this problem simply by ignoring the self-shielding correction and assuming that $\sigma_{H_2,\mathrm{dis}}$ remains unaltered regardless of whether we are in the

optically thin or optically thick regimes. Consequently, we under-estimate the reduction of the H_2 photodissociation rate at moderate H_2 column densities and over-estimate it at high H_2 column densities. However, this will have a significant impact on our results only in circumstances where we resolve the H_2 photodissociation front. In the dense, highly molecular gas that is the main focus of our current study, this front is not resolved, and so our results should be insensitive to this simplification.

Finally, in addition to the absorption of LW photon by H_2, we also account for the absorption of photons in the 11.2+ bin by the Lyman series lines of atomic hydrogen. This can become important when the atomic hydrogen column density is very large (Wolcott-Green and Haiman, 2011; Glover, 2017; Schauer et al., 2017a) and in dense gas acts to prevent the photodissociation front from advancing much beyond the ionization front (Glover, 2017). We model this process using an effective absorption cross-section of $\sigma_{\rm Lyman} = 5.23 \times 10^{-25}\,{\rm cm}^2$, based on Wolcott-Green and Haiman (2011).

6.3 Initial conditions

Following Wollenberg et al. (2019), we start our simulations from a simplified set of initial conditions that allow us to control the initial turbulent and rotational energy present in the gas. In a simulation box of size 13 pc we set up a Bonnor-Ebert sphere (BES) density profile. This has a density that is everywhere a factor of $f = 1.83$ larger than the density of a critical BES, a central density $n_{\rm c} = 1.83 \times 10^4\,{\rm cm}^{-3}$, a radius $R = 1.87$ pc a mass $M = 2671\,{\rm M}_\odot$, and a uniform temperature $T = 200$ K.

The gas is initially in solid body rotation and also has a random turbulent velocity component, generated as described in Wollenberg et al. (2019). The strength of the initial rotation and turbulence are parametrised by

$$\beta_{\rm rot} = \frac{E_{\rm rot}}{|E_{\rm grav}|} \quad \text{and} \quad \alpha_{\rm turb} = \frac{E_{\rm turb}}{|E_{\rm grav}|}, \tag{6.9}$$

where $E_{\rm rot}$ is the rotational energy, $E_{\rm turb}$ is the turbulent kinetic energy and $E_{\rm grav}$ is the initial gravitational energy of the BES. We carry out simulations using two different initial conditions, one turbulence-dominated ($\beta_{\rm rot} = 0.01, \alpha_{\rm turb} = 0.25$) and one rotation-dominated ($\beta_{\rm rot} = 0.1, \alpha_{\rm turb} = 0.001$). For each set of initial conditions, we run simulations using three different values of the sink accretion radius, $r_{\rm sink} = 2, 10$, and 30 AU. Table 6.2 summarizes the different combinations of parameters used in the simulations.

We follow the collapse of the whole BES until the first sink particle forms. This occurs around 700–750 kyr after the beginning of the simulation, depending on the adopted values of $\alpha_{\rm turb}$ and $\beta_{\rm rot}$ (see Table 6.2). We temporarily halt the simulation and select a region of size 3.9 pc around the densest point. Subsequently, we continue to simulate this selected region using outflow boundary conditions. We do this for reasons related to how SPRAI functions. As described in Section 6.2.3 above, photon transport in SPRAI occurs only on timesteps on which all the AREPO grid cells are synchronized. For reasons of accuracy, we do not want the synchronization timestep to be enormously larger than the natural hydrodynamical timestep of the densest cells. However, if we limit all the cells in our

Name	$r_{\rm sink}$ (AU)	$\beta_{\rm rot}$	$\alpha_{\rm turb}$	$t_{\rm coll}$ (kyr)
T2	2	0.01	0.25	705.135
T10	10	0.01	0.25	716.665
T30	30	0.01	0.25	716.665
R2	2	0.1	0.001	743.686
R10	10	0.1	0.001	743.687
R30	30	0.1	0.001	743.687

Table 6.2: Summary of the initial settings of our simulations. $\alpha_{\rm turb}$ and $\beta_{\rm rot}$ are ratios of the turbulent and the rotational kinetic energy to the gravitational energy, respectively. For each simulation we also list the sink accretion radius $r_{\rm sink}$ and the formation time of the first sink particle $t_{\rm coll}$.

initial 13 pc box to a small timestep, this is computationally inefficient, as we then spend considerable time evolving cells far from the centre of the simulation on timesteps that are much shorter than their natural hydrodynamical timestep. Cutting out the central dense region and continuing the simulation with only this region mitigates this cost without significantly affecting the outcome of the simulation.

Following the formation of the first sink particle, we run three variants of each simulation to help us better understand the effect of the radiative feedback on the surrounding gas. We denote them as follows:

NF – no radiation feedback

RTP – with ionizing radiation and radiation pressure

RTPr – as RTP, but with no absorption for $r < r_{\rm sink}$

The first two setups are self-explanatory, but the last deserves further comment. In setup RTPr, we modified SPRAI to disable the absorption of photons within the accretion radius $r_{\rm sink}$ around all sink particles with masses higher than $M_{\rm sink} = 10\,{\rm M}_\odot$. Outside of $r_{\rm sink}$, the treatment of attenuation and photochemistry stay the same as in the usual version of the code. Radiation from sinks with masses $M < 10\,{\rm M}_\odot$ is treated in the usual fashion. We discuss the motivation for this unusual setup in Section 6.5.3 below.

6.4 Results

All of our simulations show qualitatively similar behaviour prior to the onset of radiative feedback from massive ($M > 10\,{\rm M}_\odot$) stars. As in many previous simulations of Pop-III star formation, H_2 cooling allows the gas to collapse quasi-isothermally over many orders of magnitude in density, resulting in the gas developing a $\rho \propto R^{-2.2}$ density profile. Eventually, a Pop-III protostar forms, surrounded by a dense accretion disk which soon thereafter fragments, yielding a compact cluster of interacting protostars. Some protostars are ejected by dynamical encounters, but those that remain close to the centre of the gas distribution

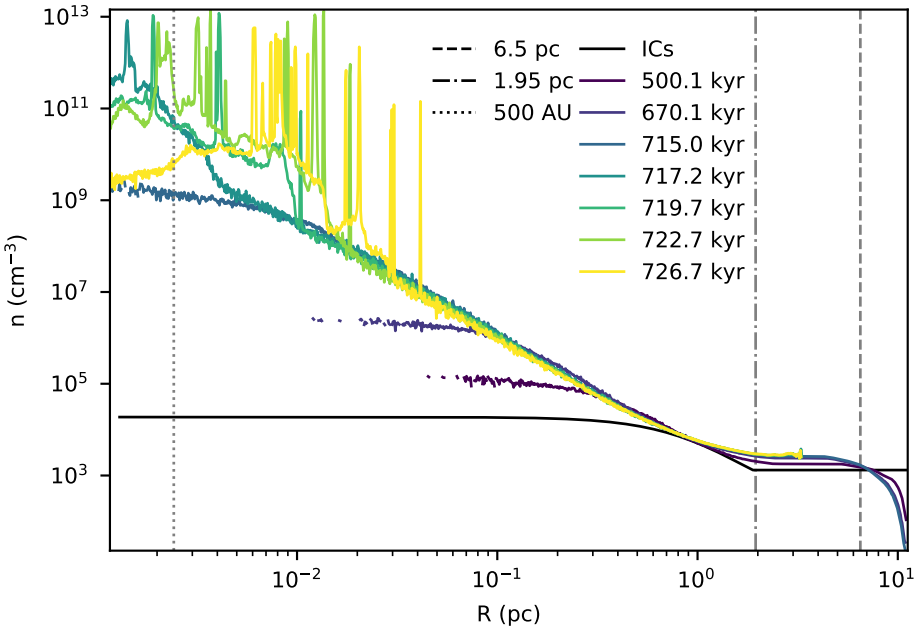

Figure 6.3: Average number density as a function of the distance from the centre of the collapse in simulation T10_NF at various different output times. For reference, the first sink formed in this simulation at a time $t_{\rm coll} = 716.7$ kyr. Vertical lines denote the size of the initial box $R_{\rm box} = 6.5$ pc (dashed), the cutout region $R_{\rm cut} = 1.95$ pc (dashed-dotted) and the inner 500 AU (dotted).

grow in mass over time through accretion from the surrounding gas reservoir. Once one or more stars reaches a mass of $M_{\rm star} \sim 10$–$20\ {\rm M}_\odot$, they become hot enough to start to emit significant numbers of ionizing and photodissociating photons (see Figure 6.1; the precise mass at which this occurs depends on the accretion rate onto the star). From this point on, greater differences become apparent between the different simulations, as we explore in more detail in the sections below.

6.4.1 Collapse and fragmentation of the BES

As a representative example of the behaviour of the gas in the simulations during the initial collapse phase and subsequent onset of fragmentation, we show in Figure 6.3 the average gas number density as a function of the radial distance from the center of mass in run T10_NF at several output times. After the formation of the first sink particles at $t_{\rm coll} = 716.7$ kyr, the whole system fragments into several high density regions that rotate around their common center of mass and drift apart. Interactions between fragments are common, leading to preferential ejection of low mass sink particles, which often end up at very large distances from the center of the simulation volume.

Figure 6.4 illustrates the resolution achieved in the same simulation at the final output time, $t = 20$ kyr after the formation of the first sink particle. The left-hand panel in the

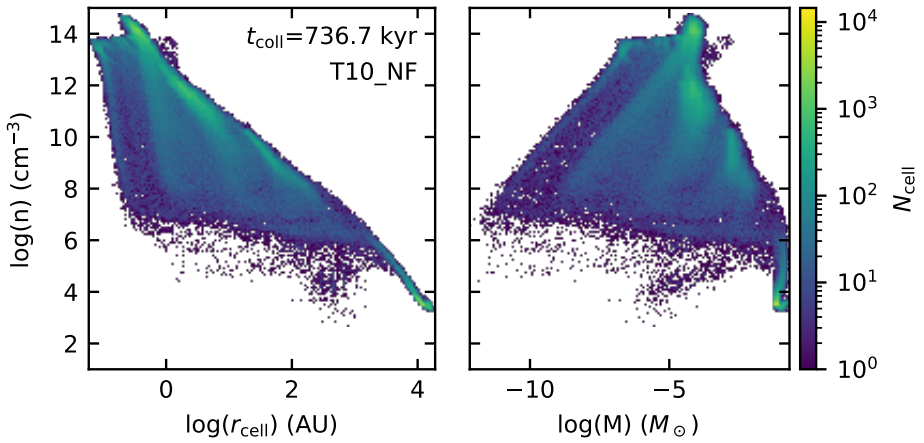

Figure 6.4: Histogram of gas cell radii (left) and masses (right) as a function of the density in the simulation T10_NF at the final output time.

figure shows the size distribution of the Voronoi mesh cells, quantified by their effective radii, $r_{\rm cell} = (3V/4\pi)^{1/3}$, where V is the cell volume. The right-hand panel shows the distribution of the corresponding cell masses. Highly populated portions of the histogram correspond to different collapsing fragments. Similar resolutions are achieved in the other simulations. At densities characteristic of the central accretion disk ($n > 10^{11}$ cm^{-3}), all of the cells have sizes below 10 AU (with some being much smaller) and have masses $M_{\rm cell} < 10^{-3}$ M$_\odot$. At densities close to our sink formation threshold ($n \sim 10^{14}$ cm^{-3}), all of the cells have radii < 1 AU and masses $M_{\rm cell} < 10^{-4}$ M$_\odot$. Note also that the absence of cells with $r_{\rm cell} \ll 1$ AU and densities $n > n_{\rm th}$ is a consequence of our sink particle algorithm: cells with radii this small lie inside the accretion radius of a sink and so accretion onto the sink therefore maintains their density at $n \leq n_{\rm th}$ by construction.

In Figure 6.5, we show the positions of the sink particles in run T10_NF at a time t = 723.7 kyr, roughly 7 kyr after the formation of the first sink. The rows from the top to bottom show face-on (left panels) and edge-on (right panels) column-averaged gas number density for boxes with sizes of 24000, 2400 and 240 AU, respectively. All of the plots are centered on the most massive sink particle present in the simulation, which remains close to the dynamical center of the gas distribution. Black crosses denote the positions of the individual sink particles. The disk-like morphology of the gas distribution is plain, particularly in the lowest panel, as are the spiral arms created by the gravitational instability of the disk. The sinks all form within the disk, but interactions lead to many of the smaller sinks being ejected (see especially the upper panels).

If we look in more quantitative detail at the properties of the sink particles formed in the different simulations, differences become apparent. The panels in Figure 6.6 show, from top to bottom, the time evolution of the number of sink particles and the total mass accreted by the sink particles, respectively. Note that the color scheme and line styles used in Figure 6.6

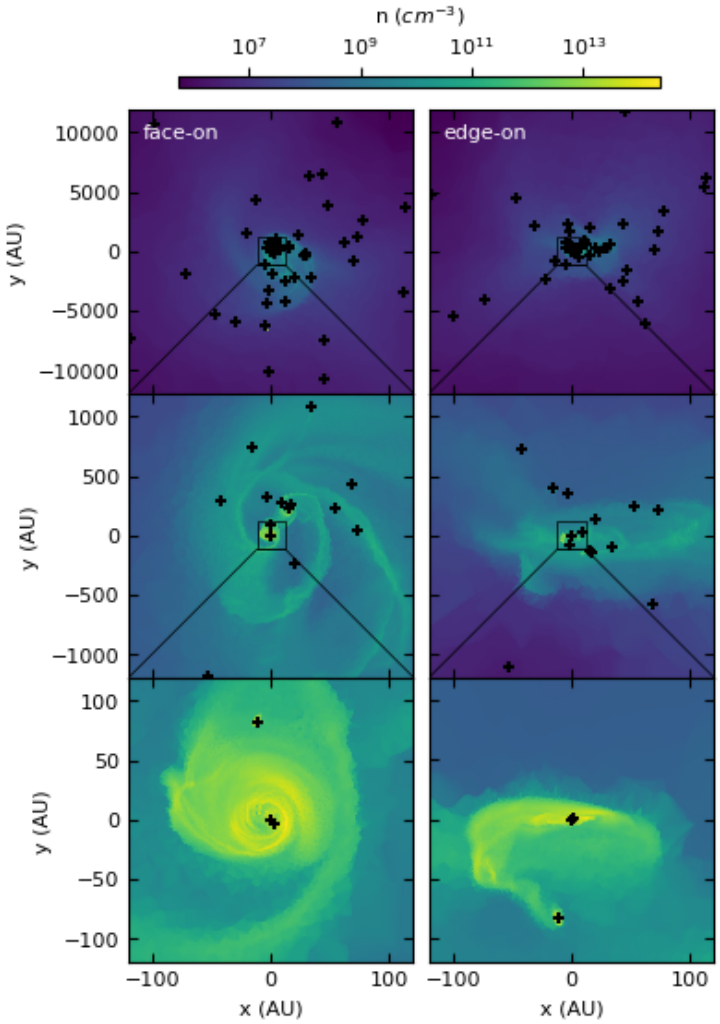

Figure 6.5: Face-on (left) and edge-on (right) projections of the column-averaged gas number density in simulation T10_NF centered on the most massive sink particle. Panels from top to bottom show box projections with sizes of 24000, 2400 and 240 AU, respectively. Crosses denote positions of the sink particles.

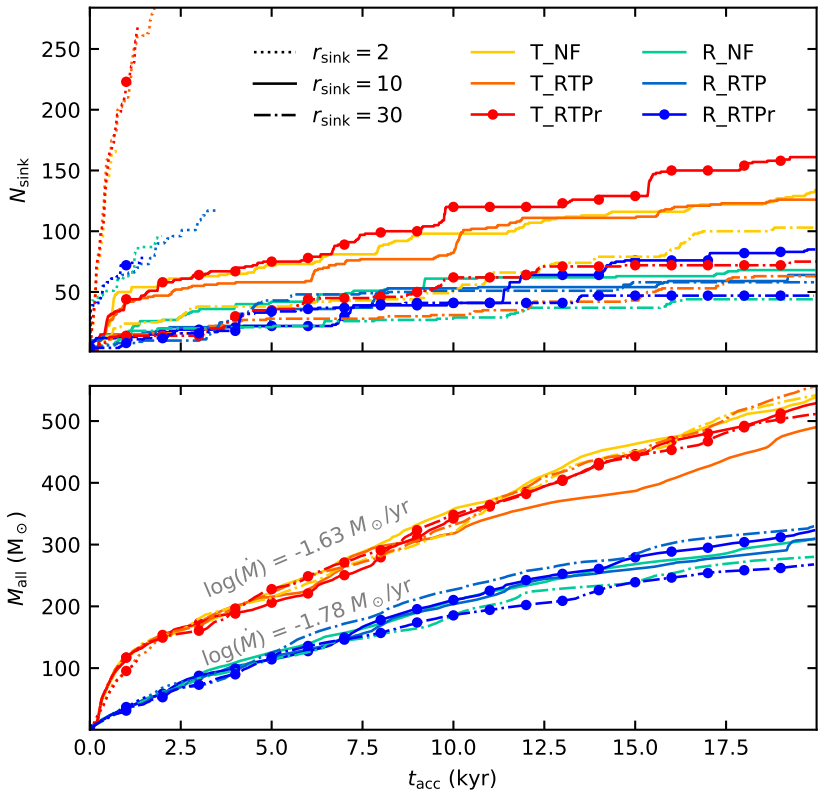

Figure 6.6: Time evolution of the total sink particle number (upper panel) and total mass accreted by sink particles (lower panel). In the lower panel we also indicate the average mass infall rates for the rotation-dominated and turbulence-dominated simulations.

are also used in later figures, to make it easy to distinguish the different simulations. Results from the simulations with high initial turbulence and low initial rotation are drawn in red tones, while those from the simulations with high initial rotation and low initial turbulence are shown in blue tones. Dots on the line plots indicate the runs in which absorption of radiation within $r_{\rm sink}$ is neglected.

As in Wollenberg et al. (2019), we find that the total mass accreted by the sink particles is sensitive to the amount of rotational energy in the initial conditions. Gas in the simulations with a higher initial β collapses more slowly than in the runs with low initial β, resulting in a systematically smaller total accretion rate and a difference in the total mass accreted of roughly a factor of two by $t = 20$ kyr. Amongst the runs with a given initial β, we find only minor variations in the total accreted gas mass, with no systematic trend with sink accretion radius or with the details of the radiative feedback. If we look at the number of sinks formed in each simulation, however, we find much greater variation, and in particular a strong systematic trend as a function of $r_{\rm sink}$. Runs with a smaller accretion radius form far more sink particles than those with a larger accretion radius. Indeed, so many sinks formed in the simulations with $r_{\rm sink} = 2$ AU that it became computationally prohibitive to keep the runs going for more than a few kyr. This high sensitivity to $r_{\rm sink}$ is a consequence of our sink particle algorithm, which does not allow new sinks to form within the accretion radius of existing sinks. This restriction is necessary to avoid artificial fragmentation of the gas, but means that we also miss some real small-scale fragmentation. That said, it is likely that many of the fragments forming within a few AU of each other would in reality merge (Wollenberg et al., 2019; Susa, 2019) and so our runs with higher $r_{\rm sink}$ are arguably more representative of the real behaviour of Pop-III star-forming systems.

We continued all of the simulations with sink accretion radii of 10 or 30 AU to a final time $t_{\rm acc} = 20$ kyr after the formation of the first sink. During this period, each simulation produced between 40 and 150 sink particles. Their final mass distributions are shown in Figure 6.7. In this figure, the rows from top to bottom correspond to setups T10, T30, R10 and R30, respectively. Three different bar plots in each row show our three radiation setups NF, RTP and RTPr, respectively. The median values (dotted lines) for each distribution are also indicated in each plot.

Looking at the mass distributions, we see that the runs with high initial turbulence produce a clear peak between 0.1 and 1 $M_\odot$, although overall the distribution remains much flatter than we find for the present-day stellar initial mass function (see e.g. Kroupa, 2002). On the other hand, the runs with high initial rotation do not display any clear peak. Minor differences are apparent in the mass distributions recovered from simulations with different radiation setups, but the significance of these variations is unclear as they are comparable to the run-to-run variations found by Wollenberg et al. (2019) for simulations differing only in the random realization of the initial turbulent velocity field.

To summarize: the main quantities determining how much fragmentation occurs in the simulations and how much mass is accreted by sinks are the initial values of α and β and the sink accretion radius $r_{\rm sink}$, with the latter affecting only the amount of fragmentation and not the total accretion rate. On the other hand, the details of the radiative feedback have very little impact on either the number of sinks formed or the total mass accreted, at least on a 20 kyr timescale. In the next section, we explore why this is the case.

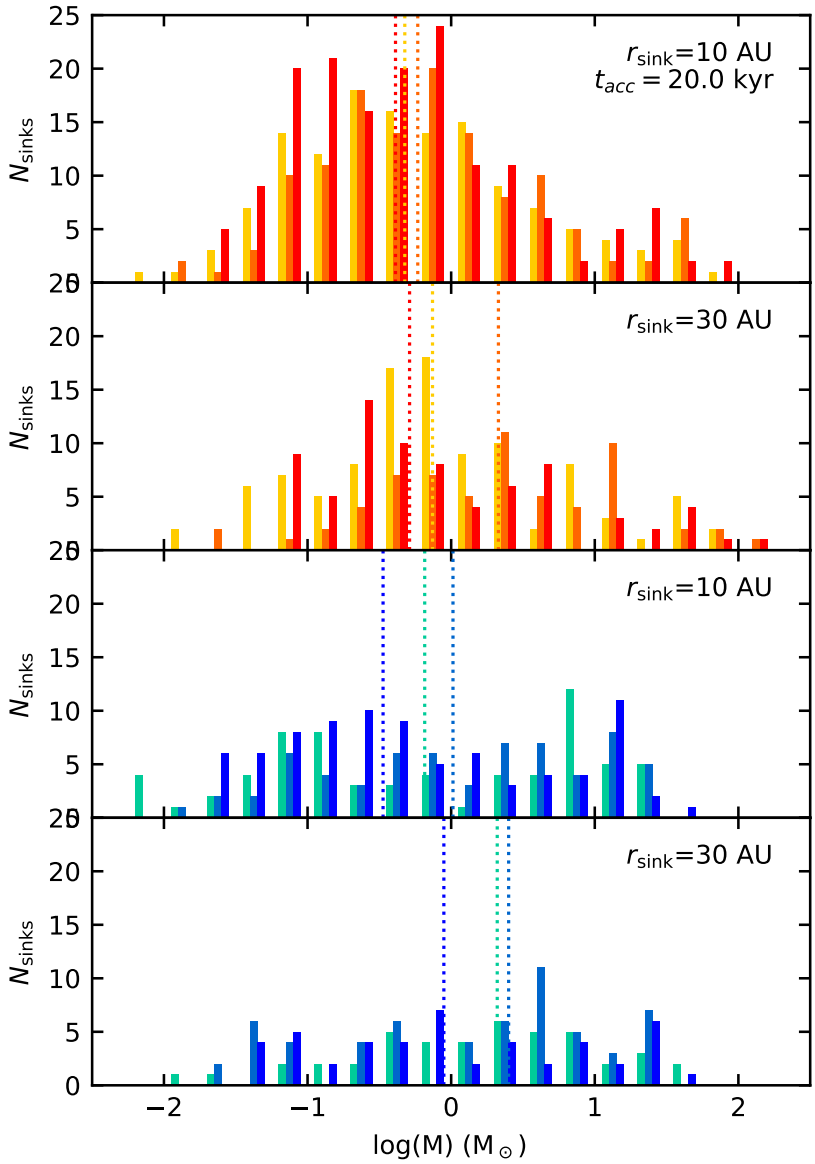

Figure 6.7: Mass distribution of sink particles in all our simulations that ran until time t_{acc}=20 kyr. The color scheme is the same as in Figure 6.6. Rows from top to bottom correspond to setups T10, T30, R10 and R30, respectively. In each panel we show the results for our three different radiation setups: NF, RTP and RTPr. The vertical dotted lines denote the median values for each distribution.

6.4.2 Radiation feedback around sinks

In this section, we analyze in more detail the environment surrounding selected sink particles. As Figure 6.7 demonstrates, most of the sinks that form in the simulations have masses $M < 10\ \mathrm{M}_\odot$ and hence do not produce a significant number of ionizing photons. We therefore focus here on the most massive sinks, which we might expect to have the greatest impact on their surroundings. Specifically, we show results for the four most massive sinks in each simulation. Moreover, we show results only for the runs with $r_{\mathrm{sink}} = 10$ or 30 AU, as the runs with $r_{\mathrm{sink}} = 2$ AU did not form any high mass sink particles by the time we ended the simulations.

Figure 6.8 summarizes the time evolution of several selected properties of the sink particles and the region surrounding them. Each column corresponds to a different simulation setup: T10, T30, R10 or R30, indicated in the label at the top. In every column we plot the results for our three different radiation setups: NF, RTP and RTPr.

The gas around the sink particles is often dynamically unstable and changes on short timescales. When sink particles pass through different environments, orbit around their binary companions or fly close to other sink particles, values such as their accretion rate or the chemical composition of the gas surrounding them can vary rapidly, making it difficult to directly compare results from different simulations in a meaningful fashion. In practice, we have found that it becomes much easier to compare the different simulations if we compare the cumulative time-weighted average values of various properties rather than their instantaneous values. These average values are computed as

$$\langle \xi \rangle = \left\{ \sum_{0}^{j=i} \xi_j \frac{(t_j - t_{j-1})}{t_i} \right\}_{i=0}^{N}, \tag{6.10}$$

where i, j and N are the indexes and a total number of simulation snapshot[2] with sink particles, respectively. The time of the snapshot is denoted as t_i and t_j (where $t_{-1} \equiv 0$) and property of interest as ξ_j. This can either be a property of the sink (e.g. its accretion rate) or of the gas surrounding the sink. In the latter case, we compute spatially averaged values within a sphere of radius $R = 200$ AU surrounding the sink particle and denote them as $\langle \xi \rangle_R$.

The first and second rows in Figure 6.8 show masses M and corresponding mean accretion rates $\langle \dot{M} \rangle$ of the selected sink particles. We see that accretion onto the sinks is more effective in the runs with high α and low β than in those with low α and high β, in agreement with the behaviour of the total accretion rate onto all sinks. There is also a tendency for the sinks with larger accretion radii to also have larger accretion rates. Furthermore, we see that in most cases, the sink accretion rate declines over time. Most of the sinks we examine here gain the majority of their mass within the first 1-2 kyr of the simulation and thereafter increase their mass only slowly with time. This behaviour is very similar regardless of whether or not we include the effects of radiative feedback, implying that it is the turbulent dynamics of the gas surrounding the sinks that largely determines how much gas they can accrete and not the radiative feedback from the sinks themselves.

[2]Even though the radiation field is updated on intervals smaller than 1 year, snapshots are produced only every 10 years.

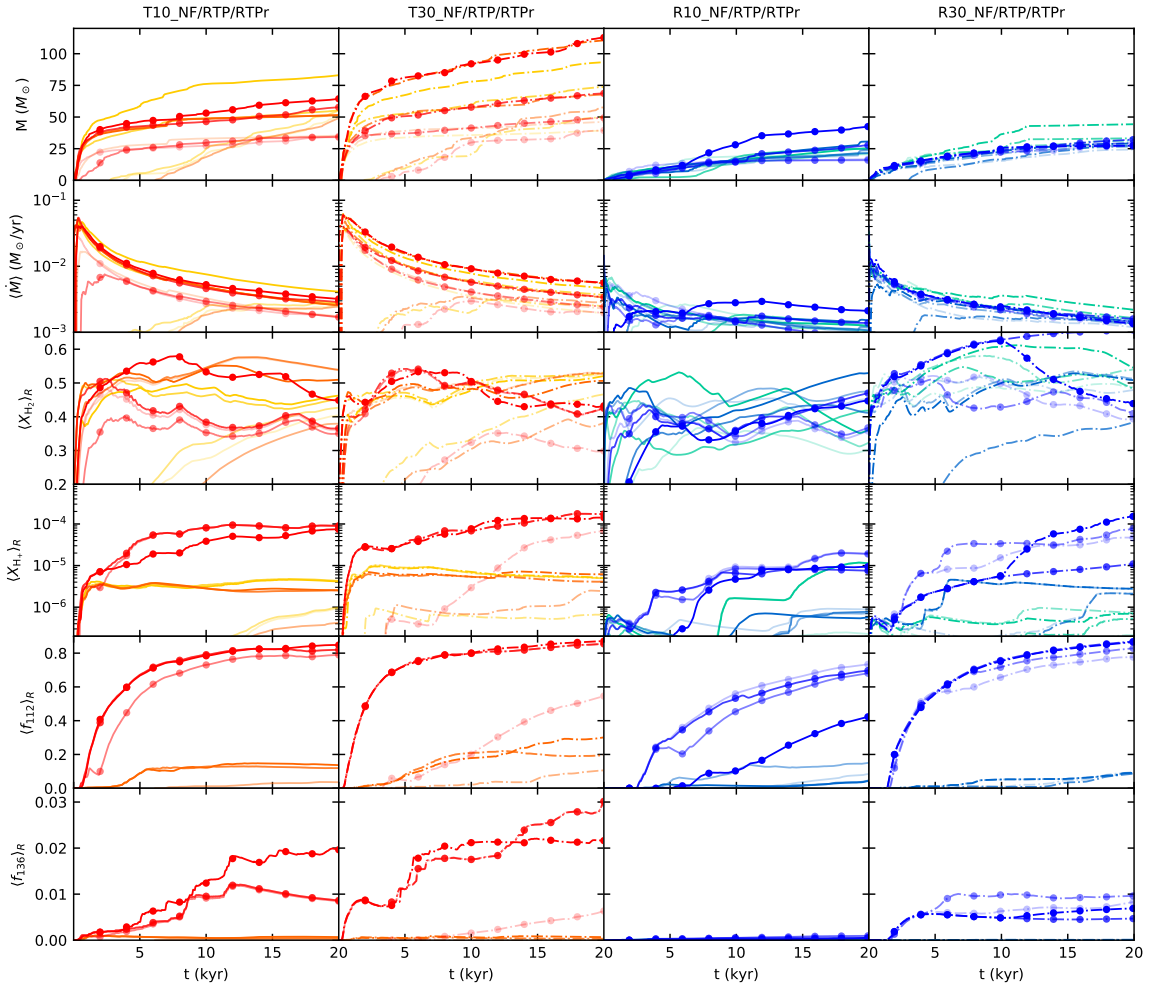

Figure 6.8: Evolution of gas properties near the four most massive sink particles in each simulation. The color scheme is the same as in Figure 6.6. Columns from left to right correspond to simulations T10, T30, R10 and R30. In each column we compare three different radiation setups: NF, RTP and RTPr. The sink particles in the same simulation are distinguished by the color intensity. Rows from the top to the bottom correspond to masses M, accretion rates $\dot{M}$, mass fractions X of H_2 and H^+ and volume filling fractions f of radiation in the 11.2+ and 13.6+ energy bins.

The third and fourth rows show the average mass fractions of molecular hydrogen $\langle X_{H_2} \rangle_R$ and ionized hydrogen $\langle X_{H^+} \rangle_R$ in the 200 AU region surrounding each sink. The mass fraction of atomic hydrogen is not shown, but is trivial to calculate since $X_H = 1 - X_{H_2} - X_{H^+}$. We see that in every case, the gas in the region surrounding each massive sink is dominated by H and H_2, with only a small amount of H^+ present. This is to be expected in the runs without radiative feedback, but we find essentially the same behaviour in the runs with radiative feedback. In other words, the ionizing radiation produced by the massive stars is unable to ionize a significant fraction of the surrounding gas. This is a key result of our study, but appears to be at odds with the results of many previous studies of ionizing feedback from Pop-III stars.

To help us understand this behaviour, we have examined the average volume filling fraction of the photons in the 11.2+ and 13.6+ bins, $\langle f_{112} \rangle_R$ and $\langle f_{136} \rangle_R$, defined as the fraction of the volume of the 200 AU sphere that contains any photons in these energy bins. These filling fractions are illustrated in the fourth and fifth rows of the Figure.[3] We see straight away that in the RTP runs, almost no ionizing radiation escapes from the immediate vicinity of the stars and only a small fraction of the volume is exposed to LW photons. On the other hand, in the RTPr runs, where absorption of radiation close to the sink is disabled, LW photons fill a large fraction of the volume of the 200 AU sphere, although ionizing photons are still confined to a relatively small volume. Taken together, these results suggest that in our fiducial RTP runs, the HII regions and PDRs surrounding the massive stars are trapped in the dense accretion disk surrounding the stars and never penetrate into the lower density gas above and below the disk. On the other hand, in the RTPr runs, the lack of absorption very close to the stars allows radiation to escape from the disk, although most of the dense gas in the disk – representing the majority of the mass in the 200 AU sphere – remains unaffected by this radiation. We will examine this interpretation of our results in more detail in the next section.

6.4.3 HII region trapping

6.4.3.1 Spatial distribution of the radiation and ionized gas

To better understand why UV photons in the RTP simulations are prevented from escaping the accretion disk, we analyze the gas properties in the immediate vicinity of some of the massive stars formed in the simulations. Specifically, we focus on the second and third most massive sink particles that form in simulation T30_RTP. As we discuss later, the behaviour of this system is representative of the behaviour we see for all of the massive stars in the RTP simulations. By the end of the simulation, these two sinks are located in a tight binary with a separation of ~ 2 AU. A similar pair of sinks with similar masses and separation is found in our T30_RTPr simulation, allowing us to directly compare the behaviour of the gas and the radiation field in both cases.

In our simulations, both massive stars in the binary emit large numbers of ionizing and photo-dissociating photons into their common environment. In principle, it would be

[3] Although not shown here, the ionizing radiation in the higher energy bins behaves in a very similar fashion to that in the 13.6+ bin.

Mass ($M_\odot$)	ID	$r_{\rm center}$ (AU)	Simulation	Age (kyr)
67.78	3	0	T30_RTP	19.78
46.17	2	2.68	T30_RTP	19.86
13.81	43	74.54	T30_RTP	5.25
5.38	46	13.9	T30_RTP	4.86
68.66	2	0	T30_RTPr	19.86
49.33	3	2.25	T30_RTPr	19.78
36.83	15	41.2	T30_RTPr	16.93
1.03	75	187.72	T30_RTPr	0.62

Table 6.3: Summary of sink particle properties around the accretion disk analyzed in Section 6.4.3. Radius $r_{\rm center}$ is measured from the most massive sink particle.

possible to examine the effects of the radiation from each star individually. However, given the small separation between the two stars, it is easier to consider their combined radiation field.

In Figure 6.9, we show plots of gas number density as a face-on projection (top row) and edge-on slice (bottom row) of a 400 by 400 AU region centred on the most massive sink in the binary system in simulations T30_RTP and T30_RTPr. Figure 6.10 shows similar plots of the temperature structure of the gas. In both Figures, we indicate the location of the binary sink particles using black crosses. For completeness, we also indicate the locations of the other sink particles present in this region. The masses, sink IDs and ages of these sinks are summarized in Table 6.3, along with their distance from the origin, $r_{\rm center}$.

From the Figures, we see immediately that the massive stars in the T30_RTP simulation are embedded in the centre of an extended accretion disk with a temperature of ~ 1000 K and a density which peaks in the centre. A disk is also present in the T30_RTPr simulation, but with a clear difference in morphology: there is a lower density cavity close to the location of the binary which is associated with a region of hot ($T \sim 10^4$ K) gas that is particularly apparent above the disk midplane.

In Figure 6.11 we plot mean radial profiles of various properties around the same sink particles in the simulations T30_RTP (left column) and T30_RTPr (right column) at time $t_{\rm acc} = 20$ kyr. We chose a set of 300 rays and distributed their orientations equally on a $r = 100$ AU sphere around the sink particle using the HEALPIX algorithm (HEALPIX) (Górski et al., 2005; Zonca et al., 2019). We then calculated the local properties of the gas along each ray. We next divided the whole solid angle into two regions according to the angle $\theta \in (0, \pi)$ measured with respect to the angular momentum vector of the accretion disk. We averaged values along rays with $\frac{\pi}{4} < \theta < \frac{3\pi}{4}$ to obtain mean values as a function of equatorial distance $r_{\rm eq}$, and did the same for rays with $\theta < \frac{\pi}{4}$ and $\frac{3\pi}{4} < \theta$ to obtain mean values as a function of polar distance $r_{\rm pol}$.

The top panels in Figure 6.11 show the mean density profile in the equatorial and polar directions in runs T30_RTP and T30_RTPr. Since the sink particles are located in a flattened disk, it is unsurprising that we find an anisotropic density distribution surrounding them. In the equatorial direction, the density first falls off rapidly from a few times 10^{13} cm^{-3} close

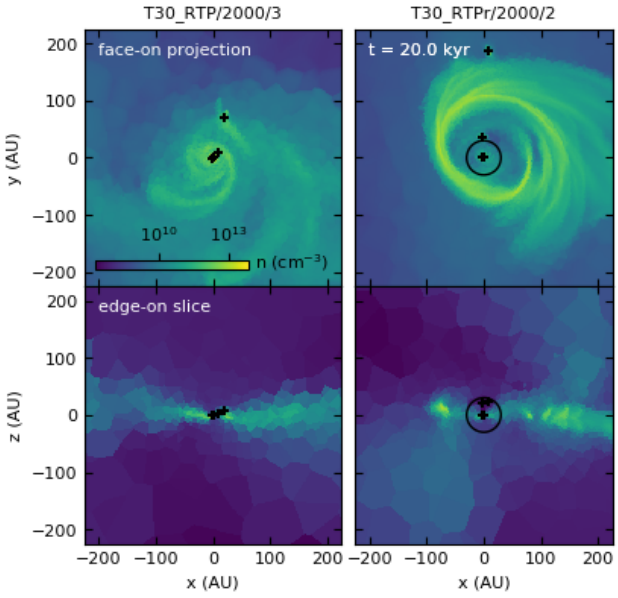

Figure 6.9: Face-on projection (top) and edge-on slices (bottom) of the gas number density around two selected sink particles (columns) at time $t_{\rm acc}$=20 kyr. In case of the projections we plot the mean column number density. Small black crosses mark the positions of the main and companion sink particles within the selected volume.

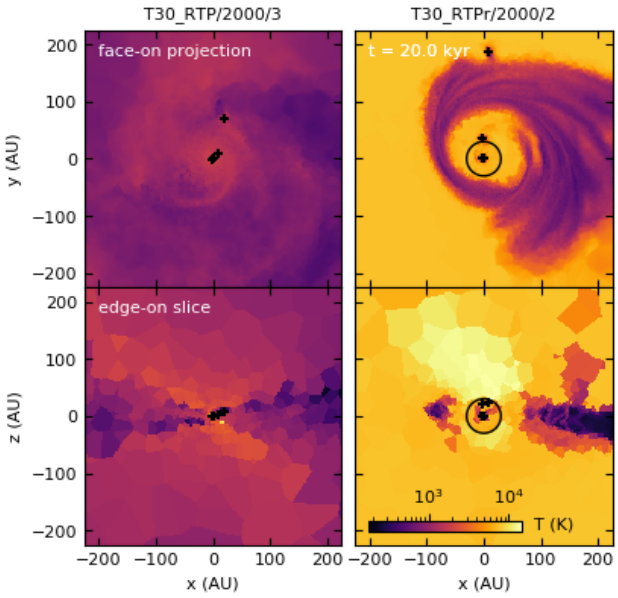

Figure 6.10: As Figure 6.9, but showing the temperature of the gas.

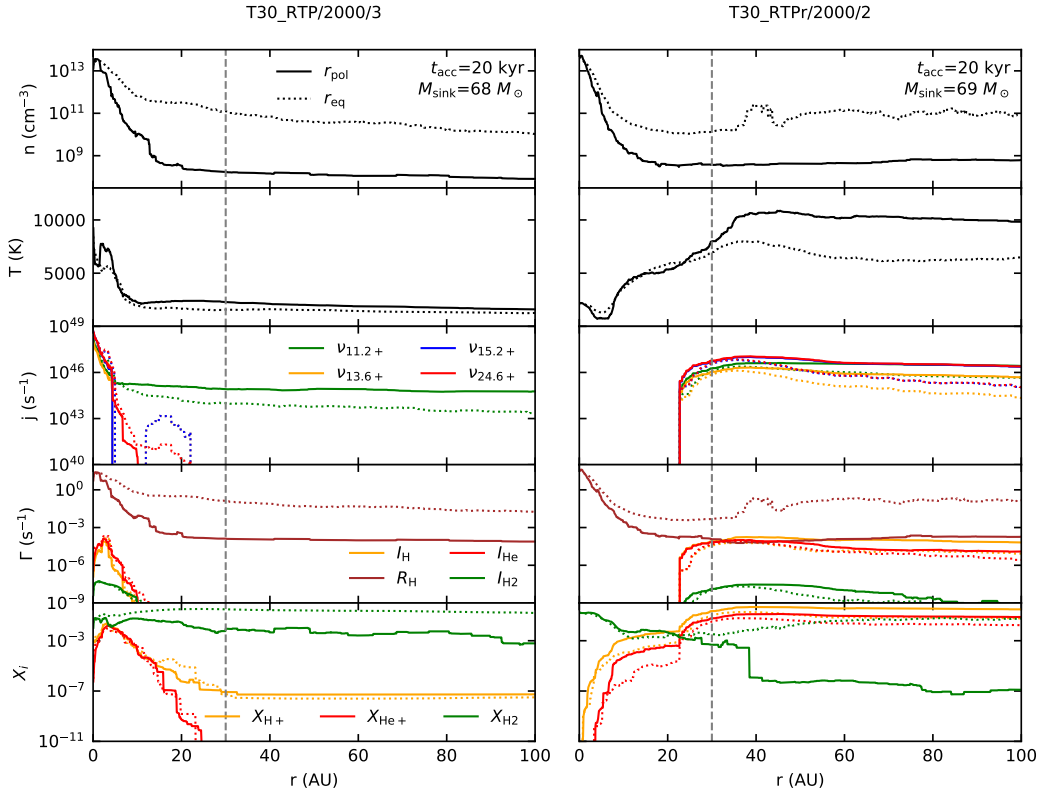

Figure 6.11: Mean polar r_{pol} and equatorial r_{eq} radial profiles around the most massive sink particles in the simulations T30_RTP (left column) and T30_RTPr (right column) at time t_{acc} = 20 kyr. We indicate the corresponding masses M_{sink} of the sink particles in the top panels. Profiles in the panels from the top to bottom show gas density, temperature, photon fluxes in all four radiation bins ($\nu_{11.2+}$, $\nu_{13.6+}$, $\nu_{15.2+}$ and $\nu_{24.6+}$), recombination R_H and ionization rates (I_H, I_{He} and I_{H_2}) and mass fractions of different gas species (X_{H^+}, X_{He^+} and X_{H_2}), respectively. Dashed grey lines denote sink accretion radii.

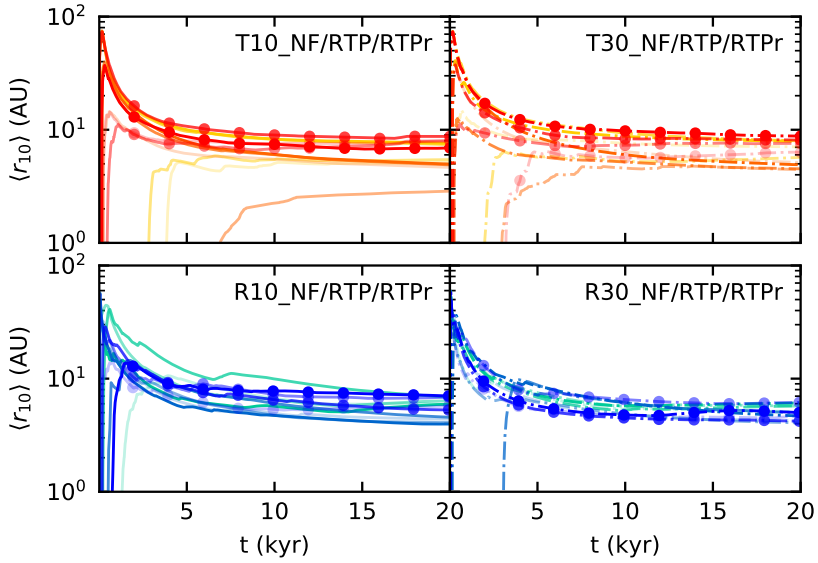

Figure 6.12: Distance of the sink particles from Figure 6.8 to the nearest cell with number density below $n = 10^{10}$ cm^{-3}. The distances are averaged in time according to Equation 6.10.

to the sink to a few times 10^{11} cm^{-3} at $r_{\rm eq} \sim 10$ AU, but thereafter decreases only slowly with increasing equatorial distance. On the other hand, in the polar direction the density decrease close to the sink is far more pronounced, with n dropping below 10^9 cm^{-3} by the time that $r_{\rm pol} = 20$ AU.

To verify that this behaviour is not simply due to the fact that we have selected some special time in the simulation, we have calculated the distance from each of our considered sinks to the nearest gas cell with density $n < 10^{10}$ cm^{-3} at various output times (We discuss this choice of density threshold in Section 6.4.3.2 below.) The results are shown in Figure 6.12. Initially, this distance – which we can take to be a reasonable proxy for the disk thickness – is large, but after only a few kyr, it settles down to a value of ~ 10 AU or smaller for most of the sinks, consistent with the behaviour we have already seen in Figure 6.11 for the most massive sinks. Importantly, this means that in our T10, R10, T30 and R30 runs, the sink accretion radius is comparable to or larger than the thickness of the accretion disk near the sinks.

Turning to the temperature structure of the gas surrounding the massive stars, we see that in run T30_RTP, there is clear evidence of radiative heating close to the star, but that once we move more than a few AU away, this vanishes and the temperature drops to the value of a few 1000 K that is characteristic of the disk even in the absence of radiative heating. In run T30_RTPr, on the other hand, the temperature rises as we move away from the sink, reaching a value of 6000–7000 K in the equatorial plane and $\sim 10^4$ K in the polar regions.

The panels in the third row in Figure 6.11 show that this difference in temperature structure is the result of a clear difference in the spatial distribution of the photon fluxes. In

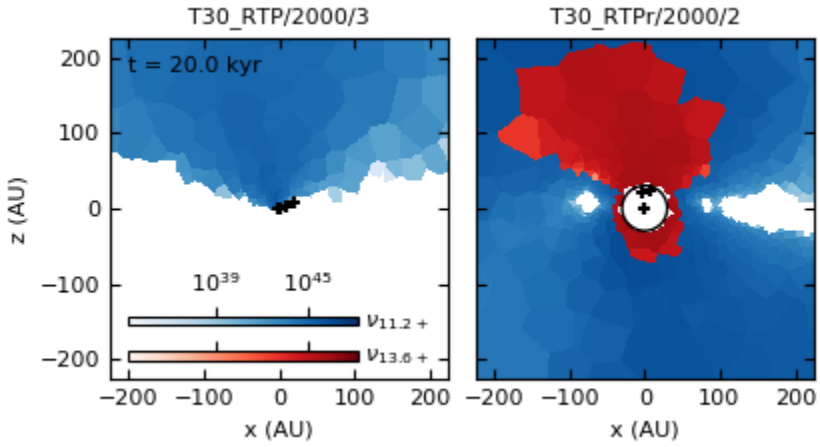

Figure 6.13: Edge-on slices of the radiation flux in the 11.2+ eV (blue) and 13.6+ eV (red) bins around the same two sinks as Figure 6.8.

run T30_RTP, radiation is emitted directly from the sink particle location and the ionizing photon flux is completely attenuated within a distance of 20 AU from the sink, with most of the attenuation occurring within the central 10 AU. Therefore, gas close to the star is heated by the radiation but the majority of the gas remains unaffected. Only the photons in the 11.2+ bin are able to escape from the immediate surroundings of the massive star. In run T30_RTPr, the behaviour of the radiation is very different. In this run, we effectively inject the photons at the accretion radius of the sink, and from there they can efficiently propagate through the surrounding gas, producing substantial radiative heating. To help us better visualize the behaviour of the radiation field in the two runs, we show in Figure 6.13 an edge-on slice of the photon fluxes in bins 11.2+ eV (blue) and 13.6+ eV (red) in each run. We overlay the two flux maps on top of each other. In both cases there is a preferential radiation outburst direction towards positive z values. However, in run RTP, only the photons in the 11.2+ eV bin escape, while in run RTPr we see significant escape of ionizing radiation, indicative of the formation of an HII region with a size of ~ 200 AU.

In the fourth row in Figure 6.11, we plot the ionization rates of H, H_2 and He, along with an estimate of the maximum recombination rate per hydrogen nucleus,

$$R_{\rm H} = \alpha_{\rm B}(T) n_{\rm H}, \tag{6.11}$$

i.e. the rate per H nucleus at which the gas would combine were it to be fully ionized. The true recombination rate is of course a factor of $\sim X^2_{\rm H^+}$ smaller than this, where $X_{\rm H^+}$ is the mass fraction of ionized hydrogen. We see that in the RTP simulation, the ionization rates of the three species close to the source are several orders of magnitude smaller than the maximum recombination rate, implying that the gas in this region should have a low fractional ionization. Far from the source, the discrepancy is even more pronounced. In the RTPr simulation, however, the ionization rate in the polar regions matches the maximum

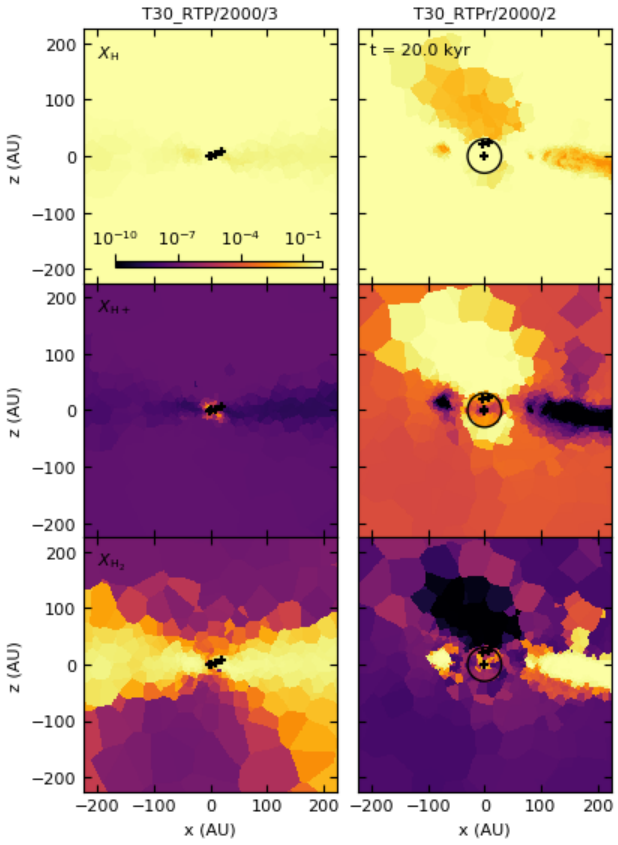

Figure 6.14: Edge-on slices of the neutral (top), ionized (middle) and molecular (bottom) hydrogen mass fractions around the same two sinks as Figure 6.8. We clipped mass fraction values in this figure into the interval $(10^{-10}, 1)$ to gain a better contrast.

recombination rate for $r_{\mathrm{pol}} > 30$ AU, i.e. as soon as we inject the ionizing photons. We would therefore expect the gas in the polar direction to be highly ionized.

Our expectations based on the ionization and recombination rates are borne out when we look at the actual spatial distributions of the ionized ($X_{\mathrm{H^+}}$ and $X_{\mathrm{He^+}}$) and molecular $X_{\mathrm{H_2}}$ gas (bottom row in Figure 6.11). In simulation T30_RTP, the fractional ionization outside of the sink accretion radius is very small and the molecular gas fraction remains comparatively high. In simulation T30_RTPr, however, dissociation of H_2 and photoionization are far more effective, leading to low H_2 mass fractions in the polar direction, coupled with a high ionized gas fraction.

Finally, we show in Figure 6.14 image slices of different hydrogen species around our chosen sink particles. A significant difference between the RTP and RTPr setups is the amount of molecular hydrogen in the accretion disk. The disk of the former is symmetric and almost entirely composed of H_2. The latter disk is disrupted, especially at the sink radius of the binary and high H_2 fractions are located only in the densest parts of the disk,

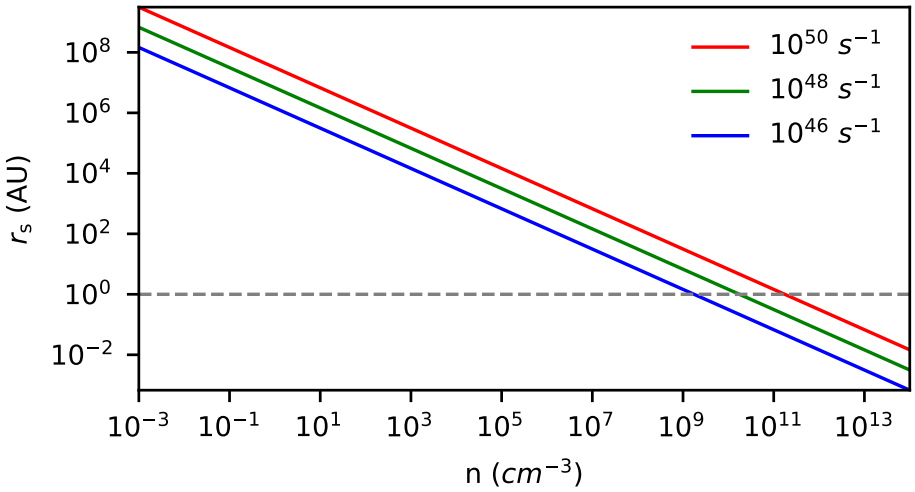

Figure 6.15: Strömgren radius r_s as a function of the number density n for three different ionization sources $\dot{Q}$ (colors lines). A grey dashed line marks the radius of the smallest resolved spherical region around the most massive sink particle.

typically the spiral arms. There is also a clear difference in the ionization state of the gas in the two runs, with run T30_RTPr showing evidence for a distinct HII region above the disk. Comparing Figure 6.14 with the temperature slice shown in Figure 6.10 and the radiation flux slice shown in Figure 6.13, we see that there is, as we would expect, a good correlation between the region with high ionizing photon flux and the hot, highly ionized gas.

6.4.3.2 Why is the HII region trapped near the stars?

The analysis presented in Section 6.4.3.1 above shows that in run T30_RTP, the ionizing photons produced by the massive binary that we examined are unable to escape from the dense accretion disk surrounding the binary. Here, we examine with the aid of some simple quantitative models why this is the case.

A simple starting point is the Strömgren radius. A point source of radiation emitting $\dot{Q}$ ionizing photons per second embedded in uniform density hydrogen[4] with number density $n_{\rm H,0}$ will rapidly produce an HII region with radius

$$r_{\rm s} = \left(\frac{3\dot{Q}}{4\pi\alpha_{\rm B} n_{\rm H,0}^2} \right)^{1/3}, \tag{6.12}$$

where $\alpha_{\rm B}$ is the case-B recombination coefficient. The time taken for an HII region to reach this radius is approximately given by the recombination time $t_{\rm rec} = (n_{\rm H,0}\alpha_{\rm B})^{-1}$, which is of the order of a few years or less in the dense gas close to the massive stars formed in

[4]The inclusion of helium changes $r_{\rm s}$ by only a small amount.

our simulation. Figure 6.15 shows how r_s evolves with density for $\dot{Q} = 10^{46}$, 10^{48} and 10^{50} photons s^{-1}. We see that even for $\dot{Q} = 10^{50}$ s^{-1} – corresponding to the number of ionizing photons emitted by a 120 M$_\odot$ Schaerer (2002) – the Strömgren radius becomes smaller than an AU for number densities $n > 10^{11}$ cm^{-3}, characteristic of the gas in the accretion disk surrounding our massive stars. Therefore, in the dense environment of the disk, we expect the initial size of the HII region to be smaller than the scale height of the accretion disk.

The gas in the HII region has an equilibrium temperature of $\sim 10^4$ K and hence is over-pressured compared to the surrounding gas. If the gravitational attraction of the central ionizing source can be neglected, it is easy to show that this elevated pressure will drive the hydrodynamical expansion of the HII region, leading to a power-law dependence of the HII region size on time in the case of approximately uniform gas (Spitzer, 1978a; Hosokawa and Inutsuka, 2006b) or a so-called champagne flow in the case of a steeply stratified density distribution (see e.g. Franco et al., 1990; Shu et al., 2002). Close to the star, however, its gravitational attraction cannot be neglected and the HII region can expand hydrodynamically only if the sound speed of the ionized gas exceeds the escape velocity associated with the gravitational field of the star (Keto, 2002). In our example case of a massive binary, the escape velocity of the larger of the two stars is given by

$$v_{\rm esc} = \left(\frac{2GM_*}{r}\right)^{1/2} \simeq 350\,{\rm km\,s^{-1}} \left(\frac{M_*}{68\,{\rm M_\odot}}\right)^{1/2} \left(\frac{1\,{\rm AU}}{r}\right)^{1/2}, \tag{6.13}$$

where r is the distance from the star and where the first term in brackets is of order unity. This becomes comparable to the ionized gas sound speed only at distances $r \gg 100$ AU, considerably larger than the initial Strömgren radius. Therefore, thermal pressure is unable to expand the HII region significantly beyond its initial size.

Finally, we must consider the effects of radiation pressure. In the top panel of Figure 6.16, we plot spherically-averaged radial profiles of gas density (blue) and the enclosed gas mass (orange) around the sink particle with ID 3 in the simulation T30_RTP at time 20 kyr. In the bottom panel of the Figure, we compare the gravitational acceleration at various distances from the star with the acceleration resulting from the absorption of ionizing photons. We compute the gravitational acceleration following

$$a_{\rm G} = \int_0^r \frac{G\rho(r)}{r^2} 4\pi r^2 dr + \frac{GM_*}{r^2}, \tag{6.14}$$

where $\rho(r)$ is the spherically-averaged radial density function of the gas, G is the gravitational constant and M_* is the mass of the star. To highlight the influence of the stellar gravity, we show profiles for three different values of the central stellar mass ($M_* = 1, 20, 40\ M_\odot$), plus one case where the star is absent. We see that on scales smaller than a few tens of AU, the acceleration is dominated by the contribution from the star even for relatively small stellar masses.

The dashed lines in the Figure 6.16 show the radiative acceleration, calculated according to the following equation

$$a_\gamma = \dot{Q}\frac{E_\gamma}{c}\left(\int_0^r \rho(r) 4\pi r^2 dr\right)^{-1} \tag{6.15}$$

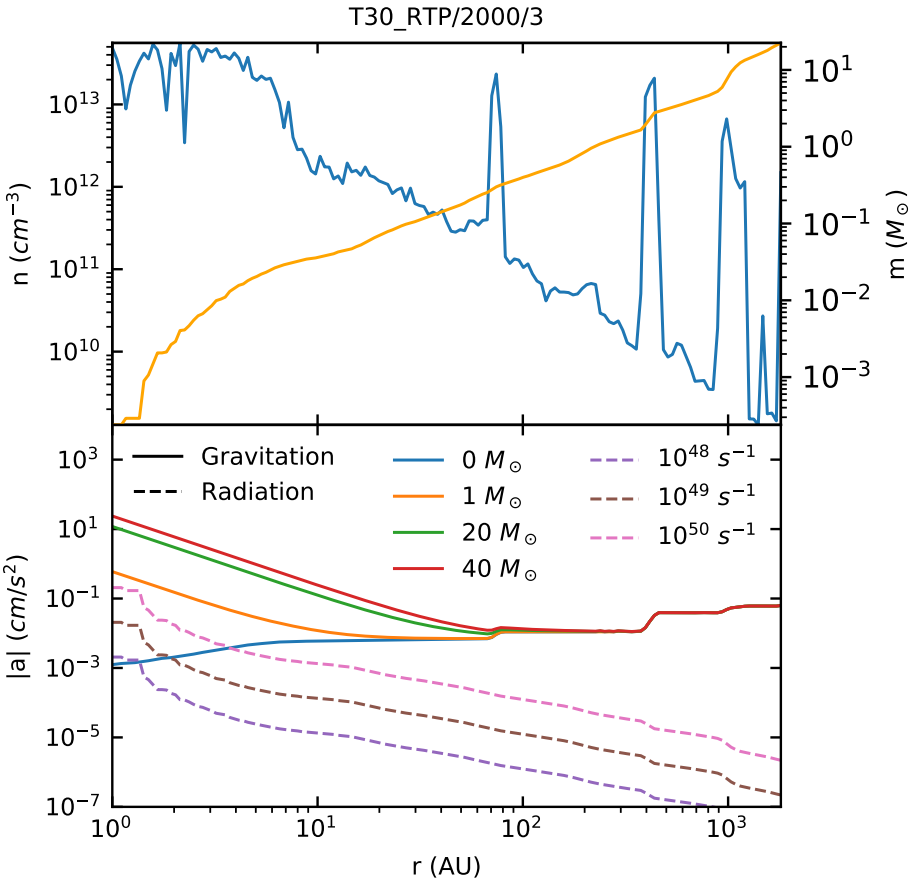

Figure 6.16: The top panel shows spherically averaged number density (blue) and enclosed mass (orange) as a function of the distance from the sink particle 3 in the simulation T30_RTP at time 20 kyr. The bottom panel shows absolute values of corresponding gravitational acceleration (solid lines), and acceleration caused by photon ionization per hydrogen atom (dashed line).

where E_γ is the mean energy of the ionizing photons. We assume here that the force is distributed uniformly amongst all of the particles enclosed within the given radius. Strictly speaking, this is not true: the force acting on a given parcel of gas within the HII region depends on its recombination rate and hence will be higher in denser gas. However, by making this approximation, we attempt to account for the fact that ionized gas that does feel a stronger force will interact with and transfer momentum to the surrounding ionized gas. We show results for three different ionizing photon production rates, $\dot{Q} = 10^{48}, 10^{49}, 10^{50}$ photons per second and a mean photon energy $E_\gamma = 15$ eV. As seen from the plot, the radiative acceleration is highest close to the star and drops strongly with increasing distance. It exceeds the gravitational acceleration only in the case where $M_* = 0$, i.e. when we do not account for the gravity of the star producing the ionizing photons. In the more realistic case where $M_* > 10\,\mathrm{M}_\odot$, we see that even at 1 AU, the gravitational acceleration exceeds the radiative acceleration by more than two orders of magnitude. We can therefore safely conclude that radiation pressure will also be unable to drive the hydrodynamical expansion of the HII region, which therefore remains trapped in the dense accretion disk.

To summarize: the high gas density in the accretion disk surrounding the massive stars limits the initial size of the Strömgren radius to < 1 AU. This close to the star, its gravitational attraction is stronger than the forces acting on the gas due to thermal pressure or radiation pressure, and so the HII region is unable to expand hydrodynamically and instead remains trapped in the disk.

6.4.4 Comparison of all sink particles

Number of sink particles in all our simulation is relatively large. Instead of doing a detail analysis of their environment as in the previous section, we will compare and correlate some of their properties. From these values we will generalize conditions favourable for HII region formation in our simulations.

Figure 6.17 is a correlation matrix between five sink particle properties at the final time $t_{\mathrm{acc}} = 20$ kyr. Columns from the right to the left show sink mass M, gas number density at its location, emission rate of the ionizing radiation $\nu_{13.6+}$, distance to the nearest sink particle d_{ngb} and maximum radius[5] of its HII region $r_{\mathrm{H+}}$, respectively. The diagonal plots show corresponding histograms.

The most prominent group of sink particles on the plots are those which escape from the central star forming region. They have sub-solar masses, low emission of ionizing photon ($\nu_{13.6+} < 37.5\ \mathrm{s}^{-1}$) and occupy low density regions ($n < 10^{10}\ \mathrm{cm}^{-3}$) with a very low refinement. In these regions all linear properties strongly correlate with the cell sizes. We report only three medium size ($M \approx 10\ M_\odot$, light blue dots) ejected sink particles that create significant ($r_{\mathrm{H+}} > 1000$ AU) HII regions. Transition regions with gas number densities between $10^8 - 10^{12}\ \mathrm{cm}^{-3}$ are only sparsely populated.

Mass histogram shows the similar mass distribution as in the Figure 6.7. Turbulent simulations with the smaller accretion radius T10 produce large amounts of low massive

[5] We calculated maximum radius $r_{\mathrm{H+}}$ using the HEALPIX rays previously mentioned in section 6.4.3. Instead of ray averaging, we searched for a ray with the longest continuous radial $r_{\mathrm{H+}}$ profile of H+ and took the value. Note that the values of $r_{\mathrm{H+}}$ in Figure 6.17 are instantaneous. Their time-averaged values may differ.

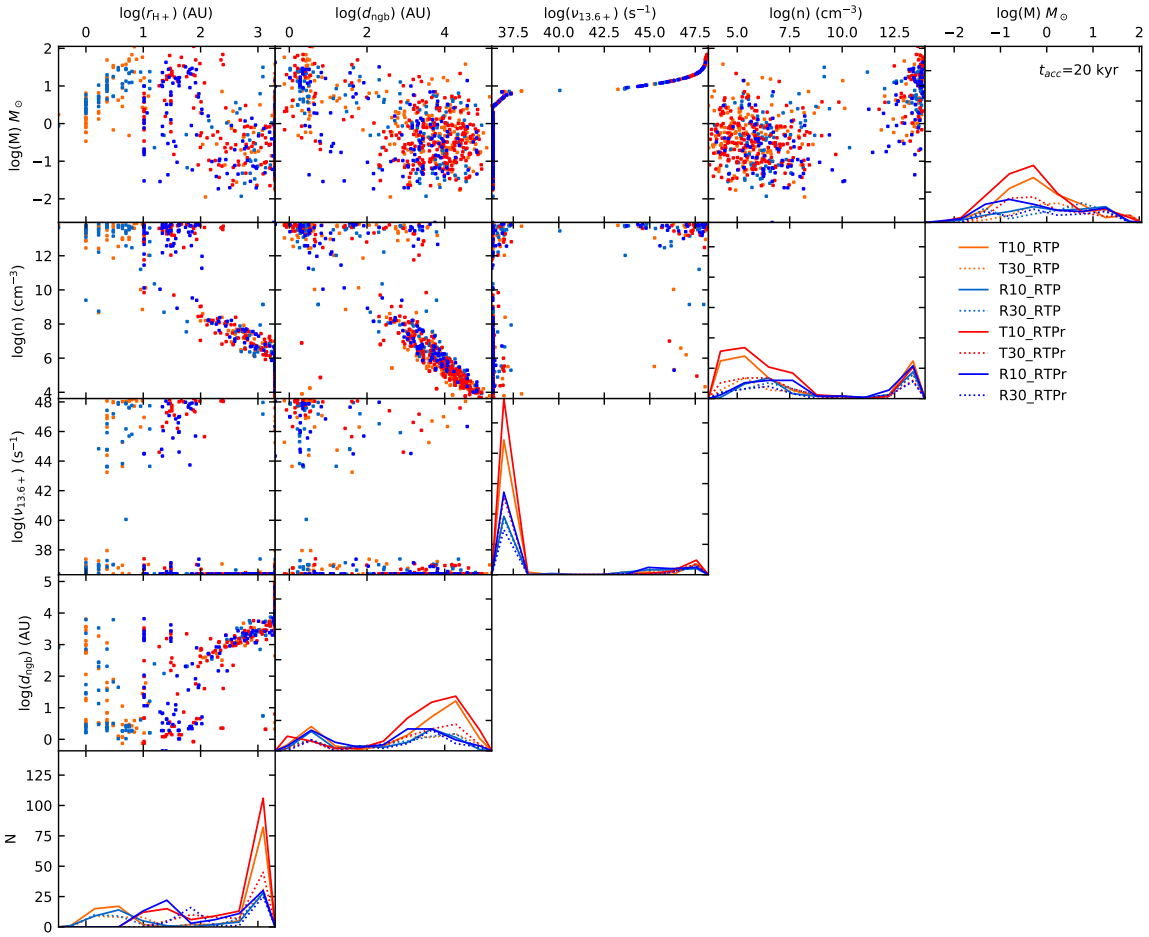

Figure 6.17: Correlation matrix of sink particle masses M, emission rates $\nu_{13.6+}$, distances to the nearest neighbors $d_{\rm ngb}$, maximum radii of their HII regions $r_{\rm H+}$ and gas densities n at the sink locations. We plot corresponding histograms (with 10 bins) of the properties on the diagonal. The color scheme corresponds to the Figure 6.6.

stars. Simulation T30 has sink particles with masses $M \approx 100\ M_\odot$. Rotational initial conditions (R10 and R30) result in flatter mass spectrum with not as high masses.

The choice of our stellar spectrum model, that depends on the sink mass and mass accretion, prescribes behaviour of the sink photon emission. Sink particle in the dense regions have super-solar masses and photon emission up to $\nu_{13.6+} \approx 10^{48}$ photons per second. Despite of their high emission rate, only a few of them produce HII regions larger that few hundreds of AU. Among them are the sink particles discussed in the Section 6.4.3.

Distances of the nearest neighbor sink particles correlate with the gas number density and have two main peaks. Sink particles in the densest regions are only few AU from each other and form binary or multiple stellar systems. In contrast, collisions eject the low massive sink particles more than 10^4 AU away and separate them from the central star-forming regions.

Some sink particles in the leftmost column in the Figure 6.17 follow vertical lines. For the RTP simulations, these radii reveal our actual cell resolution ($r_{\mathrm{cell}} \approx 1$ AU). In case of the RTPr simulations, the lines correspond to the sink accretion radii (r_{sink}=10 and 30 AU) from which we attenuate photons. The corresponding histogram is also biased by two effects related to our simulation setup. At small radii we can notice the starting radii of the photon attenuation. High radii are saturated by the cell resolution in the low density regions. The most important difference is visible in simulation T30_RTPr where the three (red color) high massive sink particles produce HII regions with $r_{\mathrm{H+}} > 100$ AU. In this case photon can escape their accretion disk easier, because we start their attenuation from the sink accretion radius.

One can conclude from the above analysis that the majority of the stars in our simulations cannot produce and maintain significantly large HII regions. Ejected sink particles have sub-solar masses and low gas accretion rates outside the star-forming region stop their accretion. Subsequently, they produce only a small amount of radiation. In contrast, high mass stars are located in high density regions where recombination rates and gravitational fields compete with the ionization rates and ionization pressure.

From our data, we report two scenarios that lead to growth of HII regions. In the first case, radiation from stars with masses above 50 $M_\odot$ in RTPr simulations disturb the accretion disk and clear the way for ionizing photons. We follow evolution of the sink particles only until 20 kyr from their birth and we expect that the amount of radiation would increase even more in later times. In the second case, stars with masses above 10 $M_\odot$ escape the central region and develop HII regions in the low density environment.

6.5 Discussion

One of the primary goals of this chapter was to study radiation feedback in the collapsing primordial mini-halos and determining its impact on the Population III stars initial mass function. We prepared a set of simulations where the gas of the collapsing Bonnor-Ebert sphere was dominated either by a turbulent (T) or rotational (R) velocity field. We ran these simulations without radiation feedback (NF), with a radiation field directly from the sink particle location (RTP) and the accretion radius (RTPr). Besides that, we studied two sink particle radii: 10 and 30 AU.

This section discusses results got from our simulations and caveats of our model. We also discuss radiation models used in the previous literature.

6.5.1 Radiation feedback of Population III stars

In Section 6.4.3 we discussed differences between the two simulation setups RTP and RTPr. We found that if we attenuate photons directly from the sink particle location, the radiation is being trapped within the accretion disk. However, if the radiation is calculated from an accretion radius, it can disturb the accretion disk and ionizing photons escape from an HII region. Only simulation T30_RTPr produced sink particle massive enough to create decent HII regions. Even these are not as large as reported in the previous literature. Other simulation setups result in significantly lower star masses and only negligible HII regions. All four panels in Figure 6.7 show the same trend. The RTP case results in more massive stars, whereas RTPr produces more low massive stars. In the first case, the ionization stays contained within the disk. In the second case escaping photons deploy more momentum into the surrounding environment, drive more turbulence and further accretion disk fragmentation.

Since the ionization heating and ionization pressure near the source in RTP simulations is not strong enough to disturb accretion disk, we might miss an additional physics such as jets or magnetic fields. These could additionally help photons to break through the accretion disk and open low-density channels through which radiation can escape. Our simulation setup uses an idealized spherical model of a collapsing mini-halo. For more realistic results we will have to use zoom-in initial conditions from the cosmological simulations.

6.5.2 Caveats

Radiation transfer at gas densities $n > 10^{10}$ cm^{-3} puts high demands on spatial and temporal resolution of simulations. In this section, we summarize our findings and caveats of our model regarding resolution constrains.

Construction of the full Voronoi mesh in Arepo determines the lower timestep limit of our radiation model. In the SPRAI-II in Chapter 5 we described necessary approximations in cases where recombination times in the gas are smaller than this threshold. At our present grid resolution $r_{\rm cell} \approx 1$ AU, exact physical calculations of radiation transfer require at least two orders lower time steps. The approximation described in the SPRAI-II (Section 5.2.2) guarantees that the code attenuates photons at the correct radii even if the number of gas species is much smaller than the number of recombinations.

Small dynamical times of the self-gravitating gas with density above certain threshold requires usage of sink particles with a certain accretion radius. However, the constant accretion radius of a sink particle is at these densities still around 2 orders higher than the radius of the HII region (Section 6.4.3.2). It is therefore computationally not feasible to directly simulate detail HII expansion and resolve individual Strömgren radii. Such extreme conditions require the usage of sub-grid models. We will discuss models used in other literature in the following section.

Author	Star	$r_{\rm sink}$ (AU)	$n_{\rm cell}^{\rm max}$ (cm^{-3})	$N_{\rm src}$	Resolution
Hosokawa et al. (2011)	grid cell	10	10^{12}	1	6-12 AU
Stacy et al. (2012)	SPH sink	50	10^{12}	1	0.72 $M_\odot$
Susa (2013)	SPH sink	30	3×10^{13}	5-10	0.496 $M_\odot$
Susa et al. (2014)	SPH sink	30	3×10^{13}	1-6	0.5 $M_\odot$
Stacy et al. (2016)	SPH sink	1	10^{16}	1	3×10^{-2} $M_\odot$
Hosokawa et al. (2016)	sink	30,52	$10^{13} - 10^{14}$	1	3.1-3.6 AU
Sugimura et al. (2020)	sink	64	2×10^{11}	1-8	4 AU
This study	sink	2/10/30	7.2×10^{13}	40-150	0.5-1 AU

Table 6.4: List of the simulations that include radiation from Pop-III stars. $N_{\rm src}$ denotes number of radiation sources, $r_{\rm sink}$ is a sink radius and $n_{\rm cell}^{\rm max}$ is the maximum resolved number density. Resolution for grid codes is given in cell sizes, whereas for SPH codes, we show the best mass resolutions $M_{\rm res}$.

In our simulations, we start attenuation of photons and injection of radiation pressure either from the source cell (RTP cases) or from the sink accretion radius (RTPr cases). The amount of escaping ionization (Figure 6.11) and structure of the accretion disk (Figure 6.14) in the two cases differ significantly (For comparison see also bottom panels in Figure 6.8). Our results show that the choice of the sink particle radius directly influences the amount of escaping ionization and final results.

Complex systems with many stars put additional constraints on the resolution. Especially simulations with turbulent initial conditions produce large amounts of sink particles with sub-solar masses that are ejected to the low-density environment. Their emission rates are usually below $\nu_{13.6+} < 10^{37}$ photons per second and resulting HII regions are smaller than the sizes of the de-refined gas cells (Figure 6.17). Maintaining a proper resolution for a large amount of ejected sinks may put an overhead on the simulation resolution. Since we focused only on the most massive stars in the central region, we did not take this into an account.

Finally, we attribute large numbers of low-massive stars in our results to the fact that our sink particle model does not include particle merging. From the nearest neighbor $d_{\rm ngb}$ plots in Figure 6.17 we showed that some sink particles are as close to each other as several AU. We expect that their mergers result in stars with much higher masses, photon emissions and a smaller number of ejected stars. For more detail study of possible merges in similar setups refer to the paper of Wollenberg et al. (2019).

6.5.3 Radiation models used in the literature

Self-consistent simulations of accretion disk fragmentation in combination with the radiation transfer from each star are computationally expensive. Previous studies of the Pop-III star formation include several setups that focus only on the central accreting star.

In the Table 6.4 we summarize the most recent simulations with the radiation feedback in the context of Pop-III formation. The three most recent studies of the radiation feedback from Pop-III stars do not take into account the detail structure of accretion disks and include radiation only from the central stars. In comparison, our model simulates radiation from all

stars.

The study of Hosokawa et al. (2016) calculates ionization from the accretion radius of the sink particle $r_{\rm sink}$ = 30 AU and Sugimura et al. (2020) even higher, 64 AU. Both radii are bigger than the actual accretion disk in our simulation (10 AU). In this case, the radiation skips the small structure of the accretion disk and high recombination rates of the dense gas. In our results, we demonstrated that the amount of radiation that escapes the main star depends on the choice of the sink radius.

In the second case (Stacy et al., 2016) the authors take into account a sub-grid model that is supposed to be valid for the regions of an order of 200 AU. Instead of using the SPH-density derived from the simulation they use in the central region densities calculated from the self-similar champagne flow solution (Franco et al., 1990; Shu et al., 2002). This model, however, does not include into account the gravitation of a central star. Further discussion of this problem is given in Section 6.4.3.2.

Our study and both examples above lead us to a conclusion, that proper treatment of the radiation around young Pop-III stars require better resolution of the accretion disks. Using a sub-grid model that ignores high densities around the star may lead to overestimation of the amount of radiation and onset of the feedback in the mini-halos.

6.6 Summary

In this chapter we studied a set of simulations of the collapsing Bonnor-Ebert sphere. The initial settings of the gas cloud had either dominant rotational or turbulent velocity fields. When the gas density reached star-formation threshold $n_{\rm th}$ we introduced sink particles that starts accreting gas within its radius $r_{\rm sink} = \{2, 10, 30\}$ AU. For each combination of the initial settings we ran a simulation without radiation feedback, with radiation feedback directly from the sink particle location and from the accretion radius. We summarize the results of our simulations into the following points:

- A combination of the turbulent initial conditions and radiation is favourable for formation of small Pop-III stars. They are subsequently ejected away from the halo. These low massive stars could survive into later times.
- Radiation feedback from all stars in the system might lead to higher turbulence of the gas and subsequent production of more low-mass stars.
- Study of the mass accretion of the Pop-III stars at high resolutions gives a quantitatively different view on the role of the radiation during accretion stage. High recombination rates of the gas trap ionizing photons inside the the accretion disks. Only H_2 dissociating radiation can escape to the surrounding environment.
- Higher spatial resolution than that used in the previous literature (Stacy et al., 2016; Hosokawa et al., 2016; Sugimura et al., 2020) is needed to model physically realistic photon outflows from the stars in the minihalos. In the first case the accretion radius of the sink particle ($r_{\rm sink}$=30 AU) is actually bigger than the actual accretion disk in our simulation (~10 AU), and in the second case the authors take into account a sub-grid

model that is supposed to be valid for the regions of an order of ∼100 AU. The sink radius in the third case (64 AU) is double the size than in our worst case (30 AU) and threshold densities for sink particles ($\sim 10^{11}$ cm^{-3}) are two orders lower than in our simulations.

- Future work needs to include other types of feedback besides the radiation heating and radiation pressure, that can help to disturb the high density accretion disks and allow radiation to escape. We assume that the magnetic fields could give rise to jet outflows and thus increase the opacity of the accretion disk.

In our future work, we need to address several additional effects that we did not include in this work and need more technical development. First, we need to implement sink particle merging. Our current simulations produce a large amount of sub-solar stars that escape from the central region via collisions with their massive neighbors. Correct treatment of the star collisions might decrease this trend.

The second physical aspect that we want to explore is formation of magnetic jets around the star. We showed that dense accretion disks around the newly formed stars can be up to 10 AU thick. Photoionization and radiation pressure alone are not sufficient to disrupt these disks and end accretion. Formation of jets could help to disturb the disk and to create outflow channels for the star radiation.

7 Conclusions

In this thesis, we utilized a novel radiation transfer technique called SIMPLEX to study complex ionization and dissociation processes in a first-star formation. These stars emerged around 400 million years after the Big Bang, and this epoch in the early Universe provides only a small amount of direct observational data. Therefore, our study has to rely mostly on theoretical predictions and numerical simulations. The importance of this work and radiation transfer code SIMPLEX lies in the fact that it enabled us to study the radiation feedback from the first stars in a high resolution. Our 3D simulations resolve the formation and fragmentation of their accretion disk. At the same time, we followed the onset of the radiation directly from all the stars within the simulated volume. Our results give us a new perspective on previous expectations, namely that the ionizing radiation from the first stars can easily escape from their accretion disks and shut down further accretion. We divide results in the following summary into two parts according to their methodological and scientific significance.

7.1 Summary

The methodological part of this work describes the SIMPLEX method and its implementation as a radiation transfer code SPRAI in the hydrodynamic code AREPO. Its exceptional performance in calculations of the multi-source radiation, discussed in Section 4.3.5, was the primary motivation why we adopted it in our Pop-III simulations. Secondly, this method calculates photon attenuation on the unstructured Voronoi mesh (see Section 4.2.1). Since SIMPLEX can use the same Voronoi mesh that is already employed by the hydro-solver, it is an excellent match for the framework of the AREPO.

Previous, standalone, version of this method (Paardekooper et al., 2010) was restricted only for use in post-processing of the simulation data. Therefore, we could not use it to simulate a self-consistent interaction between radiation and gas dynamics. This interaction is, in many astrophysical processes, principal source of feedback and we cannot neglect it. At the same time, the original SIMPLEX method missed the capability to do calculations on high-performance computing systems, and thus to handle more extensive data. SPRAI implementation successfully overcomes both of these restrictions.

Using a combination of SIMPLEX radiation and variable timestep hydrodynamics of AREPO resulted in some additional restrictions. We discuss these further in Chapters 4 and 5. By design, AREPO calculates the full Voronoi mesh only on every full hydro-steps (see Figure 4.1). This scheme optimizes the computational costs of the code, but at the same time imposes an upper limit for the updates of the radiation field. Since AREPO calculates chemical network on every hydro-step, we have to rely on the fixed radiation field in chemistry solver during all sub-steps.

In Section 4.2.2, we discuss conditions for the radiation transfer near the photon sources where the ionization is especially strong and gas is ionized almost instantly. Frequent updates of the radiation field become even more important in the cases where the recombination in high dense regions becomes dominant. In Section 5.2.2, we introduce an approximation that allows us to solve this problem even though the update of the radiation field is not sufficiently high for the convergence of the chemistry module (see the Figure 5.2). In this case, we have to estimate the number of recombined photons and additionally subtract them from the photon field.

SIMPLEX method is also prone to produce inhomogeneous radiation fields far from the sources. This effect increases together with the number of Voronoi cells that rays pass on their way from the source. In Section 4.2.4, we show that this inhomogeneity can be suppressed either by increasing the number of directional bins or by the integration of the sufficient number of radiation field realizations.

Nevertheless, the restrictions mentioned above do not prevent us from using SPRAI as a self-consistent method to study the primordial Universe. We show on several examples and resolutions that it performs well in standard test problems of the R-type (Sections 4.3.1 and 5.3.1.1) and D-type (Sections 4.3.2 and 5.3.1.2) I-fronts. The ionization correctly captures shadows behind the dense gas obstacles (Section 4.3.4) and has a correct behaviour in the regions with strong density gradients (Section 4.3.3). Our scheme also includes multi-frequency treatment of ionizing and dissociating radiation, as described in Sections 5.2.3 and 5.3.2. Finally, in Sections 5.2.4 and 5.3.3, we discuss its capability to capture the effects of the direct pressure from ionizing radiation.

The above results and necessary approximations underline the fact that a proper treatment of the radiation in numerical simulations has to be carefully evaluated both on temporal and spatial scales. Discretization of otherwise continuous radiation transfer stays still a big challenge for computational physics, and even the best algorithms may have many restrictions. Even though SPRAI implementation was one of those cases, it is capable of producing exciting results that we describe further in the text below.

The scientific part of this work presents our model of the first-star formation. In Section 6.2, we describe numerical methods. The gas in the simulation follows the primordial chemistry network (Section 6.2.1), and we model individual stars by the sink particles (Section 6.2.2) with three different accretion radii: 2, 10 and 30 AU. Spectral emission from the sink particles (Section 6.2.3) depends on their mass and accretion rates, and we calculate the number of photons in each frequency bin using the black body spectrum. SPRAI radiation transfer subsequently evolves photons emitted from all sink particles in the simulated volume. For every set of initial conditions, we evolve the system without (NF) and with radiation. The later additionally divide on the cases when radiation comes directly from the source cell (RTP) and the cases when it starts at the sink particle radius (RTPr).

In the simulations, we follow the collapse of the primordial gas cloud in the central regions of the minihalo. Initial conditions (Section 6.3) use an idealized isothermal gas cloud with the radial profile of the Bonnor-Ebert sphere. This choice allowed us to test gas clouds with initial rotational (R) and turbulent (T) velocity fields. We evolve the gas collapse until the

first stars form in the densest regions (Figure 6.3). Subsequently, we cut out the central four parsecs region of the simulation around the star-forming area, continue the simulation for the next 20 kyrs, and simulate radiation feedback from individual stars.

Figures 6.6 and 6.7 summarize the final mass distribution and number of sink particles in all simulations. The second figure also shows trends of the median masses in the three different radiation setups. Masses of the sink particles in RTP simulations, where radiation evolves directly from the sink particle cell, have higher medians than those in the NF. In the RTPr case, we observe the opposite trend. Radiated photons escape further from the stars, introduce additional turbulence to the gas, and increase the number of disk fragments. We could further improve the values of these trends by evolving our simulation to later times or test multiple seeds for our initial velocity fields. Nevertheless, present results lead us to the conclusion that the ionizing radiation does not seem to have as high effect on the final distribution of stellar masses in our simulations as we initially thought.

We discuss this interesting fact in Section 6.4.2. In Figure 6.8, we show the time evolution of the four most massive sink particles from each simulation and gas around them. In the last two rows in the same figure, we plot the average volume fraction of the LW and ionizing radiation as a function of the time. Radiation manages to escape further from the sink particle in RTPr case. However, the amount of the radiation flux in the RTP case is significantly lower.

Section 6.4.3 analyze this problem on an example of one sink particle binary form the simulations that result in the highest photon escape fraction at the final time. In Section 6.4.3.1, we discuss detail gas properties in and around their accretion disk in both radiation setups, RTP and RTPr. Particularly, Figure 6.11 lead us to the fact that if the radiation source is embedded within the dense accretion disk, the ionizing radiation becomes trapped. We attribute this to the combined effects of the unresolved HII region and extremely high recombination rates in the dense accretion disk (Section 6.4.3.2).

In previous literature, the ionization from the first stars was supposed to escape the accretion disks and, in later time, shut off the accretion of the gas on the Pop-III star. However, these studies did not have enough resolution to resolve the detailed structure of the accretion disk around the newly formed stars (Sections 6.4.3.2 and 6.5.3). Our main conclusions from the scientific part of this work are summarized in points in Section 6.6.

This analysis challenges the role of the radiation feedback from the Pop-III stars and urge us to further study the ionization processes in the accretion disks. Our results provide high resolution in the most dense regions around the stars. Nevertheless, we still need to understand better how radiation can actually disturb the accretion disk and influence its surrounding. We might inspire our answer for these questions from the present day star-formation studies, or we have to involve an additional physic processes, e.g. magnetic fields and formation of jets.

7.2 Outlook

Now that we have at hand a self-consistent way to simulate interactions between radiation and gas dynamics, we have the opportunity to explore several other questions in astrophysics. In the following paragraphs, we give a brief list of projects that we want to address in our future work.

Sub-grid calculations of expanding HII regions often use idealized spherical models with homogeneous gas distribution or completely neglect gas dynamics close to the stars. From our simulations of Pop-III star formation we learned, that the recombination rates in approximately 10 AU thick molecular accretion disks can be high enough to trap ionizing photons. In the following study, we want to investigate possible ways of how a star can disrupt such conditions, e.g., by the formation of jets.

Precise calculations of the D-front expansion of HII regions and chemistry in densities above 10^{10} cm^{-3} require time steps several orders lower than those needed by the hydrodynamics. Such high temporal resolution is not feasible for large scale simulations. Therefore, we want to study isolated high-resolution cases of these processes, devise new reliable sub-grid models, and define constraints for this problem on larger scales.

Population III stars stars form in mini-haloes at the early stage of the Universe. So far, we study this process only on isolated mini-haloes with the initial Bonnor-Ebert sphere gas distribution. Due to the non-linear nature of both hydrodynamics and radiation transfer, we will need to study a larger statistical sample of such simulations. Ideally, we will perform a set of zoom-in simulations of mini-haloes from the state-of-art cosmological catalogs. Higher statistical sample will help us to get better estimates of the primordial initial mass function.

Having an accurate distribution of Pop-III stars in the early Universe is a fundamental prerequisite that allows us to study metal enrichment of the later ISM and stars in the first galaxies. High-mass stars, composed only from Hydrogen and Helium, end their live cycle as supernovae within several Myr after formation. Their explosions release higher elements and metals into the ISM. This material serves subsequently as a building material for the next generations of Pop-II stars. We already study these processes at our department in Heidelberg (Magg et al., in prep.). SPRAI is in this project used to simulate HII regions around the first stars, which in subsequent supernovae explosions enhance metal enrichment of the surrounding ISM. From the analysis of these processes using tracer particles, we will learn more about the distribution of metals in the primordial haloes and their effect on further star-formation.

The extension of the SPRAI will be necessary for my future work. We need to improve some physical aspects of our models. Even though our simulation is self-consistently solving hydrodynamics and radiation, we are currently excluding several other physical aspects such as magnetic field and sink particle merging. The current version of the SPRAI is working

only with primordial chemistry. Further on, we have to implement the dust chemistry and self-shielding from the molecular hydrogen to make our primordial model complete.

Besides stars, other ionization sources in the primordial Universe left a noticeable trace for the present-day observers. Ionizing radiation from AGN in first galaxies plays an essential role in the study of the 21cm line. In collaboration with a group from the University of Cambridge, we started to integrate soft and hard X-rays into the SPRAI. First, we plan to study X-ray radiation from individual minihaloes. As a next step, we want to perform large-scale simulations of X-ray ionization and derive a prediction of 21cm line observations.

An adaptation of SPRAI for the present-day star formation is also possible. This extension would be useful for simulations of the HII region in galactic disks and molecular clouds in our close Universe. Our current department in Heidelberg has an interest in extending the code for this purpose.

8 Acknowledgements

The study contained in this thesis would not be possible without the previous work and achievement of many scientists mentioned and cited in this work. I want to express a special thanks and appreciation to prof. Dr. Ralf Klessen and prof. Dr. Simon Glover for giving me the opportunity to explore these fascinating parts of the Astrophysical research. Their expertise, assistance, and accompanying during the study has a great value to me and for my future career.

Thanks also belongs to my colleagues with whom I shared my daily routine and which were always helpful to discuss and help with various topics. Among these belong Robin Tress, Mattis Magg, Katharina Wollenberg, Sacha Hony, Kiwan Park, and many others. A special thanks belong to Anna Schauer for her support and help during the development of SPRAI and for her computational time when it was needed. As well as to Sam Geen for the discussions and help with corrections.

We thank prof. Dr. Volker Springel for giving us access to the AREPO code and for his help. We also thank Paul Clark and Oliver Lomax for useful discussions on the behavior of the SIMPLEX algorithm. The authors would like to thank Dr. Thomas Bisbas for his kind help with setting up the tests from the STARBENCH code comparison paper.

We acknowledge support by the European Research Council under the European Community's Seventh Framework Programme (FP7/2007-2013) via the ERC Advanced Grant 'STARLIGHT: Formation of the First Stars' (project number 339177). SCOG and RSK also acknowledge support from the DFG via SPP 1573 "Physics of the Interstellar Medium" (grant number GL 668/2-1). Financial support for this work was also provided by the Deutsche Forschungsgemeinschaft (DFG) via the Collaborative Research Centre SFB 881-138713538 "The Milky Way System" (sub-projects A1, B1, B2, and B8) and from the Heidelberg cluster of excellence EXC 2181/1-390900948 "STRUCTURES: A unifying approach to emergent phenomena in the physical world, mathematics, and complex data", funded by the German Excellence Strategy.

The authors gratefully acknowledge the data storage service SDS@hd, supported by the Ministry of Science, Research and the Arts Baden-Württemberg (MWK) and the DFG through grants INST 35/1314-1 FUGG and INST 35/1503-1 FUGG, as well as the MLS&WISO Production Cluster, supported by the state of Baden-Württemberg through bwHPC and the DFG through grant INST 35/1134-1 FUGG.

Part II

Appendix

A List of abbreviations

Common abbreviations

AGN	active galactic nuclei
BB	Big Bang
BES	Bonnor-Ebert sphere
CIE	collision-induced emission
CMB	Cosmic Microwave Background
DE	dark energy
DM	dark matter
D-type	density-type
EoR	Epoch of Reionization
FLD	flux-limited diffusion
I-front	ionization front
IGM	intergalactic medium
IMF	initial mass function
ISM	interstellar medium
ΛCDM	Lambda Cold Dark Matter
LW	Lyman-Werner
PDRs	photodissociation regions
Pop-I	Population I stars
Pop-II	Population II stars
Pop-III	Population III stars
RT	radiative transport
R-type	rarified-type
UV	ultraviolet
WDM	Warm Dark Matter

Codes and projects

AREPO	the AREPO code
AURIGA	AURIGA simulation
FERVENT	radiative transfer module for the magnetohydrodynamical adaptive mesh refinement code FLASH-4
GADGET	the GADGET-2 code
HEALPIX	HEALPIX algorithm
ILLUSTRIS	ILLUSTRIS simulation
ILLUSTRIS-TNG	ILLUSTRIS-TNG simulation
RAMSES	the RAMSES code
RAMSES-RT	RAMSES radiation transfer implementation
SGCHEM	SGCHEM chemistry module
SIMPLEX	SIMPLEX radiation transfer
SPRAI	SPRAI module
SPRAI-I	basic version of SPRAI
SPRAI-II	extended version of SPRAI
STARBENCH	STARBENCH code comparison project

B List of publications

- O. Jaura, S. C. O. Glover, R. S. Klessen, and J.-P. Paardekooper. sprai: coupling of radiative feedback and primordial chemistry in moving mesh hydrodynamics. *Monthly Notices of the Royal Astronomical Society*, 475(2):2822–2834, Apr. 2018. ISSN 0035-8711. doi: 10.1093/mnras/stx3356
- O. Jaura, M. Magg, S. C. O. Glover, and R. S. Klessen. sprai-ii: multifrequency radiative transfer for variable gas densities. *MNRAS, submitted*, 2020

Publications listed above are discussed in more detail at the beginning of Chapters 4 and 5, respectively.

C Bibliography

T. Abel and B. D. Wandelt. Adaptive ray tracing for radiative transfer around point sources. *Monthly Notices of the Royal Astronomical Society*, 330(3):L53–L56, Mar. 2002. doi: 10.1046/j.1365-8711.2002.05206.x.

T. Abel, M. L. Norman, and P. Madau. Photon-conserving Radiative Transfer around Point Sources in Multidimensional Numerical Cosmology. *The Astrophysical Journal*, 523(1): 66–71, Sept. 1999. doi: 10.1086/307739.

T. Abel, G. L. Bryan, and M. L. Norman. The Formation of the First Star in the Universe. *Science*, 295(5552):93–98, Jan. 2002. ISSN 0036-8075, 1095-9203. doi: 10.1126/science.1063991.

T. Abel, J. H. Wise, and G. L. Bryan. The H II Region of a Primordial Star. *The Astrophysical Journal Letters*, 659:L87–L90, Apr. 2007. doi: 10.1086/516820.

M. A. Alvarez, V. Bromm, and P. R. Shapiro. The H II Region of the First Star. *The Astrophysical Journal*, 639:621–632, Mar. 2006. ISSN 0004-637X. doi: 10.1086/499578.

D. Aubert and R. Teyssier. A radiative transfer scheme for cosmological reionization based on a local Eddington tensor. *Monthly Notices of the Royal Astronomical Society*, 387(1): 295–307, June 2008. doi: 10.1111/j.1365-2966.2008.13223.x.

C. Baczynski, S. C. O. Glover, and R. S. Klessen. Fervent: chemistry-coupled, ionizing and non-ionizing radiative feedback in hydrodynamical simulations. *Monthly Notices of the Royal Astronomical Society*, 454(1):380–411, Nov. 2015. ISSN 0035-8711. doi: 10.1093/mnras/stv1906.

A. Bauer, V. Springel, M. Vogelsberger, S. Genel, P. Torrey, D. Sijacki, D. Nelson, and L. Hernquist. Hydrogen reionization in the Illustris universe. *Monthly Notices of the Royal Astronomical Society*, 453(4):3593, Nov. 2015. doi: 10.1093/mnras/stv1893.

T. C. Beers and N. Christlieb. The Discovery and Analysis of Very Metal-Poor Stars in the Galaxy. *Annual Review of Astron and Astrophys*, 43:531–580, Sept. 2005. doi: 10.1146/annurev.astro.42.053102.134057.

T. G. Bisbas, T. J. Haworth, R. J. R. Williams, J. Mackey, P. Tremblin, A. C. Raga, S. J. Arthur, C. Baczynski, J. E. Dale, T. Frostholm, S. Geen, T. Haugbølle, D. Hubber, I. T. Iliev, R. Kuiper, J. Rosdahl, D. Sullivan, S. Walch, and R. Wünsch. starbench: the D-type expansion of an H ii region. *Monthly Notices of the Royal Astronomical Society*, 453(2): 1324–1343, Oct. 2015. ISSN 0035-8711. doi: 10.1093/mnras/stv1659.

A. C. Boley, T. W. Hartquist, R. H. Durisen, and S. Michael. The Internal Energy for Molecular Hydrogen in Gravitationally Unstable Protoplanetary Disks. *The Astrophysical Journal Letters*, 656(2):L89–L92, Feb. 2007. doi: 10.1086/512235.

S. Bovino, T. Grassi, M. A. Latif, and D. R. G. Schleicher. Impact of an accurate modelling of primordial chemistry in high-resolution studies. *Monthly Notices of the Royal Astronomical Society*, 434:L36–L40, July 2013a. doi: 10.1093/mnrasl/slt072.

S. Bovino, D. R. G. Schleicher, and J. Schober. Turbulent magnetic field amplification from the smallest to the largest magnetic Prandtl numbers. *New Journal of Physics*, 15(1): 013055, Jan. 2013b. doi: 10.1088/1367-2630/15/1/013055.

V. Bromm. Formation of the first stars. *Rep. Prog. Phys.*, 76(11):112901, Nov. 2013. doi: 10.1088/0034-4885/76/11/112901.

V. Bromm and R. B. Larson. The First Stars. *Annual Review of Astron and Astrophys*, 42: 79–118, Sept. 2004. doi: 10.1146/annurev.astro.42.053102.134034.

V. Bromm, P. S. Coppi, and R. B. Larson. The Formation of the First Stars. I. The Primordial Star-forming Cloud. *The Astrophysical Journal*, 564:23–51, Jan. 2002. doi: 10.1086/323947.

V. Bromm, N. Yoshida, L. Hernquist, and C. F. McKee. The formation of the first stars and galaxies. *Nature*, 459:49–54, May 2009. ISSN 0028-0836. doi: 10.1038/nature07990.

M. G. Burton, D. J. Hollenbach, and A. G. G. M. Tielens. Line Emission from Clumpy Photodissociation Regions. *The Astrophysical Journal*, 365:620, Dec. 1990. doi: 10.1086/169516.

E. Caffau, P. Bonifacio, P. François, L. Sbordone, L. Monaco, M. Spite, F. Spite, H.-G. Ludwig, R. Cayrel, S. Zaggia, F. Hammer, S. Randich, P. Molaro, and V. Hill. An extremely primitive star in the Galactic halo. *Nature*, 477:67–69, Sept. 2011. doi: 10.1038/nature10377.

P. C. Clark, S. C. O. Glover, R. S. Klessen, and V. Bromm. Gravitational Fragmentation in Turbulent Primordial Gas and the Initial Mass Function of Population III Stars. *The Astrophysical Journal*, 727(2):110, Feb. 2011a. ISSN 0004-637X. doi: 10.1088/0004-637X/727/2/110.

P. C. Clark, S. C. O. Glover, R. J. Smith, T. H. Greif, R. S. Klessen, and V. Bromm. The Formation and Fragmentation of Disks Around Primordial Protostars. *Science*, 331 (6020):1040, Feb. 2011b. doi: 10.1126/science.1198027.

P. C. Clark, S. C. O. Glover, S. E. Ragan, and A. Duarte-Cabral. Tracing the formation of molecular clouds via [C II], [C I], and CO emission. *Monthly Notices of the Royal Astronomical Society*, 486(4):4622–4637, July 2019. doi: 10.1093/mnras/stz1119.

B. Commerçon, P. Hennebelle, and T. Henning. Collapse of Massive Magnetized Dense Cores Using Radiation Magnetohydrodynamics: Early Fragmentation Inhibition. *The Astrophysical Journal Letters*, 742:L9, Nov. 2011. doi: 10.1088/2041-8205/742/1/L9.

S. W. Davis, J. M. Stone, and Y.-F. Jiang. A Radiation Transfer Solver for Athena Using Short Characteristics. *The Astrophysical Journal Supplement Series*, 199(1):9, Mar. 2012. doi: 10.1088/0067-0049/199/1/9.

B. T. Draine. Photoelectric heating of interstellar gas. *The Astrophysical Journal Supplement Series*, 36:595–619, Apr. 1978. doi: 10.1086/190513.

B. T. Draine and F. Bertoldi. Structure of Stationary Photodissociation Fronts. *The Astrophysical Journal*, 468:269, Sept. 1996. doi: 10.1086/177689.

C. P. Dullemond, A. Juhasz, A. Pohl, F. Sereshti, R. Shetty, T. Peters, B. Commercon, and M. Flock. RADMC-3D: A multi-purpose radiative transfer tool. *Astrophysics Source Code Library*, page ascl:1202.015, Feb. 2012.

J. J. Eldridge and E. R. Stanway. BPASS predictions for binary black hole mergers. *Monthly Notices of the Royal Astronomical Society*, 462:3302–3313, Nov. 2016. ISSN 0035-8711. doi: 10.1093/mnras/stw1772.

B. Ercolano, P. R. Young, J. J. Drake, and J. C. Raymond. X-Ray Enabled MOCASSIN: A Three-dimensional Code for Photoionized Media. *The Astrophysical Journal Supplement Series*, 175(2):534–542, Apr. 2008. doi: 10.1086/524378.

P. Feautrier. Sur la resolution numerique de l'equation de transfert. *Comptes Rendus Academie des Sciences*, 258:3189, 1964.

G. J. Ferland, B. M. Peterson, K. Horne, W. F. Welsh, and S. N. Nahar. Anisotropic line emission and the geometry of the broad-line region in active galactic nuclei. *The Astrophysical Journal*, 387:95–108, Mar. 1992. doi: 10.1086/171063.

K. Finlator, F. Özel, and R. Davé. A new moment method for continuum radiative transfer in cosmological re-ionization. *Monthly Notices of the Royal Astronomical Society*, 393 (4):1090–1106, Mar. 2009. doi: 10.1111/j.1365-2966.2008.14190.x.

J. Franco, G. Tenorio-Tagle, and P. Bodenheimer. On the formation and expansion of H II regions. *ApJ*, 349:126–140, 1990. ISSN 0004-637X. doi: 10.1086/168300.

T. Frostholm, T. Haugbølle, and T. Grassi. Lampray: Multi-group long characteristics ray tracing for adaptive mesh radiation hydrodynamics. *arXiv e-prints*, page arXiv:1809.05541, Sept. 2018.

B. Fryxell, K. Olson, P. Ricker, F. X. Timmes, M. Zingale, D. Q. Lamb, P. MacNeice, R. Rosner, J. W. Truran, and H. Tufo. FLASH: An Adaptive Mesh Hydrodynamics Code for Modeling Astrophysical Thermonuclear Flashes. *The Astrophysical Journal Supplement Series*, 131(1):273–334, Nov. 2000. ISSN 0067-0049. doi: 10.1086/317361.

P. Girichidis, C. Federrath, R. Banerjee, and R. S. Klessen. Importance of the initial conditions for star formation - II. Fragmentation-induced starvation and accretion shielding. *Monthly Notices of the Royal Astronomical Society*, 420:613–626, Feb. 2012. doi: 10.1111/j.1365-2966.2011.20073.x.

S. Glover. The Formation Of The First Stars In The Universe. *Space Science Reviews*, 117: 445–508, Apr. 2005. doi: 10.1007/s11214-005-5821-y.

S. Glover. The First Stars. In T. Wiklind, B. Mobasher, and V. Bromm, editors, *The First Galaxies*, volume 396 of *Astrophysics and Space Science Library*, page 103, 2013. doi: 10.1007/978-3-642-32362-1_3.

S. C. O. Glover. The Chemistry of the Early Universe. In J. Cernicharo and R. Bachiller, editors, *The Molecular Universe*, volume 280 of *IAU Symposium*, pages 313–324, Dec. 2011. doi: 10.1017/S1743921311025075.

S. C. O. Glover. Simulating the formation of massive seed black holes in the early Universe - I. An improved chemical model. *Monthly Notices of the Royal Astronomical Society*, 451:2082–2096, Aug. 2015a. doi: 10.1093/mnras/stv1059.

S. C. O. Glover. Simulating the formation of massive seed black holes in the early Universe - II. Impact of rate coefficient uncertainties. *Monthly Notices of the Royal Astronomical Society*, 453:2901–2918, Nov. 2015b. doi: 10.1093/mnras/stv1781.

S. C. O. Glover. The dynamics of ionization and dissociation fronts in extremely dense primordial gas. *Mem. Societa Astronomica Italiana*, 88:682, Jan. 2017.

S. C. O. Glover and T. Abel. Uncertainties in H_2 and HD chemistry and cooling and their role in early structure formation. *Monthly Notices of the Royal Astronomical Society*, 388: 1627–1651, Aug. 2008. doi: 10.1111/j.1365-2966.2008.13224.x.

S. C. O. Glover and P. C. Clark. Approximations for modelling CO chemistry in giant molecular clouds: a comparison of approaches. *Monthly Notices of the Royal Astronomical Society*, 421:116–131, Mar. 2012. ISSN 0035-8711. doi: 10.1111/j.1365-2966.2011.20260.x.

S. C. O. Glover and A.-K. Jappsen. Star Formation at Very Low Metallicity. I. Chemistry and Cooling at Low Densities. *The Astrophysical Journal*, 666:1–19, Sept. 2007. doi: 10.1086/519445.

K. M. Górski, E. Hivon, A. J. Banday, B. D. Wandelt, F. K. Hansen, M. Reinecke, and M. Bartelmann. HEALPix: A Framework for High-Resolution Discretization and Fast Analysis of Data Distributed on the Sphere. *The Astrophysical Journal*, 622:759–771, Apr. 2005. doi: 10.1086/427976.

R. J. J. Grand, F. A. Gómez, F. Marinacci, R. Pakmor, V. Springel, D. J. R. Campbell, C. S. Frenk, A. Jenkins, and S. D. M. White. The Auriga Project: the properties and formation mechanisms of disc galaxies across cosmic time. *MNRAS*, 467:179, Jan. 2017. ISSN 0035-8711. doi: 10.1093/mnras/stx071.

T. H. Greif. Multifrequency radiation hydrodynamics simulations of H2 line emission in primordial, star-forming clouds. *Mon. Not. R. Astron. Soc.*, 444(2):1566–1583, Aug. 2014. ISSN 0035-8711. doi: 10.1093/mnras/stu1532.

T. H. Greif, J. L. Johnson, R. S. Klessen, and V. Bromm. The first galaxies: assembly, cooling and the onset of turbulence. *Monthly Notices of the Royal Astronomical Society*, 387:1021–1036, July 2008. doi: 10.1111/j.1365-2966.2008.13326.x.

T. H. Greif, S. C. O. Glover, V. Bromm, and R. S. Klessen. The First Galaxies: Chemical Enrichment, Mixing, and Star Formation. *The Astrophysical Journal*, 716(1):510, June 2010. doi: 10.1088/0004-637X/716/1/510.

T. H. Greif, V. Springel, S. D. M. White, S. C. O. Glover, P. C. Clark, R. J. Smith, R. S. Klessen, and V. Bromm. SIMULATIONS ON A MOVING MESH: THE CLUSTERED FORMATION OF POPULATION III PROTOSTARS. *ApJ*, 737(2):75, Aug. 2011a. ISSN 0004-637X. doi: 10.1088/0004-637X/737/2/75.

T. H. Greif, S. D. M. White, R. S. Klessen, and V. Springel. The Delay of Population III Star Formation by Supersonic Streaming Velocities. *The Astrophysical Journal*, 736:147, Aug. 2011b. doi: 10.1088/0004-637X/736/2/147.

T. H. Greif, V. Bromm, P. C. Clark, S. C. O. Glover, R. J. Smith, R. S. Klessen, N. Yoshida, and V. Springel. Formation and evolution of primordial protostellar systems. *Monthly Notices of the Royal Astronomical Society*, 424:399–415, July 2012. doi: 10.1111/j.1365-2966.2012.21212.x.

M. G. Haehnelt. Momentum transfer by an internal source of ionizing radiation: an important feedback process during galaxy formation? *Monthly Notices of the Royal Astronomical Society*, 273(2):249–256, Mar. 1995. doi: 10.1093/mnras/273.2.249.

L. Haemmerlé, T. E. Woods, R. S. Klessen, A. Heger, and D. J. Whalen. The evolution of supermassive Population III stars. *Monthly Notices of the Royal Astronomical Society*, 474(2):2757, Feb. 2018. doi: 10.1093/mnras/stx2919.

T. J. Harries, T. J. Haworth, D. Acreman, A. Ali, and T. Douglas. The TORUS radiation transfer code. *Astronomy and Computing*, 27:63, Apr. 2019. doi: 10.1016/j.ascom.2019.03.002.

T. Hartwig, P. C. Clark, S. C. O. Glover, R. S. Klessen, and M. Sasaki. A new approach to determine optically thick H2 cooling and its effect on primordial star formation. *ArXiv e-prints:1407.2102*, July 2014.

T. Hartwig, S. C. O. Glover, R. S. Klessen, M. A. Latif, and M. Volonteri. How an improved implementation of H_2 self-shielding influences the formation of massive stars and black holes. *Monthly Notices of the Royal Astronomical Society*, 452:1233–1244, Sept. 2015. doi: 10.1093/mnras/stv1368.

J. C. Hayes and M. L. Norman. Beyond Flux-limited Diffusion: Parallel Algorithms for Multidimensional Radiation Hydrodynamics. *The Astrophysical Journal Supplement Series*, 147(1):197–220, July 2003. doi: 10.1086/374658.

A. Heger and S. E. Woosley. The Nucleosynthetic Signature of Population III. *The Astrophysical Journal*, 567:532–543, Mar. 2002. doi: 10.1086/338487.

A. Heger and S. E. Woosley. Nucleosynthesis and Evolution of Massive Metal-free Stars. *The Astrophysical Journal*, 724:341–373, Nov. 2010. doi: 10.1088/0004-637X/724/1/341.

A. Heger, C. L. Fryer, S. E. Woosley, N. Langer, and D. H. Hartmann. How Massive Single Stars End Their Life. *The Astrophysical Journal*, 591:288–300, July 2003. ISSN 0004-637X. doi: 10.1086/375341.

S. Hirano and V. Bromm. Formation and survival of Population III stellar systems. *Monthly Notices of the Royal Astronomical Society*, 470(1):898, Sept. 2017. doi: 10.1093/mnras/stx1220.

S. Hirano, T. Hosokawa, N. Yoshida, H. Umeda, K. Omukai, G. Chiaki, and H. W. Yorke. One Hundred First Stars: Protostellar Evolution and the Final Masses. *The Astrophysical Journal*, 781:60, Feb. 2014. ISSN 0004-637X. doi: 10.1088/0004-637X/781/2/60.

S. Hirano, T. Hosokawa, N. Yoshida, K. Omukai, and H. W. Yorke. Primordial star formation under the influence of far ultraviolet radiation: 1540 cosmological haloes and the stellar mass distribution. *Monthly Notices of the Royal Astronomical Society*, 448:568–587, Mar. 2015. ISSN 0035-8711. doi: 10.1093/mnras/stv044.

P. F. Hopkins. GIZMO: A New Class of Accurate, Mesh-Free Hydrodynamic Simulation Methods. *Monthly Notices of the Royal Astronomical Society*, 450(1):53–110, June 2015. ISSN 0035-8711, 1365-2966. doi: 10.1093/mnras/stv195. arXiv: 1409.7395.

P. F. Hopkins and M. Y. Grudic. Numerical problems in coupling photon momentum (radiation pressure) to gas. *Monthly Notices of the Royal Astronomical Society*, 483(3):4187, Mar. 2019. doi: 10.1093/mnras/sty3089.

T. Hosokawa and S.-i. Inutsuka. Dynamical Expansion of Ionization and Dissociation Front around a Massive Star. II. On the Generality of Triggered Star Formation. *The Astrophysical Journal*, 646(1):240, July 2006a. doi: 10.1086/504789.

T. Hosokawa and S.-i. Inutsuka. Dynamical Expansion of Ionization and Dissociation Front around a Massive Star: A Starburst Mechanism. *The Astrophysical Journal*, 648(2):L131, Sept. 2006b. doi: 10.1086/507887.

T. Hosokawa and K. Omukai. Evolution of Massive Protostars with High Accretion Rates. *The Astrophysical Journal*, 691:823–846, Jan. 2009. doi: 10.1088/0004-637X/691/1/823.

T. Hosokawa, H. W. Yorke, and K. Omukai. Evolution of Massive Protostars Via Disk Accretion. *The Astrophysical Journal*, 721:478–492, Sept. 2010. doi: 10.1088/0004-637X/721/1/478.

T. Hosokawa, K. Omukai, N. Yoshida, and H. W. Yorke. Protostellar Feedback Halts the Growth of the First Stars in the Universe. *Science*, 334(6060):1250, Dec. 2011. doi: 10.1126/science.1207433.

T. Hosokawa, N. Yoshida, K. Omukai, and H. W. Yorke. Protostellar Feedback and Final Mass of the Second-generation Primordial Stars. *The Astrophysical Journal Letters*, 760: L37, Dec. 2012. doi: 10.1088/2041-8205/760/2/L37.

T. Hosokawa, S. Hirano, R. Kuiper, H. W. Yorke, K. Omukai, and N. Yoshida. Formation of Massive Primordial Stars: Intermittent UV Feedback with Episodic Mass Accretion. *The Astrophysical Journal*, 824(2):119, June 2016. doi: 10.3847/0004-637X/824/2/119.

T. Hsyu, R. J. Cooke, J. X. Prochaska, and M. Bolte. The Little Cub: Discovery of an Extremely Metal-Poor Star-Forming Galaxy in the Local Universe. *arXiv*, 2017. arXiv: 1708.01260.

D. G. Hummer and P. J. Storey. Recombination of helium-like ions - I. Photoionization cross-sections and total recombination and cooling coefficients for atomic helium. *Monthly Notices of the Royal Astronomical Society*, 297:1073–1078, July 1998. doi: 10.1046/j.1365-8711.1998.2970041073.x.

I. T. Iliev, B. Ciardi, M. A. Alvarez, A. Maselli, A. Ferrara, N. Y. Gnedin, G. Mellema, T. Nakamoto, M. L. Norman, A. O. Razoumov, E. J. Rijkhorst, J. Ritzerveld, P. R. Shapiro, H. Susa, M. Umemura, and D. J. Whalen. Cosmological radiative transfer codes comparison project - I. The static density field tests. *MNRAS*, 371(3):1057–1086, Mar. 2006. ISSN 00358711. doi: 10.1111/j.1365-2966.2006.10775.x.

I. T. Iliev, D. Whalen, G. Mellema, K. Ahn, S. Baek, N. Y. Gnedin, A. V. Kravtsov, M. Norman, M. Raicevic, D. R. Reynolds, D. Sato, P. R. Shapiro, B. Semelin, J. Smidt, H. Susa, T. Theuns, and M. Umemura. Cosmological Radiative Transfer Comparison Project II: The Radiation-Hydrodynamic Tests. *MNRAS*, 400(3):1283–1316, May 2009. ISSN 00358711. doi: 10.1111/j.1365-2966.2009.15558.x.

J. Jaacks, R. Thompson, S. L. Finkelstein, and V. Bromm. Baseline metal enrichment from Population III star formation in cosmological volume simulations. *Monthly Notices of the Royal Astronomical Society*, 475:4396–4410, Apr. 2018. ISSN 0035-8711. doi: 10.1093/mnras/sty062.

O. Jaura, S. C. O. Glover, R. S. Klessen, and J.-P. Paardekooper. sprai: coupling of radiative feedback and primordial chemistry in moving mesh hydrodynamics. *Monthly Notices of the Royal Astronomical Society*, 475(2):2822–2834, Apr. 2018. ISSN 0035-8711. doi: 10.1093/mnras/stx3356.

O. Jaura, M. Magg, S. C. O. Glover, and R. S. Klessen. sprai-ii: multifrequency radiative transfer for variable gas densities. *MNRAS, submitted*, 2020.

J. H. Jeans. The Stability of a Spherical Nebula. *Philosophical Transactions of the Royal Society of London Series A*, 199:1–53, 1902. ISSN 0080-4614. doi: 10.1098/rsta.1902.0012.

M. Jeon, A. H. Pawlik, V. Bromm, and M. Milosavljević. Radiative feedback from high-mass X-ray binaries on the formation of the first galaxies and early reionization. *Monthly Notices of the Royal Astronomical Society*, 440:3778–3796, June 2014. doi: 10.1093/mnras/stu444.

J. L. Johnson, C. Dalla Vecchia, and S. Khochfar. The First Billion Years project: the impact of stellar radiation on the co-evolution of Populations II and III. *Monthly Notices of the Royal Astronomical Society*, 428(3):1857, Jan. 2013. doi: 10.1093/mnras/sts011.

R. Kannan, M. Vogelsberger, F. Marinacci, R. McKinnon, R. Pakmor, and V. Springel. AREPO-RT: radiation hydrodynamics on a moving mesh. *Monthly Notices of the Royal Astronomical Society*, 485(1):117–149, May 2019. doi: 10.1093/mnras/stz287.

E. Keto. On the Evolution of Ultracompact H II Regions. *The Astrophysical Journal*, 580 (2):980–986, Dec. 2002. doi: 10.1086/343794.

E. Keto. The Formation of Massive Stars: Accretion, Disks, and the Development of Hypercompact H II Regions. *The Astrophysical Journal*, 666:976–981, Sept. 2007. doi: 10.1086/520320.

R. Kippenhahn, A. Weigert, and A. Weiss. *Stellar Structure and Evolution*. Springer Verlag Berlin Heidelberg, 2012. doi: 10.1007/978-3-642-30304-3.

T. Kitayama, N. Yoshida, H. Susa, and M. Umemura. The Structure and Evolution of Early Cosmological H II Regions. *The Astrophysical Journal*, 613:631–645, Oct. 2004. doi: 10.1086/423313.

R. S. Klessen. Formation of the first stars. In M. Latif and D. Schleicher, editors, *Formation of the first black holes*, World Scientific Publishing Company, page 67, July 2018.

P. Kroupa. The Initial Mass Function of Stars: Evidence for Uniformity in Variable Systems. *Science*, 295:82–91, Jan. 2002. doi: 10.1126/science.1067524.

C. J. H. Kruip, J.-P. Paardekooper, B. J. F. Clauwens, and V. Icke. Mathematical properties of the SimpleX algorithm. *Astronomy and Astrophysics*, 515:A78, June 2010. doi: 10.1051/0004-6361/200913439.

M. R. Krumholz, R. I. Klein, C. F. McKee, S. S. R. Offner, and A. J. Cunningham. The Formation of Massive Star Systems by Accretion. *Science*, 323:754, Feb. 2009. doi: 10.1126/science.1165857.

R. Kuiper, H. Klahr, H. Beuther, and T. Henning. Circumventing the Radiation Pressure Barrier in the Formation of Massive Stars via Disk Accretion. *The Astrophysical Journal*, 722:1556–1576, Oct. 2010. doi: 10.1088/0004-637X/722/2/1556.

R. Kuiper, H. Klahr, H. Beuther, and T. Henning. Three-dimensional Simulation of Massive Star Formation in the Disk Accretion Scenario. *The Astrophysical Journal*, 732:20, May 2011. doi: 10.1088/0004-637X/732/1/20.

P. Kunasz and L. H. Auer. Short characteristic integration of radiative transfer problems: formal solution in two-dimensional slabs. *Journal of Quantitiative Spectroscopy and Radiative Transfer*, 39:67–79, Jan. 1988. doi: 10.1016/0022-4073(88)90021-0.

C. Leitherer, D. Schaerer, J. D. Goldader, R. M. G. Delgado, C. Robert, D. F. Kune, D. F. de Mello, D. Devost, and T. M. Heckman. Starburst99: Synthesis Models for Galaxies with Active Star Formation. *The Astrophysical Journal Supplement Series*, 123:3–40, July 1999. doi: 10.1086/313233.

C. D. Levermore and G. C. Pomraning. A flux-limited diffusion theory. *The Astrophysical Journal*, 248:321–334, Aug. 1981. doi: 10.1086/159157.

R. Li, C. S. Frenk, S. Cole, L. Gao, S. Bose, and W. A. Hellwing. Constraints on the identity of the dark matter from strong gravitational lenses. *Monthly Notices of the Royal Astronomical Society*, 460:363–372, July 2016. ISSN 0035-8711. doi: 10.1093/mnras/stw939.

A. Lipovka, R. Núñez-López, and V. Avila-Reese. The cooling function of HD molecule revisited. *Monthly Notices of the Royal Astronomical Society*, 361:850–854, Aug. 2005. doi: 10.1111/j.1365-2966.2005.09226.x.

X. Liu and D. E. Shemansky. Nondissociative electron and photon ionization cross sections of molecular hydrogen and deuterium. *Journal of Physics B Atomic Molecular Physics*, 45(9):095203, May 2012. doi: 10.1088/0953-4075/45/9/095203.

A. Loeb. *How Did the First Stars and Galaxies Form?* Princeton University Press, 2010.

M. N. Machida and T. Nakamura. Accretion phase of star formation in clouds with different metallicities. *Monthly Notices of the Royal Astronomical Society*, 448(2):1405, Apr. 2015. doi: 10.1093/mnras/stu2633.

M. N. Machida, K. Omukai, T. Matsumoto, and S.-i. Inutsuka. The First Jets in the Universe: Protostellar Jets from the First Stars. *The Astrophysical Journal Letters*, 647:L1–L4, Aug. 2006. doi: 10.1086/507326.

M. N. Machida, T. Matsumoto, and S.-i. Inutsuka. Magnetohydrodynamics of Population III Star Formation. *The Astrophysical Journal*, 685:690–704, Oct. 2008. doi: 10.1086/591074.

J. Mackey. Accuracy and efficiency of raytracing photoionisation algorithms. *Astronomy and Astrophysics*, 539:A147, Mar. 2012. doi: 10.1051/0004-6361/201117984.

P. Madau, F. Haardt, and M. Dotti. Super-critical Growth of Massive Black Holes from Stellar-mass Seeds. *The Astrophysical Journal Letters*, 784:L38, Apr. 2014. doi: 10.1088/2041-8205/784/2/L38.

A. Maeder and G. Meynet. Rotating massive stars: From first stars to gamma ray bursts. *Rev. Mod. Phys.*, 84:25–63, Jan. 2012. doi: 10.1103/RevModPhys.84.25.

U. Maio, L. V. E. Koopmans, and B. Ciardi. The impact of primordial supersonic flows on early structure formation, reionization and the lowest-mass dwarf galaxies. *Monthly Notices of the Royal Astronomical Society*, 412:L40–L44, Mar. 2011. doi: 10.1111/j.1745-3933.2010.01001.x.

A. Maselli, A. Ferrara, and B. Ciardi. CRASH: a radiative transfer scheme. *Monthly Notices of the Royal Astronomical Society*, 345(2):379–394, Oct. 2003. doi: 10.1046/j.1365-8711.2003.06979.x.

M. Mayer and W. J. Duschl. Rosseland and Planck mean opacities for primordial matter. *Monthly Notices of the Royal Astronomical Society*, 358:614–631, Apr. 2005. doi: 10.1111/j.1365-2966.2005.08826.x.

G. Mellema, I. T. Iliev, M. A. Alvarez, and P. R. Shapiro. C2-ray: A new method for photon-conserving transport of ionizing radiation. *New Astron.*, 11(5):374–395, 2006. ISSN 13841076. doi: 10.1016/j.newast.2005.09.004.

D. Mihalas, L. H. Auer, and B. R. Mihalas. Two-dimensional radiative transfer. I. Planar geometry. *The Astrophysical Journal*, 220:1001–1023, Mar. 1978. doi: 10.1086/155988.

K. Omukai. Primordial Star Formation under Far-Ultraviolet Radiation. *The Astrophysical Journal*, 546:635–651, Jan. 2001. doi: 10.1086/318296.

K. Omukai and R. Nishi. Evolution of primordial protostellar clouds. *Memorie della Società Astronomia Italiana*, 1998.

K. Omukai and F. Palla. On the Formation of Massive Primordial Stars. *The Astrophysical Journal Letters*, 561:L55–L58, Nov. 2001. doi: 10.1086/324410.

K. Omukai and F. Palla. Formation of the First Stars by Accretion. *The Astrophysical Journal*, 589:677–687, June 2003. doi: 10.1086/374810.

B. W. O'Shea and M. L. Norman. Population III Star Formation in a Lambda CDM Universe. I. The Effect of Formation Redshift and Environment on Protostellar Accretion Rate. *The Astrophysical Journal*, 654:66–92, Jan. 2007. doi: 10.1086/509250.

D. E. Osterbrock. *Astrophysics of gaseous nebulae and active galactic nuclei*. University Science Books, 1989. ISBN 0-935702-22-9.

D. E. Osterbrock and G. J. Ferland. *Astrophysics of gaseous nebulae and active galactic nuclei*. University Science Books, 2006.

J.-P. Paardekooper, C. J. H. Kruip, and V. Icke. SimpleX2: radiative transfer on an unstructured, dynamic grid. *Astronomy and Astrophysics*, 515:A79, June 2010. doi: 10.1051/0004-6361/200913821.

J.-P. Paardekooper, S. Khochfar, and C. Dalla Vecchia. The First Billion Years project: the escape fraction of ionizing photons in the epoch of reionization. *Monthly Notices of the Royal Astronomical Society*, 451(3):2544, Aug. 2015. ISSN 0035-8711. doi: 10.1093/mnras/stv1114.

R. Pakmor and V. Springel. Simulations of magnetic fields in isolated disc galaxies. *Monthly Notices of the Royal Astronomical Society*, 432:176–193, June 2013. doi: 10.1093/mnras/stt428.

R. Pakmor, A. Bauer, and V. Springel. Magnetohydrodynamics on an unstructured moving grid. *Monthly Notices of the Royal Astronomical Society*, 418(2):1392–1401, Dec. 2011. doi: 10.1111/j.1365-2966.2011.19591.x.

F. Palla, E. E. Salpeter, and S. W. Stahler. Primordial star formation - The role of molecular hydrogen. *The Astrophysical Journal*, 271:632–641, Aug. 1983. doi: 10.1086/161231.

A. H. Pawlik, A. Rahmati, J. Schaye, M. Jeon, and C. Dalla Vecchia. The Aurora radiation-hydrodynamical simulations of reionization: calibration and first results. *MNRAS*, 466 (1):960–973, Apr. 2017. ISSN 0035-8711. doi: 10.1093/mnras/stw2869.

T. Peters, M.-M. Mac Low, R. Banerjee, R. S. Klessen, and C. P. Dullemond. Understanding Spatial and Spectral Morphologies of Ultracompact H II Regions. *The Astrophysical Journal*, 719:831–843, Aug. 2010. doi: 10.1088/0004-637X/719/1/831.

T. Peters, R. Banerjee, R. S. Klessen, and M.-M. Mac Low. The Interplay of Magnetic Fields, Fragmentation, and Ionization Feedback in High-mass Star Formation. *The Astrophysical Journal*, 729:72, Mar. 2011. doi: 10.1088/0004-637X/729/1/72.

M. Petkova and V. Springel. A novel approach for accurate radiative transfer in cosmological hydrodynamic simulations. *Monthly Notices of the Royal Astronomical Society*, 415: 3731–3749, Aug. 2011. doi: 10.1111/j.1365-2966.2011.18986.x.

A. Pillepich, V. Springel, D. Nelson, S. Genel, J. Naiman, R. Pakmor, L. Hernquist, P. Torrey, M. Vogelsberger, R. Weinberger, and F. Marinacci. Simulating Galaxy Formation with the IllustrisTNG Model. *MNRAS, in press; arXiv:1703.02970*, Mar. 2017.

Planck Collaboration. Planck 2018 results. VI. Cosmological parameters. *arXiv:1807.06209 [astro-ph]*, Sept. 2019. arXiv: 1807.06209.

A. C. Raga, J. Cantó, and L. F. Rodríguez. The universal time-evolution of an expanding HII region. *Revista Mexicana de Astronomia y Astrofisica*, 48:149, Apr. 2012.

D. Rahner, E. W. Pellegrini, S. C. O. Glover, and R. S. Klessen. Winds and radiation in unison: a new semi-analytic feedback model for cloud dissolution. *Monthly Notices of the Royal Astronomical Society*, 470(4):4453–4472, Oct. 2017. doi: 10.1093/mnras/stx1532.

D. Rahner, E. W. Pellegrini, S. C. O. Glover, and R. S. Klessen. WARPFIELD 2.0: feedback-regulated minimum star formation efficiencies of giant molecular clouds. *Monthly Notices*

of the Royal Astronomical Society, 483(2):2547–2560, Feb. 2019. doi: 10.1093/mnras/sty3295.

S. Reissl, S. Wolf, and R. Brauer. Radiative transfer with POLARIS. I. Analysis of magnetic fields through synthetic dust continuum polarization measurements. *Astronomy and Astrophysics*, 593:A87, Sept. 2016. ISSN 0004-6361. doi: 10.1051/0004-6361/201424930.

S. Reissl, S. Wolf, and R. Brauer. POLARIS: POLArized RadIation Simulator. *Astrophysics Source Code Library*, page ascl:1807.001, July 2018.

E. Ripamonti and T. Abel. Fragmentation and the formation of primordial protostars: the possible role of collision-induced emission. *Monthly Notices of the Royal Astronomical Society*, 348:1019–1034, Mar. 2004. doi: 10.1111/j.1365-2966.2004.07422.x.

J. Ritzerveld and V. Icke. Transport on Adaptive Random Lattices. *Phys. Rev. E*, 74:26704, July 2006. doi: 10.1103/PhysRevE.74.026704.

M. Röllig, N. P. Abel, T. Bell, F. Bensch, J. Black, G. J. Ferland, B. Jonkheid, I. Kamp, M. J. Kaufman, J. Le Bourlot, F. Le Petit, R. Meijerink, O. Morata, V. Ossenkopf, E. Roueff, G. Shaw, M. Spaans, A. Sternberg, J. Stutzki, W. F. Thi, E. F. van Dishoeck, P. A. M. van Hoof, S. Viti, and M. G. Wolfire. A photon dominated region code comparison study. *Astronomy and Astrophysics*, 467(1):187–206, May 2007. doi: 10.1051/0004-6361:20065918.

J. Rosdahl and R. Teyssier. A scheme for radiation pressure and photon diffusion with the M1 closure in ramses-rt. *Monthly Notices of the Royal Astronomical Society*, 449(4):4380–4403, June 2015. ISSN 0035-8711. doi: 10.1093/mnras/stv567.

J. Rosdahl, J. Blaizot, D. Aubert, T. Stranex, and R. Teyssier. ramses-rt: radiation hydrodynamics in the cosmological context. *Monthly Notices of the Royal Astronomical Society*, 436(3):2188–2231, Dec. 2013. ISSN 0035-8711. doi: 10.1093/mnras/stt1722.

A. L. Rosen, M. R. Krumholz, C. F. McKee, and R. I. Klein. An unstable truth: how massive stars get their mass. *Monthly Notices of the Royal Astronomical Society*, 463:2553–2573, Dec. 2016. doi: 10.1093/mnras/stw2153.

N. Roth and D. Kasen. Monte Carlo Radiation-Hydrodynamics With Implicit Methods. *The Astrophysical Journal Supplement Series*, 217(1):9, Mar. 2015. doi: 10.1088/0067-0049/217/1/9.

D. Schaerer. On the properties of massive Population III stars and metal-free stellar populations. *Astronomy and Astrophysics*, 382:28, Jan. 2002. doi: 10.1051/0004-6361:20011619.

A. T. P. Schauer, D. J. Whalen, S. C. O. Glover, and R. S. Klessen. Lyman-Werner UV escape fractions from primordial haloes. *Monthly Notices of the Royal Astronomical Society*, 454:2441–2450, Dec. 2015. doi: 10.1093/mnras/stv2117.

A. T. P. Schauer, B. Agarwal, S. C. O. Glover, R. S. Klessen, M. A. Latif, L. Mas-Ribas, C.-E. Rydberg, D. J. Whalen, and E. Zackrisson. Lyman-Werner escape fractions from the first galaxies. *Monthly Notices of the Royal Astronomical Society*, 467(2):2288–2300, May 2017a. doi: 10.1093/mnras/stx264.

A. T. P. Schauer, J. Regan, S. C. O. Glover, and R. S. Klessen. The formation of direct collapse black holes under the influence of streaming velocities. *Monthly Notices of the Royal Astronomical Society*, 471:4878–4884, Nov. 2017b. doi: 10.1093/mnras/stx1915.

A. T. P. Schauer, S. C. O. Glover, R. S. Klessen, and D. Ceverino. The influence of streaming velocities on the formation of the first stars. *Monthly Notices of the Royal Astronomical Society*, 484(3):3510–3521, Apr. 2019. doi: 10.1093/mnras/stz013.

D. R. G. Schleicher, D. Galli, S. C. O. Glover, R. Banerjee, F. Palla, R. Schneider, and R. S. Klessen. The Influence of Magnetic Fields on the Thermodynamics of Primordial Star Formation. *The Astrophysical Journal*, 703:1096–1106, Sept. 2009. doi: 10.1088/0004-637X/703/1/1096.

J. Schober, D. Schleicher, C. Federrath, S. Glover, R. S. Klessen, and R. Banerjee. The Small-scale Dynamo and Non-ideal Magnetohydrodynamics in Primordial Star Formation. *The Astrophysical Journal*, 754:99, Aug. 2012a. doi: 10.1088/0004-637X/754/2/99.

J. Schober, D. Schleicher, C. Federrath, R. Klessen, and R. Banerjee. Magnetic field amplification by small-scale dynamo action: Dependence on turbulence models and Reynolds and Prandtl numbers. *Physical Review E*, 85(2):026303, Feb. 2012b. doi: 10.1103/PhysRevE.85.026303.

F. H. Shu, S. Lizano, D. Galli, J. Cantó, and G. Laughlin. Self-similar Champagne Flows in H II Regions. *The Astrophysical Journal*, 580(2):969, Dec. 2002. doi: 10.1086/343859.

R. A. Simcoe, P. W. Sullivan, K. L. Cooksey, M. M. Kao, M. S. Matejek, and A. J. Burgasser. Extremely metal-poor gas at a redshift of 7. *Nature*, 492:79–82, Dec. 2012. doi: 10.1038/nature11612.

A. Smith, B. T. H. Tsang, V. Bromm, and M. Milosavljević. Discrete diffusion Lyman αradiative transfer. *Monthly Notices of the Royal Astronomical Society*, 479(2):2065–2078, Sept. 2018. doi: 10.1093/mnras/sty1509.

R. J. Smith, S. C. O. Glover, P. C. Clark, T. Greif, and R. S. Klessen. The effects of accretion luminosity upon fragmentation in the early universe. *Monthly Notices of the Royal Astronomical Society*, 414:3633–3644, July 2011. doi: 10.1111/j.1365-2966.2011.18659.x.

R. J. Smith, T. Hosokawa, K. Omukai, S. C. O. Glover, and R. S. Klessen. Variable accretion rates and fluffy first stars. *Monthly Notices of the Royal Astronomical Society*, 424:457–463, July 2012. doi: 10.1111/j.1365-2966.2012.21211.x.

R. J. Smith, S. C. O. Glover, R. S. Klessen, and G. A. Fuller. On the nature of star-forming filaments - II. Subfilaments and velocities. *Monthly Notices of the Royal Astronomical Society*, 455:3640–3655, Feb. 2016. doi: 10.1093/mnras/stv2559.

L. Spitzer. *Physical processes in the interstellar medium*. A Wiley-Interscience Publication, New York: Wiley, 1978a.

L. Spitzer. *Physical Processes in the Interstellar Medium*. Wiley-VCH Verlag GmbH, Weinheim, Germany, May 1978b. ISBN 978-3-527-61772-2. doi: 10.1002/9783527617722.

V. Springel. The cosmological simulation code GADGET-2. *Mon.Not.Roy.Astron.Soc.*, 364: 1105–1134, May 2005. doi: 10.1111/j.1365-2966.2005.09655.x.

V. Springel. E pur si muove: Galilean-invariant cosmological hydrodynamical simulations on a moving mesh. *Monthly Notices of the Royal Astronomical Society*, 401(2):791, Jan. 2010. doi: 10.1111/j.1365-2966.2009.15715.x.

A. Stacy and V. Bromm. Constraining the statistics of Population III binaries. *Monthly Notices of the Royal Astronomical Society*, 433:1094–1107, Aug. 2013. doi: 10.1093/mnras/stt789.

A. Stacy, V. Bromm, and A. Loeb. Effect of Streaming Motion of Baryons Relative to Dark Matter on the Formation of the First Stars. *The Astrophysical Journal Letters*, 730:L1, Mar. 2011. doi: 10.1088/2041-8205/730/1/L1.

A. Stacy, T. H. Greif, and V. Bromm. The first stars: mass growth under protostellar feedback. *Monthly Notices of the Royal Astronomical Society*, 422(1):290, May 2012. doi: 10.1111/j.1365-2966.2012.20605.x.

A. Stacy, A. H. Pawlik, V. Bromm, and A. Loeb. The mutual interaction between Population III stars and self-annihilating dark matter. *Monthly Notices of the Royal Astronomical Society*, 441:822–836, June 2014. doi: 10.1093/mnras/stu621.

A. Stacy, V. Bromm, and A. T. Lee. Building up the Population III initial mass function from cosmological initial conditions. *Monthly Notices of the Royal Astronomical Society*, 462(2):1307, Oct. 2016. doi: 10.1093/mnras/stw1728.

B. Strömgren. The Physical State of Interstellar Hydrogen. *ApJ*, 89:526–547, 1939. ISSN 0004-637X. doi: 10.1007/s13398-014-0173-7.2.

K. Sugimura, T. Matsumoto, T. Hosokawa, S. Hirano, and K. Omukai. The Birth of a Massive First-Star Binary. *arXiv:2002.00012 [astro-ph]*, Jan. 2020. arXiv: 2002.00012.

S. Sur, D. R. G. Schleicher, R. Banerjee, C. Federrath, and R. S. Klessen. The Generation of Strong Magnetic Fields During the Formation of the First Stars. *The Astrophysical Journal Letters*, 721:L134–L138, Oct. 2010. doi: 10.1088/2041-8205/721/2/L134.

S. Sur, C. Federrath, D. R. G. Schleicher, R. Banerjee, and R. S. Klessen. Magnetic field amplification during gravitational collapse - influence of turbulence, rotation and gravitational compression. *Monthly Notices of the Royal Astronomical Society*, 423: 3148–3162, July 2012. doi: 10.1111/j.1365-2966.2012.21100.x.

H. Susa. The Mass of the First Stars. *The Astrophysical Journal*, 773(2):185, Aug. 2013. doi: 10.1088/0004-637X/773/2/185.

H. Susa. Merge or survive: Number of Population III stars per minihalo. *arXiv:1904.09731 [astro-ph]*, Apr. 2019. arXiv: 1904.09731.

H. Susa, K. Hasegawa, and N. Tominaga. The Mass Spectrum of the First Stars. *The Astrophysical Journal*, 792(1):32, Sept. 2014. doi: 10.1088/0004-637X/792/1/32.

J. C. Tan and C. F. McKee. The Formation of the First Stars. I. Mass Infall Rates, Accretion Disk Structure, and Protostellar Evolution. *The Astrophysical Journal*, 603:383–400, Mar. 2004. doi: 10.1086/381490.

R. Teyssier. Cosmological hydrodynamics with adaptive mesh refinement. A new high resolution code called RAMSES. *å*, 385:1349–1374, Apr. 2002. doi: 10.1051/0004-6361: 20011817.

A. Toomre. On the gravitational stability of a disk of stars. *The Astrophysical Journal*, 139: 1217–1238, May 1964. ISSN 0004-637X. doi: 10.1086/147861.

J. K. Truelove, R. I. Klein, C. F. McKee, J. H. Holliman, II, L. H. Howell, and J. A. Greenough. The Jeans Condition: A New Constraint on Spatial Resolution in Simulations of Isothermal Self-gravitational Hydrodynamics. *The Astrophysical Journal Letters*, 489: L179+, Nov. 1997. doi: 10.1086/316779.

D. Tseliakhovich and C. Hirata. Relative velocity of dark matter and baryonic fluids and the formation of the first structures. *Physical Review D*, 82(8):083520, Oct. 2010. doi: 10.1103/PhysRevD.82.083520.

M. J. Turk, T. Abel, and B. O'Shea. The Formation of Population III Binaries from Cosmological Initial Conditions. *Science*, 325:601–, July 2009. doi: 10.1126/science. 1173540.

M. J. Turk, J. S. Oishi, T. Abel, and G. L. Bryan. Magnetic Fields in Population III Star Formation. *The Astrophysical Journal*, 745:154, Feb. 2012. doi: 10.1088/0004-637X/ 745/2/154.

N. J. Turner and J. M. Stone. A Module for Radiation Hydrodynamic Calculations with ZEUS-2D Using Flux-limited Diffusion. *The Astrophysical Journal Supplement Series*, 135:95–107, July 2001. doi: 10.1086/321779.

B. Vandenbroucke and K. Wood. The Monte Carlo photoionization and moving-mesh radiation hydrodynamics code CMACIONIZE. *Astronomy and Computing*, 23:40, Apr. 2018. doi: 10.1016/j.ascom.2018.02.005.

D. A. Verner, G. J. Ferland, K. T. Korista, and D. G. Yakovlev. Atomic Data for Astrophysics. II. New Analytic FITS for Photoionization Cross Sections of Atoms and Ions. *The Astrophysical Journal*, 465:487, July 1996. doi: 10.1086/177435.

M. Vogelsberger, S. Genel, V. Springel, P. Torrey, D. Sijacki, D. Xu, G. F. Snyder, D. Nelson, and L. Hernquist. Introducing the Illustris Project: Simulating the coevolution of dark and visible matter in the Universe. *MNRAS*, 444(2):1518–1547, May 2014. ISSN 0035-8711. doi: 10.1093/mnras/stu1536.

E. I. Vorobyov, A. L. DeSouza, and S. Basu. The Burst Mode of Accretion in Primordial Protostars. *The Astrophysical Journal*, 768(2):131, May 2013. doi: 10.1088/0004-637X/768/2/131.

D. Whalen, T. Abel, and M. L. Norman. Radiation Hydrodynamic Evolution of Primordial H II Regions. *The Astrophysical Journal*, 610:14–22, July 2004. doi: 10.1086/421548.

D. J. Whalen and M. L. Norman. A Multistep Algorithm for the Radiation Hydrodynamical Transport of Cosmological Ionization Fronts and Ionized Flows. *ApJS*, 162(2):281–303, Aug. 2005. ISSN 0067-0049. doi: 10.1086/499072.

J. H. Wise and T. Abel. ENZO+MORAY: radiation hydrodynamics adaptive mesh refinement simulations with adaptive ray tracing. *Monthly Notices of the Royal Astronomical Society*, 414(4):3458–3491, July 2011. doi: 10.1111/j.1365-2966.2011.18646.x.

J. H. Wise, T. Abel, M. J. Turk, M. L. Norman, and B. D. Smith. The birth of a galaxy - II. The role of radiation pressure. *Monthly Notices of the Royal Astronomical Society*, 427 (1):311, Nov. 2012a. doi: 10.1111/j.1365-2966.2012.21809.x.

J. H. Wise, M. J. Turk, M. L. Norman, and T. Abel. The Birth of a Galaxy: Primordial Metal Enrichment and Stellar Populations. *The Astrophysical Journal*, 745:50, Jan. 2012b. doi: 10.1088/0004-637X/745/1/50.

J. Wolcott-Green and Z. Haiman. Suppression of HD cooling in protogalactic gas clouds by Lyman-Werner radiation. *Monthly Notices of the Royal Astronomical Society*, 412(4): 2603, Apr. 2011. doi: 10.1111/j.1365-2966.2010.18080.x.

K. M. J. Wollenberg, S. C. O. Glover, P. C. Clark, and R. S. Klessen. Formation sites of Population III star formation: The effects of different levels of rotation and turbulence on the fragmentation behavior of primordial gas. *MNRAS, submitted; arXiv:1912.06377*, Jan. 2019.

H. Xu, J. H. Wise, M. L. Norman, K. Ahn, and B. W. O'Shea. GALAXY PROPERTIES AND UV ESCAPE FRACTIONS DURING THE EPOCH OF REIONIZATION: RESULTS FROM THE RENAISSANCE SIMULATIONS. *ApJ*, 833(1):84, 2016. ISSN 1538-4357. doi: 10.3847/1538-4357/833/1/84.

H. W. Yorke and C. Sonnhalter. On the Formation of Massive Stars. *The Astrophysical Journal*, 569:846–862, Apr. 2002. doi: 10.1086/339264.

N. Yoshida, S. P. Oh, T. Kitayama, and L. Hernquist. Early Cosmological H II/He III Regions and Their Impact on Second-Generation Star Formation. *The Astrophysical Journal*, 663: 687–707, July 2007. doi: 10.1086/518227.

N. Yoshida, T. Hosokawa, and K. Omukai. Formation of the first stars in the universe. *Prog. Theor. Exp. Phys*, 2012(1):01A305, Oct. 2012. doi: 10.1093/ptep/pts022.

H. Zinnecker and H. W. Yorke. Toward Understanding Massive Star Formation. *Annual Review of Astron and Astrophys*, 45:481–563, Sept. 2007. doi: 10.1146/annurev.astro.44.051905.092549.

A. Zonca, L. Singer, D. Lenz, M. Reinecke, C. Rosset, E. Hivon, and K. Gorski. healpy: equal area pixelization and spherical harmonics transforms for data on the sphere in Python. *Journal of Open Source Software*, 4(35):1298, Mar. 2019. doi: 10.21105/joss.01298.